Chemical Transformations of Lithium Cobalt Oxide Nanoparticles in Model Environmental

Systems

By

Elizabeth Dina Laudadio

A dissertation submitted in partial fulfillment of

the requirements for the degree of

Doctor of Philosophy

(Chemistry)

at the

UNIVERSITY OF WISCONSIN-MADISON

2020

Chemical Transformations of Lithium Cobalt Oxide Nanoparticles in Model Environmental Systems

Elizabeth Dina Laudadio

Under the supervision of Professor Robert J. Hamers

University of Wisconsin – Madison

Abstract

Complex metal oxides are important nanomaterials for catalysis, energy storage, and water purification. These nanomaterials are being rapidly incorporated into numerous commercial products, however, the potential impact to the environment upon improper disposal is still unknown. A commonly overlooked and largely unknown aspect of assessing the environmental and biological safety of engineered nanomaterials is their transformation in aqueous systems. We present a comprehensive analysis of the interaction of an environmentally relevant oxyanion, phosphate, with a complex metal oxide nanomaterial, lithium cobalt oxide ($LiCoO_2$), through the implementation of complementary *in situ* analytical techniques to probe the reactions occurring at the nanoparticle-liquid interface. Attenuated total reflectance – FTIR (ATR-FTIR) experiments confirm irreversible adsorption of phosphate to $LiCoO_2$ in a predominantly deprotonated geometry on the surface. Using laser doppler microelectrophoresis, dynamic light scattering, and UV-visible spectroscopy, we show that adsorption of phosphate at environmentally relevant concentrations on $LiCoO_2$ nanoparticles significantly alters their surface charge, and therefore dispersibility in solution. The adsorbed phosphate remains on the surface over significant periods of time, suggesting that desorption is not kinetically favored. Potential implications of this interaction may be increased dispersibility and bioavailability of these materials in environmental water systems.

Additional studies present a thermodynamic analysis of phosphate adsorption to $LiCoO_2$ and corroborate the results with additional in situ techniques, including zeta potential measurements and ATR−FTIR spectroscopy, at pH values relevant to potential environmental release scenarios. Flow microcalorimetry measurements of phosphate interaction with $LiCoO_2$ at pH 7.4 show that there are two distinct exothermic processes taking place. Time-sequence in situ ATR−FTIR with two-dimensional correlation analysis reveals the spectroscopic signatures of these processes. We interpret the data as an interaction of phosphate with $LiCoO_2$ that occurs through the release of two water molecules and is therefore, best described as a condensation process rather than a simple adsorption, consistent with prior studies, demonstrating that phosphate interaction with $LiCoO_2$ is highly irreversible. Additional measurements for over longer times of 5 months show that phosphate adsorption terminates with one surface layer and that continued transformation over longer periods of time arises from H^+/Li^+ exchange and slow transformation to a cobalt hydroxide, with phosphate adsorbed to the surface only. To the best of our knowledge, this is the first time that flow microcalorimetry and two-dimensional correlation analysis have been applied in tandem to clarify the specific chemical reactions that occur at the interface of solids and adsorbates.

These studies highlight the power of using multiple in situ techniques in tandem to tackle complex research questions at the nanoparticle-liquid interface, and have opened the door to studies involving more complex systems. Organic molecules, such as small organic acids and natural organic matter are present in environmental water systems, and have the potential to interact competitively with phosphate and other molecules for adsorption to the surface of $LiCoO_2$. We show that the impact of small organic acids on adsorption to, and dissolution of $LiCoO_2$ is controlled at least partially by the hydrophobicity and/or steric hinderance of the molecule. X-ray

iii

photoelectron spectroscopy elucidates the competitive interaction between lactic acid and phosphate with the $LiCoO_2$ surface, where the presence of lactic acid results in less coverage of phosphate on the particles.

Through the development and use of complementary in situ methodologies, we have enabled the exploration of the competitive interactions of a variety of environmentally relevant molecules with $LiCoO_2$. The analytical toolkit established in this work can used to build up complexity of model environment systems in a systematic and controlled manner to enable the elucidation of the important factors that control the transformation, and therefore fate and transport, of this class of materials.

Acknowledgements

Table of Contents

Chapter I. An introduction for non-scientists: Lithium cobalt oxide nanoparticles and how they interact with phosphate molecules

This chapter is accessible to the public through the Wisconsin Initiative for Science Literacy (WISL).

I.0. Context.

Throughout my training in graduate school, I have become increasingly fascinated by the way that we communicate science. One of the most important goals of science and research is to protect and improve the lives of everyone. Science belongs to all of us, and yet, it is not always perceived this way. Scientists can be viewed as elite, untouchable, and our work is often shrouded from the public eye. Even when the public has access to the work, it is often filled with jargon and technical terms, making it entirely inaccessible. This not only is unfair to the public, but it is also a failure of our responsibility as scientists. I believe the mark of a truly good scientist is being able to not only do good science, but be able to boil it down to the most important information, and explain the core of the work in a way that is accessible to anyone. Doing this well is sometimes harder than doing the work itself. As a scientist, you must truly understand your work to be able to communicate it effectively and generally. It is a skill that is important to develop, and the only way to do so is to practice. I'm grateful to the Wisconsin Initiative for Science Literacy at UW-Madison for providing this platform for researchers at our institution, and for sponsoring and supporting the creation of this chapter.

I.1. Introduction to nanomaterials.

In 1959, physicist Dr. Richard Feynman delivered a lecture entitled "There's Plenty of Room at the Bottom." In Feynman's lecture, he posed the question, "what if you could fit the entire Encyclopedia Britannica on the head of a pin?" He painted a picture of a world where you could

"swallow the surgeon," "arrange atoms the way we want." While at the time, the speech felt more like science fiction than science itself, many of his predictions are well on their way to becoming reality.

The core message of Feynman's lecture was the idea that there is a whole world of science and technology yet to be discovered, that we could access by zooming in, or looking down. Many credit this lecture with sparking the field of nanotechnology, though the field did not truly take off until the 1980s.

What is nanotechnology? Simply put, nanotechnology is the study of nanomaterials that have a technologically relevant function. Nanomaterials, as the name suggests, are very, very small materials. These materials can be technologically useful, because the properties of many materials change when you shrink them down to the nanoscale.

Just how small are we talking, you may be wondering. One nanometer is one billionth of a meter (a meter is just about the same as one yard, or 3 feet long). Figure I.1 illustrates what a nanometer is with respect to some other materials. Note that one nanometer is smaller than a single cell - bacteria cells can be about 1,000 nm long, with human cells being larger at around 10,000 nm long. A period at the end of a sentence in 12-point type is about one million nanometers long, and a tennis ball is around one hundred million nanometers long. Something this size is really hard to conceptualize, but the important thing to know is that nanomaterials are really, really small.
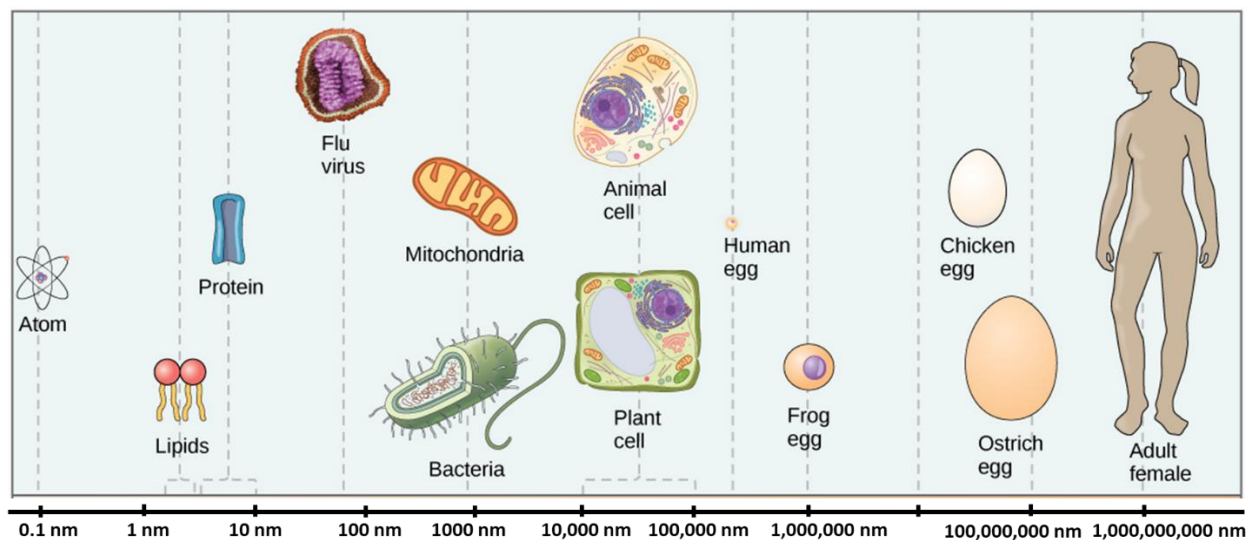
Figure I.1. Scale of different objects in nanometers. Image from WikiCommons.

When you take a bulk material and shrink it to the nanoscale, the properties of that material start to change. Take gold nanoparticles for instance. Nanoparticles of gold can be suspended in water, meaning that they are so small they can essentially "float" in water. An example of this in everyday life is muddy water – the dirt is suspended in the water, and so the water appears to be brown. When gold nanoparticles are suspended in water, the water appears red. Figure I.2 shows suspensions of gold nanoparticles in vials, where the larger the particle size, the darker the red color. This is unlike bulk gold, which has a color we are all familiar with. The color changes because on the nanoscale, the gold interacts differently with light. Below each vial in Figure I.2 is a microscopy image of the gold nanoparticles.
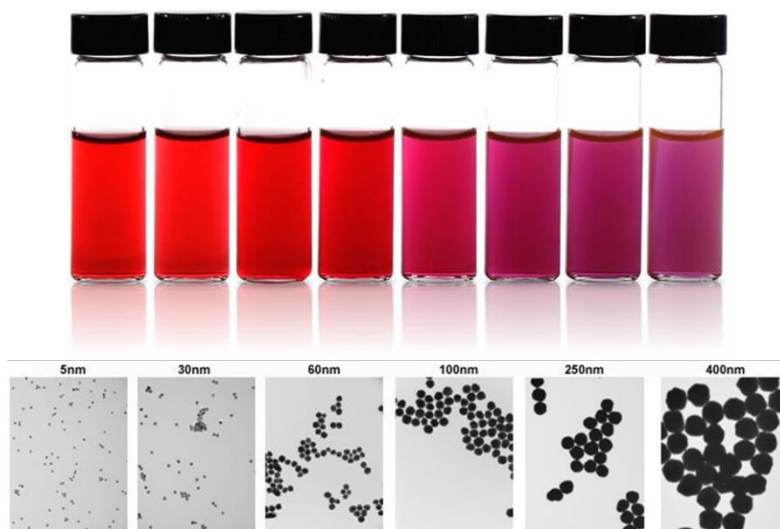
Figure I.2. Top: vials of gold nanoparticle suspensions. Image from Shopify. Bottom: microscopy images of the nanoparticles that are in each suspension. Image from Sigma Aldrich.

Another example of how the optical properties of nanomaterials is different from the properties of the bulk material is illustrated in Figure I.3. Thin films of silicon dioxide (SiO_2, or quartz), have very different visible colors depending on their thickness in the nanometer-range. The 300 nm thick film of quartz is a vibrant purple, while the 200 nm film is a sunny yellow. Both are vastly different from the bulk crystal, shown on the right.
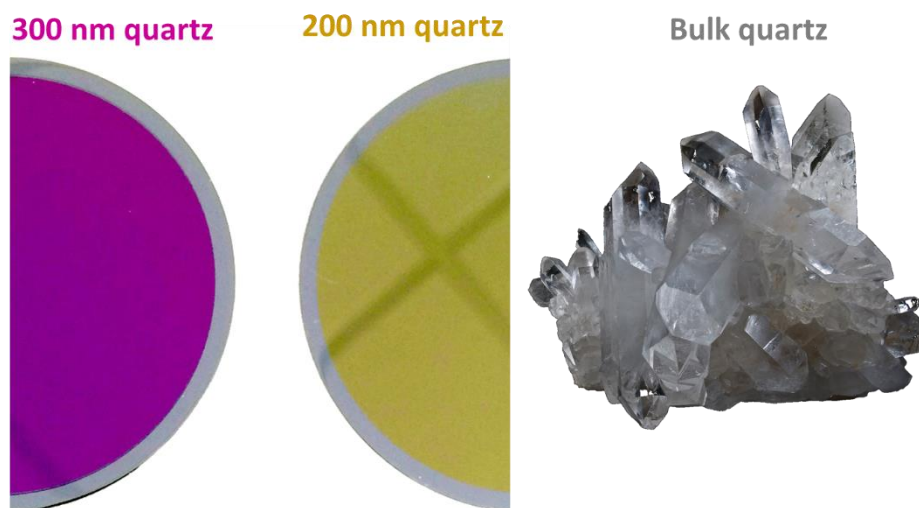
Figure I.3. 300 nm of quartz is purple (left) while 200 nm is yellow (middle). Bulk quartz crystal is transparent. Image from WikiCommons.

The color of a material is just one example of a property that changes on the nanoscale. One reason that nanomaterials have different properties than their bulk counterparts has to do with the surface area to volume ratio of the atoms in the material. As you take a material and shrink it down, there is a higher percentage of the total atoms in the material that are at the surface. We can consider Rubik's cubes of different sizes to understand how this works. Figure I.4 shows four different sizes of Rubik's cubes. The volume of a 5 by 5 by 5 Rubik's cube is 125 units cubed (length times width times height) and the surface area is 150 units squared (area of each face of the cube, 5 times 5, multiplied by the number of faces, 6). Therefore the surface area to volume ratio is 1.2.

length = 5	length = 4	length = 3	length = 2
Surface area: (5 x 5 x 6) = 150	Surface area = 96	Surface area = 54	Surface area = 24
Volume: 5^3 = 125	Volume = 64	Volume = 27	Volume = 8
Surface Area : Volume Ratio = 1.2	**Surface Area : Volume Ratio = 1.5**	**Surface Area : Volume Ratio: 2**	**Surface Area : Volume Ratio: 3**

Decreasing size means more "atoms" on the surface!
Surfaces are reactive.
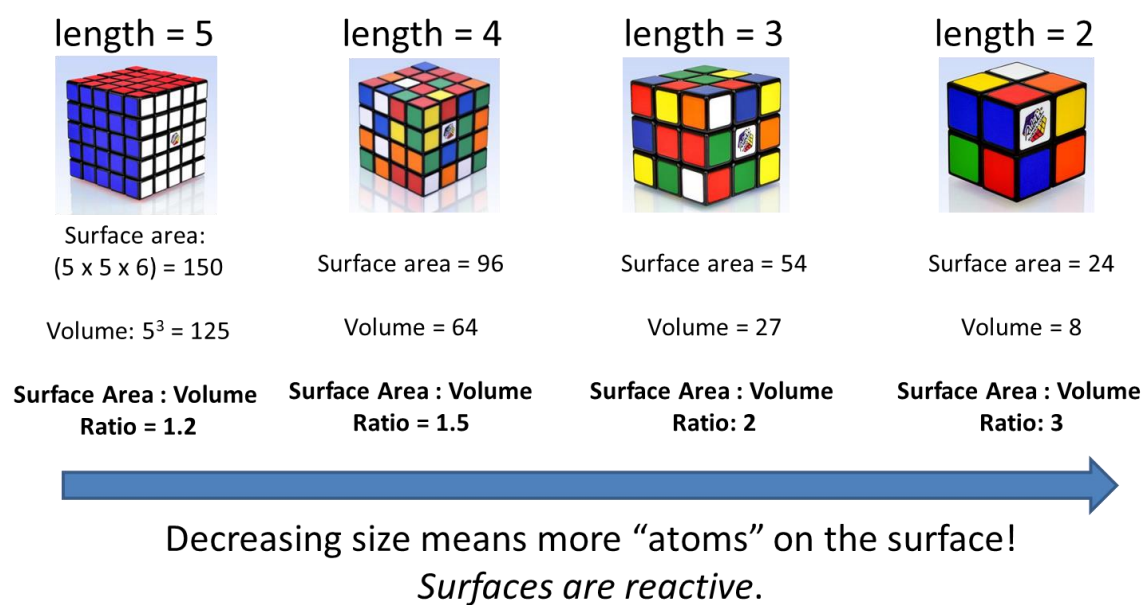
Figure I.4. Illustrating the surface area to volume ratio using Rubik's cubes. Images from Rubik's.

If we shrink this cube down, by the time we have a 2 by 2 by 2 cube, we now have a surface area of 24 units squared, and a volume of 8 units cubes. Our surface area to volume ratio is now 3, which is much higher than the 5 by 5 by 5 cube. The reason this is important for materials is

that surface atoms are often more reactive. The more atoms at the surface, or the higher the surface area to volume ratio, the more reactive a material can be.

I.2. Introduction to sustainable nanotechnology.

Because nanomaterials have such interesting properties, researchers have been using them to create new technologies. One example of this is a particular kind of nanoparticle called quantum dots, which can have vibrant and varied colors. These types of nanoparticles are being used in tablet and television screens, such as QLED TVs. Scientists are also researching how nanomaterials can be used to advance science, energy storage, solar panels, and much more.

But because there is still a lot that we don't know about nanomaterials, a lot of scientists have dedicated their studies to understanding the potential environmental and biological impacts of nanomaterials. My research is part of the Center for Sustainable Nanotechnology (CSN), funded by the National Science Foundation, which is a collaborative network of scientists from many fields dedicated to understanding the fundamental chemistry behind how nanomaterials interact with biological and environmental systems. Some of our scientists study how nanoparticles and bacterial cells interact – Figure 5 shows an electron microscopy image of gold nanoparticles at the cell wall of a bacterium.[1]
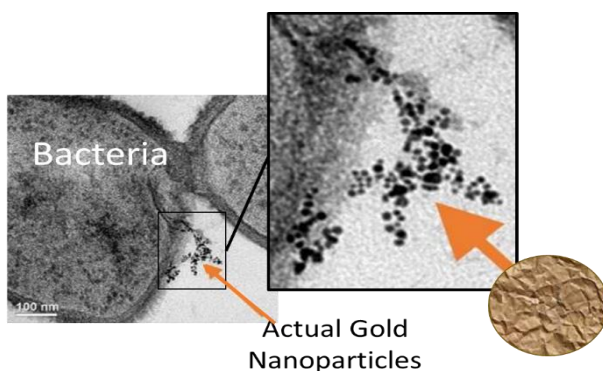
Figure I.5. An electron microscopy image of gold nanoparticles near the surface of a bacterium. Adapted from Reference 1.

We also have scientists studying nanomaterials for sustainable agriculture, where we've shown that copper containing nanomaterials can help fend off fungal disease on watermelon plants.[2] My thesis research is a part of the CSN, where I have spent five years in graduate school researching how a particular nanomaterial called lithium cobalt oxide interacts with model (simplified) environmental waters, which I will explain in more detail below.

I.3. What is lithium cobalt oxide, and why do we care about it?

Lithium cobalt oxide (LCO) is a very important material in all of our lives. It is a material that is used in lithium-ion batteries (LIBs), which are the most common type of rechargeable batteries. LIBs are in our cellphones, laptops, Nintendo Switch systems, and more; most things that you plug in to recharge are not only LIBs, they also contain LCO or a related material.

LIBs have three main components; the anode, the cathode, and the electrolyte, as shown in Figure I.6.[3] LIBs operate by shuttling lithium ions between the anode and cathode through the electrolyte. The electrolyte is a combination of a solvent and a salt that are able to solvate the lithium ions. This solvation is effectively like providing a boat for the lithium ions to travel through the liquid from the anode to the cathode. For each lithium ion that is transferred, an electron can move through a circuit, which generates electricity. A common anode material is graphite, which is a layered version of carbon (the same thing that is used in pencils). LCO is a popular choice as a cathode material, as it consists of layers of oxygen and metal atoms, with lithium "intercalated" in between the layers. What that means is that the lithium ions are able to be very mobile, which is a good quality for a battery cathode, since the function of the battery relies on those lithium ions being able to move easily from anode to cathode, and vice versa. The structure of LCO makes the movement of lithium ions easier, by providing a straight, short path for them to follow to get to the "boat" (electrolyte) and travel to the anode.
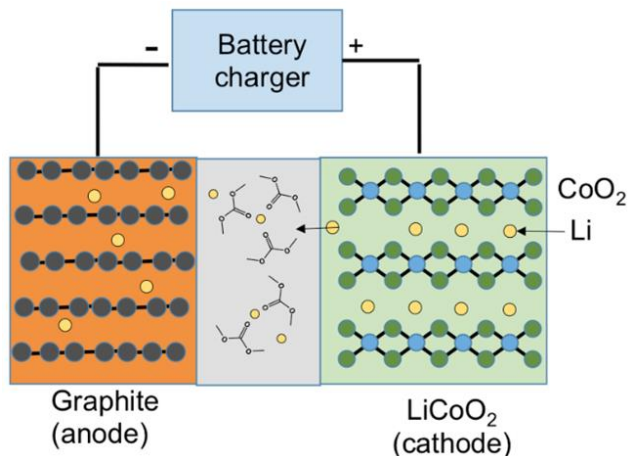
Figure I.6. Schematic of a lithium ion battery. Image from Bob Hamers (adapted from Ref 3)

It's undeniable that these materials are ubiquitous in our every-day life. Many of us have cell phones, laptops, rechargeable wireless headphones, portable gaming systems – almost everything you use that you plug in to charge at night uses a battery like this. LIBs are being used in electric vehicles, the production and use of which is on the rise. In just one of these vehicles, there are tens of kilograms of cathode material. With no federally instated infrastructure for recycling these materials, and low economic incentive to do so, it is inevitable that these materials will be improperly disposed of and end up in landfills and potentially our environment. For these reasons, researchers like me in the CSN are working to understand what the impacts of these materials like LCO may be on the environment.

I.4. How does lithium cobalt oxide interact with the environment?

"The environment" is a very complex system, and it is an oversimplification to lump it all into one category. For the sake of this chapter, the environment that I am considering is surface waters, like those of lakes or rivers. Cathode materials being disposed of may end up in these systems through a variety of pathways. Cathode materials like LCO function well in their intended systems – batteries – which require a very specific chemical environment to operate. These materials are not designed to be in water, and until recently, we did not know what would happen

to these materials if they were put into water. Surface waters can have a variety of different molecules in them that could interact with the LCO particles, as suggested schematically in Figure I.7. When LCO interacts with these molecules, the particles may "transform" – an umbrella term we use to describe a change in properties of the material from their "pristine" or intended form.
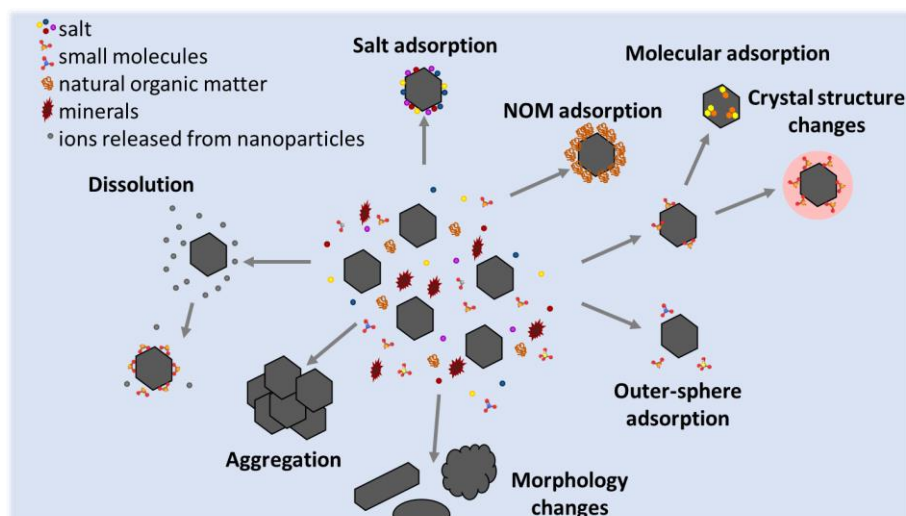
Figure I.7. Possible transformations of LCO nanoparticles in a natural water system.

A lot of my work has focused on one small aspect of this – looking at how LCO interacts with a molecule called phosphate. Phosphate is an important molecule that is environmentally, biologically, and technologically relevant. Phosphate is present in surface waters, such as those in lakes, at low concentrations. Many places are seeing enhanced concentrations of phosphate in their surface waters, as a result of fertilizer runoff. Fertilizer runoff occurs when some of the applied fertilizer doesn't make it to the intended plants; instead, this excess fertilizer is transported from the soil into these bodies of water. Excess phosphate in natural waters can have negative effects. High phosphate environments support algae, and so the algal blooms that you may see on the lakes in Madison during the summer are caused in part by phenomena such as this.

Phosphate is also important in biological systems. It is present in the growth medium that researchers in the CSN use to grow the bacteria they study. It is important for us to know if LCO and phosphate interact, and how that may change how LCO then interacts with the bacteria. Phosphate groups are also present in many biomolecules, such as DNA. Phosphate coatings are also used on medical implants to help recognition between the implant and the body, and similar coatings are used on pipes for irrigation to prevent metal leaching into the water.

I used an analytical method known as infrared spectroscopy to investigate how phosphate and LCO interact. Infrared spectroscopy is a useful technique that provides specific signatures for every molecule. When a molecule interacts with infrared (low energy) light, the chemical bonds in that molecule can stretch or bend. These motions are caused by an absorption of the energy by the molecule, which results in a signal that we can read. We can think of the bonds between atoms as springs that can be stretched and compressed. Certain bonds will be like stiffer springs, and so more energy will be needed to stretch and compress those bonds. Because every bond requires a specific amount of energy to be stretched or compressed, we can use this technique to identify what those different bonds are.

I specifically used a surface-sensitive method of this technique that let me see how phosphate molecules bind to LCO.[4] Figure I.8a shows a schematic for my experimental set-up. I deposited LCO nanoparticles on the surface of a prism, which I could then seal in a liquid cell. I was able to then flow phosphate over the particles, and see if and how it stuck to the surface. I found that phosphate binds to LCO quite strongly, and even after trying to rinse it off, it stays bound. By interpreting the infrared spectroscopy signature shown in Figure I.8b, I was able to determine how the molecule was bound to the surface, shown in Figure I.8c. This allowed me to hypothesize that LCO with phosphate bound to it would likely be negatively charged, because how

the molecule was bound left a negative charge on the molecule. To test this hypothesis, I used another technique to measure how the nanoparticle's zeta potential, or effective surface charge, changed in the presence of phosphate.
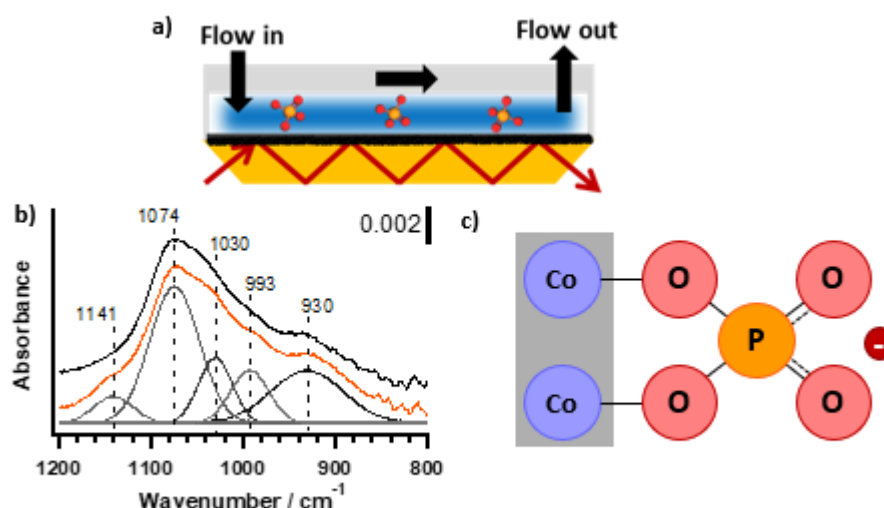
Figure I.8. a) a schematic of the infrared spectroscopy experimental setup. The binding of phosphate to LCO is probed by flowing phosphate solutions over a surface with LCO particles on it. b) the infrared signature from the experiment, adapted from Reference 4. c) the proposed structure of phosphate bound to the LCO surface.

When I measured the zeta potential of LCO in different concentrations of phosphate, I found that my hypothesis was correct. Figure I.9a. shows that as phosphate concentration increased, the LCO particles became more and more negatively charged. At the highest concentrations, the particles had zeta potentials of -30 millivolts (mV) or lower, which is consistent with particles being stable in suspension – similar to how the gold nanoparticles in Figure I.2. are evenly dispersed within the liquid. I used another spectroscopic technique to get more evidence for this phenomenon. The particles themselves absorb light in the near-UV range of the color spectrum. Absorbance is proportional to concentration, so by tracking LCO absorbance over time, I was able to get a sense of what percentage of particles were stable in suspension. We can use the "muddy water" analogy again to picture what this looks like. If you added mud to water and shook

it, it would form a suspension, and the water would appear brown. Over time, the dirt would settle

to the bottom, and the water itself would look less and less brown. This means less light is being

absorbed, and more is being reflected. That's exactly what I was tracking for the LCO particles,

but instead of just looking by eye, I used the instrument to provide more exact data on how the

absorbance was changing over time. Figure I.9b shows how the absorbance of the LCO suspension

decays over time more quickly when phosphate isn't present (blue trace) than when it is present

(orange trace). This means that the LCO settles to the bottom quicker when phosphate is not there.

Because absorbance is proportional to concentration, this confirms that in the presence of

phosphate, the LCO is more stable in suspension, as the zeta potential measurements suggested.
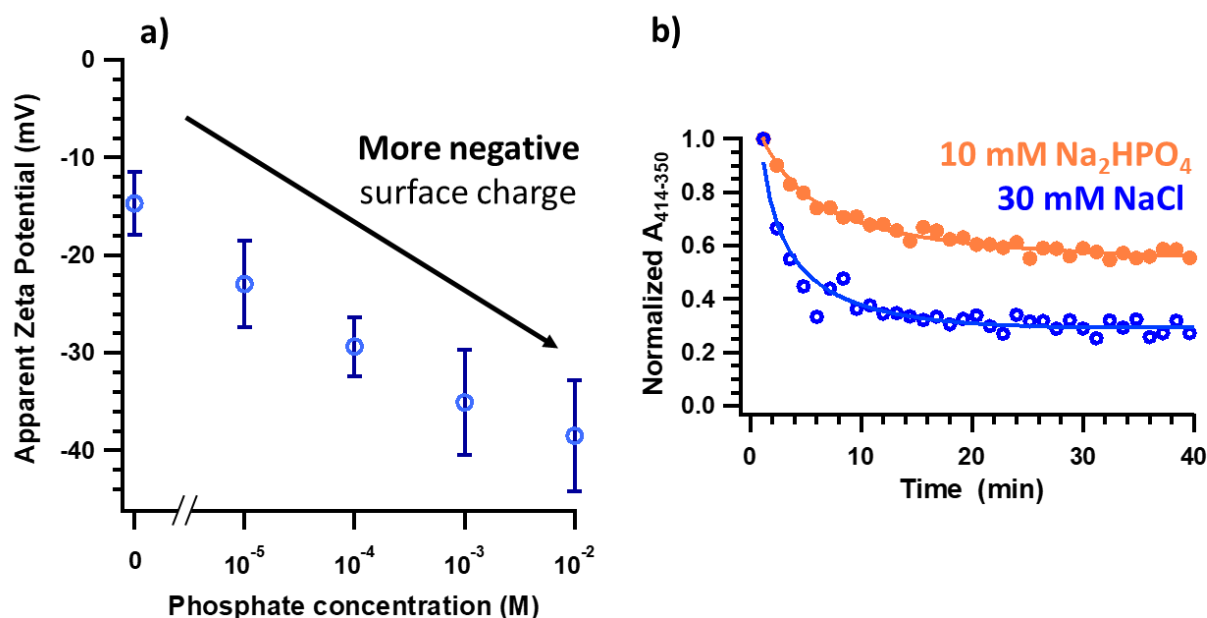
Figure I.9. a) zeta potential measurements of LCO in phosphate. b) UV-visible spectroscopy absorbance of LCO in suspension over time. Figure adapted from Reference 4.

I.5. Summary and perspective.

While this study was done on a simple model system, these results point to some important

factors to consider when trying to predict and understand nanoparticle fate and transport in the

environment. This study shows that molecules adsorbing, or sticking, to LCO, can change the

properties of the nanoparticle. In this case, phosphate adsorption changed the surface properties by making the charge more negative, which made the particles more stable in suspension. This may impact bioavailability of particles in environmental systems. If they are staying in suspension for longer times when phosphate is present, this may dictate if and how they encounter different organisms. For instance, phosphate adsorption may make LCO more accessible to surface water dwellers, such as fish. Studies by my collaborators have seen that LCO can enter fish gill cells and have negative impacts on their health.

Phosphate isn't present in every surface water system, and so researchers in the CSN are also studying how LCO impacts bottom-feeders such as chironomids, which are a type of fly that, as it's growing, lives in soil. It's important for us to gain an understanding of how LCO can impact environmental systems from every level – from the chemistry side, as I've presented here, and from a more biological side, which my coworkers study. Together, we in the Center for Sustainable Nanotechnology hope to use our combined knowledge and research findings to aid in the safe use and disposal of nanomaterials.

I.6. References.

1.   Feng, Z. V.; Gunsolus, I. L.; Qiu, T. A.; Hurley, K. R.; Nyberg, L. H.; Frew, H.; Johnson, K. P.; Vartanian, A. M.; Jacob, L. M.; Lohse, S. E.; Torelli, M. D.; Hamers, R. J.; Murphy, C. J.; Haynes, C. L., Impacts of gold nanoparticle charge and ligand type on surface binding and toxicity to Gram-negative and Gram-positive bacteria. *Chem Sci* **2015,** *6* (9), 5186-5196.

2.   Borgatta, J.; Ma, C.; Hudson-Smith, N.; Elmer, W.; Plaza Pérez, C. D.; De La Torre-Roche, R.; Zuverza-Mena, N.; Haynes, C. L.; White, J. C.; Hamers, R. J., Copper Based Nanomaterials Suppress Root Fungal Disease in Watermelon (Citrullus lanatus): Role of Particle Morphology,

Composition and Dissolution Behavior. *ACS Sustainable Chemistry & Engineering* **2018,** *6* (11), 14847-14856.

3.   Hamers, R.J., What's With All Those Flaming Cell Phones? A Primer on Battery Safety. In *Sustainable-Nano*, Sustainable-Nano, Ed. Sustainable-Nano: 2016; Vol. 2020.

4.   Laudadio, E. D.; Bennett, J. W.; Green, C. M.; Mason, S. E.; Hamers, R. J., Impact of Phosphate Adsorption on Complex Cobalt Oxide Nanoparticle Dispersibility in Aqueous Media. *Environ. Sci. Technol.* **2018,** *52*, 10186-10195.

Chapter 1. Introduction: A Perspective on Lithium Ion Batteries Cathode Materials and their Role in Global Sustainability: Resources, Recycling, and Environmental Impacts

"Humanity has the ability to make development sustainable to ensure that it meets the needs of the present without compromising the ability of future generations to meet their own needs."

- Definition of Sustainable Development, *Report of the World Commission on Environment and Development: Our Common Future*

1.1. Introduction.

The discovery and development of lithium-ion batteries (LIBs) in an otherwise fossil-fuel dependent world has raised the question, does this technology have the potential to secure a sustainable, distributed energy supply for modern civilization?[1] In order to answer this question, we must gain an understanding of the expense to or gains in environmental impact of lithium ion batteries at every stage: material mining and processing, battery pack assembly and integration, waste treatment or recycling, and consequences of unintentional release. The goal of this introduction is to provide perspective on the connectivity between manufacture and use, recycling, and unintentional release of complex metal oxides which comprise battery cathodes on the environmental impact of these materials. In this chapter the recent and relevant outcomes from life cycle assessment, research on metal recovery from spent materials, and our understanding of the environmental and toxicological effects of these materials will be reviewed to provide insight into the necessary considerations for the responsible development and use of the next generation of lithium ion batteries.

1.2. Lithium ion batteries.

A LIB consists of three main components: the anode, the cathode, and the electrolyte. The anode and the cathode are the two electrodes of the electrochemical cell. The battery is able to operate due to the intrinsic chemical potential difference between the two electrodes, establishing a potential gradient. As the battery discharges, the negative electrode (the anode for LIBs) undergoes oxidation, as Li^+ is released into the electrolyte and electrons are passed through a current collector. The electrolyte is commonly a liquid, consisting of a salt and (usually organic) solvent, that aid in the transport of lithium from one electrode to the other during the battery charge/discharge process. The electrolyte exists between the two solid electrodes, which are kept apart by an electrolyte-permeable separator. The most common electrolyte system used in commercial batteries today consists of lithium hexafluorophosphate ($LiPF_6$) as the salt, in a solvent of cyclic and linear carbonates. One Li^+ is transported to the positive electrode (the cathode for LIBs) for each electron passed through the electrical circuit. A key characteristic of LIBs is the ability for this process to be reversed; by applying an external electricity source, the battery can be charged again, such that the battery can be charged and discharged for many cycles over a relatively long lifetime.

The ability to charge and discharge a battery using a lithium-intercalating material was first demonstrated in the 1970's using TiS_2.[2-3] The first commercialized LIB was produced by Sony,[4-5] using lithium cobalt oxide ($LiCoO_2$) as a cathode material, which was discovered by John B. Goodenough in 1980.[6-7] Since Goodenough's discovery of the promise of metal oxide materials for lithium intercalating cathodes, many commercialized batteries have used such materials. The pioneers of LIBs, John B. Goodenough, M. Stanly Whittingham, and Akira Yoshino won the

Nobel Prize in Chemistry in 2019 for this work, an acknowledgement of the incredible impact this technology has had on our society.

1.2.1. Metal oxides as LIB cathodes.

The energy density of LIBs is more or less dictated by the cathode, as the achievable energy density is greatly inferior to that of the anode.[8] $LiCoO_2$ cathodes have high energy density attributed to the two-dimensional channel for migration of Li^+, electrical conductivity from the octahedral edge-shared CoO_6 array, and a high theoretical capacity of 274 mAh/g.[9] However, only about half of the theoretical capacity can be achieved due to the physical/chemical instabilities of the crystal structure resulting from the oxidation of Co^{3+} to Co^{4+} as Li^+ migrates to the anode. This motivated the search for higher-capacity cathode materials by replacing cobalt with other electroactive transition metals.

$LiNiO_2$ and $LiMnO_2$ were among the earliest alternatives to $LiCoO_2$ explored for LIB cathode materials. $LiNiO_2$ in theory has less structural instability than $LiCoO_2$, however it suffers from Ni^{2+} migration into the Li^+ sites, which lowers the battery capacity over time. $LiMnO_2$ has a higher theoretical capacity than $LiCoO_2$, and has a high power density, with the added advantages of being more environmentally benign and inexpensive.[9] However, it is harder to synthesize in the layered structure, resulting in poor cycle life.

These investigations lead to increased interest in mixed transition metal cathodes, as they have synergistic benefits over single transition metals. Lithium nickel cobalt oxide (NC) was shown to be more structurally stable than pure $LiNiO_2$,[10] though the material suffers from lower conductivity.[11] Lithium nickel manganese cobalt oxide, $LiNi_xMn_yCo_{1-x-y}O_2$ ($0 \leq x \leq 1$, $0 \leq y \leq 1$, $0 \leq x + y \leq 1$), abbreviated NMC, was first explored as a cathode material in 1999.[12-13] NMC benefits from the high charge capacity of $LiNiO_2$, the rate capability of $LiCoO_2$, with added

structural stability from Mn^{4+}.[9] However, these materials still have lower electrical conductivity than $LiCoO_2$. The Mn^{4+} is not electroactive, and capacity is largely dictated by nickel content. Increasing the nickel content in NMC cathodes leads to higher capacity, due to the two-stage oxidation of Ni^{2+}/Ni^{3+} and Ni^{3+}/Ni^{4+}. For instance, the specific capacity of NMC111 (x = y = 0.33) is around 160 mAh/g, while NMC811 (x = 0.8, y = 0.1) has a specific capacity closer to 200 mAh/g.[14] As the nickel fraction approaches 1, the structural and thermal stability issues seen in pure $LiNiO_2$ begin to dominate. High nickel content NMC or NC materials are economically preferred due to the lower cost and higher global availability of nickel over cobalt, so much research is focused on optimizing these materials. Other modifications to the NMC class of materials include utilizing core-shell structures with a Ni-rich core and Mn-rich shell,[15] full concentration-gradient NMC,[16] and Li-rich and Mn-rich oxides.[17]

One of the complications with using LIBs for electric vehicles (EVs) is the fact that the capacity is directly related to the amount of the material. For EVs, high capacity is required, yet it would be ideal to limit the volume of material necessary in the cathode. One potential solution to this is the use of nanostructured and nanoparticulate materials for the cathodes. Advantages of nanomaterials for LIBs include reduced diffusion lengths of ions and electrons due to the decreased primary particle size and increased surface area-to-volume ratio.[8] This can lead to faster charge/discharge times, and in some cases greater mechanical stability.[18] The expansion and contraction of the cathode as a function of lithiation and delithiation can cause material fracture, such that bulk, commercial cathode materials at end-of-life may in fact contain nanostructured and nanoparticulate materials.[19-20]

1.2.2. LIBs for electric vehicles.

As the development and performance of LIBs continued to improve, it was clear they showed promise for use in EVs. EVs have the potential to significantly increase sustainability of transportation, as significant portion of greenhouse gas (GHG) emissions are a result of the fossil fuel-based transport sector.[21] While early iterations of the electric vehicle operated with lead-acid, nickel metal-hydride or sodium-nickel-chloride batteries, LIBs are ideal for EVs due to both lithium being the lightest metal, and one with great electrochemical potential, allowing for high power and energy density. Environmental burdens of vehicles, electric or internal combustion engine, are largely dominated by the operation phase, regardless of engine type.[24] Therefore, while the use of EVs themselves emit less CO_2 than their fuel-engine counterparts, if the electricity generated for recharging LIBs is primarily from oil or coal-fired plants, the CO_2 emissions of an electric vehicle can sometimes be higher than that of a traditional vehicle.[22] Another factor to consider for the sustainability of these materials is their end-of-life. There is projected to be between 40 and 70 million LIB-containing EVs by 2025,[23] and such growth will also be accompanied by a massive increase in the number of spent batteries.

1.3. Life cycle assessment.

There is an impression that the advent of EVs will undoubtedly be a beneficial transition for our environment. Of course, limiting our reliance on fossil fuels is essential to protecting our atmosphere, however, in actuality, there are additional factors to consider. One way to assess and predict the environmental burdens or benefits of EVs is through the implementation of life cycle assessment (LCA). LCA is an analytical method that allows for the estimation of the total environmental impacts associated with the production and use of products. The technique operates by taking inventory of all exchanges with the environment and all energy inputs across the various

stages of development and consumption of the product: materials extraction to processing and manufacturing (cradle-to-gate), use and end of life of the product (cradle-to-grave), and the potential for recycling and reuse of the spent materials (cradle-to-cradle). LCA helps to identify particularly energy intensive areas that should be improved upon to make the manufacturing and use of a material more sustainable.

1.3.1. Raw material extraction.

Nickel mining, while the impacts of which have improved over time, has had significant historical impacts including acid rain from SO_2 emissions, soil contamination, wetland acidification, biodiversity loss, vegetation die back, soil erosion, and coral reef contamination. Cobalt is often a byproduct or co-productive of nickel or copper mining, and so the local environmental impacts are similar to those listed above. Cobalt-dominant mining efforts have unique environmental and health challenges as they often tap arsenide ores. Lithium recovery is less energy and emissions intensive than recovery of cobalt and nickel, and is available from natural brines, ore or seawater, with recovery from brines dominating the supply. While lithium used for batteries represented 14% of the lithium demand in 2010, by 2025 it is projected to represent over 75%. Similarly, for cobalt, the percent of the demand increases from 25% to a projected 53% by 2025.[25]

1.3.2. Materials processing and manufacturing.

Different assessment methods yielded different results about what was the most impactful part of the battery to produce, cathode or anode. The copper needed for the collector foil in the anode accounted for over 40% of the environmental burden of the battery, while the cathode collector, made of aluminum foil, also comes with significant impact.[24] The use of these metals is more burdensome than the lithium itself, since ultimately the lithium content only accounts for 7

g per kg of active material, and though lithium is considered a scarce metal, the processes to extract lithium from brines are simple and have low energy demand.[24] Notter et al. found that the lithium in the cathode material yielded more of an environmental burden than the $LiPF_6$ in the battery electrolyte, and that the production of the cathode itself has high environmental impact due to the release of considerable amounts of CO_2. The production of the LIB causes damage to human health as a function of the inorganic emissions from the processing, as well as the reliance of fossil fuels and minerals within the production process. The primary cathode material considered in this model is $LiMn_2O_4$, though the results show that switching to NMC333 resulted in a 12.8% increase in environmental burden. The ultimate result of the study is that the environmental burden mostly comes from operation, where as long as the electricity for the EV is not being produced by a renewable source, the burden is still high.[24]

Battery assembly itself is also an energy intensive process. The assembly involves producing the electrodes by mixing the cathode or active material with a binder in a solvent to achieve a homogenous slurry. A coating process applies an aluminum foil that functions as a current collector to the cathode and a copper foil to the anode. A separator is placed between the electrodes, the electrolyte is added and the cells are sealed. The batteries are aged and then assembled into the battery packs to be installed.[26] Dunn et al performed a more detailed assessment of the environmental impact of battery assembly (versus materials production) after noting a large variability amongst published analysis of the burdens of EV LIBs based on discrepancies within this step.[26] They found that the cradle-to-gate energy consumption in the production of cathode materials varied significantly on cathode composition, with $LiCoO_2$ being the most energy expensive, followed by NMC333, with $LiFePO_4$ and $LiMn_2O_4$ being the least energy expensive. The production of $LiCoO_2$ and NMC333 accounts for the majority of the energy intensity for

batteries that use these cathode materials at about 40%, whereas for $LiMn_2O_4$ and $LiFePO_4$ the cathode production is 10-20%, and the aluminum drives the overall energy intensity at about 40%. The SO_2 and GHG emissions for production of each cathode material follow this trend. This is largely due to the energy-intensive and high-emission steps of recovering cobalt and nickel from ores. However, it is worth noting that cathode materials that do not contain cobalt or nickel commonly have lower specific energies than those that do, which can mean more material is needed per battery to achieve the same performance.[26]

To maximize the climate change mitigation benefits that can be accomplished with EVs, it is necessary to improve both electrochemical performance and lessen the environmental impact of production.[8] It is possible that the incorporation of nanomaterials can ultimately lessen environmental impact, however currently the production of nanomaterials is often more energy demanding.[8] The use of recycled materials to generate new batteries is also potential option, though this area requires significant development, as discussed later.

1.3.3. Use.

Notter et al. performed a life cycle analysis (LCA) on EVs with a functional unit of one kilometer driven, and found that PM_{10}^-, NO_x^- and SO_2 emissions from an EV was higher than a traditional vehicle, with the production of the battery also emitting considerable amounts.[24] Life cycle analysis studies have concluded that while EV production is 10-40% more energy intensive than producing conventional vehicles, operating an EV then consumes 1.6-3.4 times less energy on a per kilometer basis. While greenhouse gas emission from EV production is higher than conventional vehicles, because EVs do not emit greenhouse gases during use, the emissions "debt" is paid back within the first 25,000 kilometers using a national average grid to charge the vehicle.

However, the source of the electricity in the grid will impact how clean of a process charging an EV is.[26]

1.3.4. End of life: E-waste disposal and recycling opportunities.

A consequence of rapid technological innovation is early obsolescence of devices, which contributes significantly to the tens of millions of tons of e-waste, or electronic waste, generated yearly.[27-28] There are currently no federal disposal regulations for LIBs.[29] It is projected that by 2030, there will be about 11 million tons of spent LIB accumulation, in which batteries from EVs constitute a large portion.[25] The cathode alone comprises from 25-30% of the batteries total weight.[29] Of e-waste, 70% consists of metals. 80% of e-waste from the United States is exported to Asia, 90% of which is sent to China.[30] In the regions where this waste is maintained, higher concentrations of contaminants in air, soils and sediments has been seen.[28] Primitive recycling efforts can have significant health impacts for the workers, as well as the environment.[31]

A challenge faced in recycling LIB cathode materials is the ability to economically and efficiently recover resources from cathodes with different chemistries.[32] The recovery process has two steps; physical separation of the battery components, then chemical leaching and separation of the specific elements. In a commonly used recycling method, batteries are introduced into a furnace and smelted, which forms an alloy of copper, cobalt, nickel and iron. Through a series of leaching, solvent extraction and purification, the metal alloy is separated into Cu, Fe, $Ni(OH)_2$ and CoO. Lithium exits the furnace in a slag, and recovery is not economically viable. Because cobalt recovery drives the process economics, cobalt containing cathode materials may be the only ones realistically prioritized for recycling. Recovery of cobalt is less energy intensive than the mining and smelting of virgin material, and so the SO_2 and greenhouse gas emissions from recycling cobalt and using recycled cobalt in the manufacturing process are less than starting the process from

mining material. The chemical leaching is often done in dilute strong acid (HCl, HNO$_3$, and H$_2$SO$_4$ being leading solvents) whereas a variety of separation techniques have been explored, including solvent extraction, and solid state reactions.[33]

Recent benchtop-scale efforts have tested leaching the metals out of the cathode using H$_2$SO$_4$ and H$_2$O$_2$ instead of HCl for reduced environmental impact, and have leveraged the different solubility constants of the hydroxides to recover iron impurities first, followed by nickel, cobalt and manganese in a co-precipitate.[32] Recycled cathode material could then be synthesized from the coprecipitate, as well as recovered LiCO$_3$, which eliminates the need for an additional isolation step of the coprecipitate before reintroduction into the production scheme.

The cost of synthesizing NMC333 is \$16,635/ton from virgin materials, and only \$6,195/ton using this recovery method.[32] Other work has focused on mitigating both environmental and health impacts of the leaching solution by investigating weaker organic acids, such as succinic acid[34], citric acid[35], malic acid[36], oxalic acid[37], tartaric acid[38], glucose[39], and ascorbic acid[40-41], with many of these having efficiencies higher than 90% for both transition metals and lithium.

1.4. Environmental implications.

Considering that <5% of LIBs produced are currently recycled,[42] and the millions of tons of waste being produced[27-31], it is inevitable that these materials are going to be released into the environment. It has already been seen that the treatment of e-waste has hazardous impacts to humans, and that there is increased environmental contamination in the regions with high reserves of e-waste.[28, 31] A significant research effort of the Center for Sustainable Nanotechnology has been the investigation of the biological and environmental impacts of nanomaterials of LiCoO$_2$ and NMC. Because of the potential advantages of using nanomaterials for LIB cathodes,[8] and

because the current commercial materials are often fractured into nanoparticulate matter by end-of-life,[19-20] these studies have focused on investigating the impacts of nanoparticles of common cathode materials.

1.4.1. Biological impacts.

Investigations of the environmental and biological effects of this class of materials has revealed several important factors to consider when assessing the toxicity and/or impact of lithium intercalation compounds. Exposure of equistoichiometric $LiNi_{0.33}Mn_{0.33}Co_{0.33}O_2$ (NMC333) nanosheets to model soil bacterium *Shewanella oneidensis* showed that Ni^{2+} and Co^{2+} released into solution from the materials was the major mode of toxicity to the bacteria.[20] This study also revealed an unexpected incongruent dissolution of metals from the nanomaterial; with Ni^{2+} being released in the highest concentrations, followed by Co^{2+} and then Mn^{4+}, despite the equal stoichiometry of all three metals in the starting material. This result was corroborated by Density functional theory (DFT) simulations that show a more energetically favorable release of Ni^{2+} from the material.

The implication that dissolved ions were the major mode of toxicity, at least in this model system, inspired a follow-up study aimed towards synthesizing a more benign NMC. The composition of NMC nanosheets was tuned such that a suite of high-manganese content ($LiNi_{0.31}Mn_{0.39}Co_{0.30}O_2$, $LiNi_{0.23}Mn_{0.55}Co_{0.22}O_2$, $LiNi_{0.14}Mn_{0.72}Co_{0.14}O_2$) particles could be compared.[43] These materials retained the morphology and crystal structure of the parent equistoichiometric NMC, allowing for a direct comparison of the toxicity to *S. onedensis*. Consistent with the prior study, it was seen that increasing the amount of manganese in the material core resulted in less ion release of Ni^{2+} and Co^{2+} into solution, and therefore lower toxicity to *S. oneidensis*.

While increasing manganese content in NMC mitigates some biological impact, high manganese materials are expected to be less efficient as cathode materials. In NMC the electroactive elements are Ni^{2+} and Co^{3+}, which are oxidized to Ni^{3+} and Co^{4+} as the battery discharges. The role of manganese is mostly structural, and therefore increasing its content reduces the capacity of the battery. Industry is moving towards higher nickel content NMC materials, as nickel is both electroactive and also significantly cheaper than cobalt. Using the same synthetic control developed in the manganese content study, a suite of high-nickel NMC materials were investigated for their biological impact. Unexpectedly, increasing nickel content did not increase nickel release from the materials, and it was found that the toxicity of NMC333 and NMC622 to *S. oneidensis* was comparable.[44] DFT simulations of the dissolution of these materials revealed that the increased concentration of Ni^{4+} in high nickel NMC as opposed to Ni^{2+} stabilized it in the lattice, resulting in less total release of nickel ions than hypothesized. As had been seen previously[20, 43], the impact to *S. oneidensis* was heavily contributed to the release of ions from the nanomaterial.

A similar outcome that ion release dictates NMC toxicity has been seen for Gram-positive bacterium *Bacilus subtilis* in addition to Gram-negative bacterium *S. oneidensis.* It was found that the growth curve of *B. subtilis* in the presence of the concentration of dissolved Ni^{2+} ions alone recapitulated the nanoparticle response.[45] The difference in the composition of the growth medium between the two bacteria result in a difference in speciation of the released ions in solution, which resulted in more significant toxicological impacts to *B. subtilis* than *S. oneidensis* at comparable nanoparticle concentrations. The *S. oneidensis* medium contains 100 mM sodium lactate as the carbon source, and speciation calculations suggest the majority of released ions exist in complexed forms with lactate.[20] However, the carbon source in the *B. subtilis* medium is 10 mM dextrose,

which does not complex with the dissolved ions, and therefore the majority of them exist as free ions in solution. The result of this is that while the respiratory impacts of NMC to *S. oneidensis* were a delayed onset of oxygen uptake that eventually reached the same level of oxygen consumption as healthy bacteria, for the gram positive bacterium *B. subtilis* exposed to the same concentration of NMC, the same levels of oxygen uptake were never achieved.

While both Gram-negative and Gram-positive bacteria show toxicological responses to metal ion release from NMC nanomaterials, this effect is not generalizable to other organisms. The impact of NMC333 and LiCoO$_2$ to the fresh-water organism *Daphnia magna* was found to not be related to ion release from the materials.[46] Both NMC333 and LiCoO$_2$ impacted the survival, reproduction, and size of *D. magna* in a dose-dependent manner, and the particles were seen both to adhere to the carapace of the organism and also accumulate within the digestive tract. Gene expression changes between control groups, ion only groups and nanoparticle-exposed groups were also in support of a nano-specific impact to the organisms. Another investigation of the impact of LiCoO$_2$ on rainbow trout epithelial cells found that cell viability was impacted at nanoparticle exposure concentrations as low as 10 mg/L, and yet cell exposure to Li$^+$ and Co^{2+} ions alone did not reduce cell viability.[47-48]

Expanding our understanding of the impact of these materials on biological systems beyond the "toxic" dose is necessary to develop a picture of the long-term implications of continuous exposure. Upon chronic exposure to NMC333, *S. oneidensis* have been seen to develop a resistance to the material that persists over multiple generations.[49] NMC333 has been shown to cause DNA damage in both *S. oneidensis* and *B. subtilis*.[45] Gene expression analysis after LiCoO$_2$ exposure to the benthic organism *Chironomous riparius* reveal significant disruption of genes

related to heme synthesis.[50] There is a continued effort to elucidate the impacts of these materials on organisms across multiple organisms and methods of exposure.

1.4.2 Chemical transformations.

The field of nano-environmental health and safety (nanoEHS) has expanded over the past two decades.[51-55] While the early stages of this field focused on simpler model nanomaterials, such as gold, silver, and single-transition metal oxides, there is an increasing need to expand our understanding of the potential fate and transport of engineered nanomaterials in the environment to include more complex and technologically relevant materials. One aspect of this field is the characterization of the transformations of nanomaterials in complex model and actual environmental systems.[56-57] While the work in the following thesis is one step towards the understanding of the transformations of cathode materials (specifically $LiCoO_2$) in the environment, the environmental transformations of these complex metal oxides is only just starting to be investigated. Existing work of these transformations on more simple model nanomaterials provides guiding principles and clarifies potential transformations that led to the considerations for the studies that follow, such as molecular adsorption[58-60], corona formation[61-62], material dissolution[63-64], aggregation and sedimentation,[65] and reactive oxygen species generation.[66]

1.5. Scope of Thesis.

The development and use of LIBs has been recognized worldwide as one of the greatest technological advances in our lifetimes. While the potential of LIBs to contribute to global sustainability is significant, there is still a lot of work to be done in this area. The major areas of continued development and research are 1) cathode material optimization, both in terms of composition and structuring; 2) mitigating total environmental impacts from materials mining, device production, and recycling; and 3) work to understand the potential environmental impacts

of LIBs released into the environment, to aid design of safer materials. Considering the massive scale at which LIBs are produced and the lack of well-defined disposal or recycling streams for spent materials, a continued focus on how to mitigate the environmental impacts of the materials currently being released into the environment is key.

The work in the following thesis aims to provide some insight into the third area of concern, understanding the potential environmental impacts of released cathode materials. The work presented here is some of the first studies on environmentally-mediated chemical transformations of electroactive materials such as $LiCoO_2$. Within this thesis a toolkit for in situ analysis of the nanoparticle surface – liquid interface is established, and the complementary information that each technique yields aids in the understanding of how this material is transformed in suspension, through oxyanion adsorption, organic acid-mediated transition metal dissolution, and how these transformations impact the particle composition, charge, and stability in aqueous systems.

1.6. References.

1.   Goodenough, J. B.; Park, K. S., The Li-ion rechargeable battery: a perspective. *J Am Chem Soc* **2013,** *135* (4), 1167-76.

2.   Whittingham, M. S., Electrical Energy Storage and Intercalation Chemistry. *Science* **1976,** *192*, 1126-1127.

3.   Whittingham, M. S., The Role of Ternary Phases in Cathode Reactions. *J. Electrochem. Soc.* **1976,** *123*, 315-320.

4.   Nagaura, T.; Tozawa, K., Lithium ion rechargeable battery. *Prog. Batteries Solar Cells* **1990,** *9*, 209.

5.   Ozawa, K., Lithium-ion rechargeable batteries with LiCoO2 and carbon electrodes: the LiCoO2/C system. *Solid State Ionics* **1994,** *69*.

6.   Goodenough, J. B., Design considerations. *Solid State Ionics* **1994,** *69*, 184-198.

7.   Mizushima, K.; Jones, P. C.; Wiseman, P. J.; Goodenough, J. B., LixCoO2: A New Cathode Material for Batteries of High Energy Density. *Mat. Res. Bull* **1980,** *15*, 783-789.

8.   Ellingsen, L. A.; Hung, C. R.; Majeau-Bettez, G.; Singh, B.; Chen, Z.; Whittingham, M. S.; Stromman, A. H., Nanotechnology for environmentally sustainable electromobility. *Nat Nanotechnol* **2016,** *11* (12), 1039-1051.

9.   Kim, T.; Song, W.; Son, D.-Y.; Ono, L. K.; Qi, Y., Lithium-ion batteries: outlook on present, future, and hybridized technologies. *Journal of Materials Chemistry A* **2019,** *7* (7), 2942-2964.

10.   Rougier, A.; Saadouane, I.; Gravereau, P.; Willmann, P.; Delmas, C., Effect of cobalt substitution on cationic distribution in LiNi1− y CoyO2 electrode materials. *Solid State Ionics* **1996,** *90*.

11.   Saadouane, I.; Delmas, C., LiNi1–yCoyO2 positive electrode materials: relationships between the structure, physical properties and electrochemical behaviour. *J. Mater. Chem.* **1996,** *6*, 193.

12.   Liu, Z.; Yu, A.; Lee, J. Y., Synthesis and characterization of LiNi1− x− yCoxMnyO2 as the cathode materials of secondary lithium batteries. *Journal of Power Sources* **1999,** *81-82*, 416.

13.   Yoshio, M.; Noguchi, H.; Itoh, J.-i.; Okada, M.; Mouri, T., Preparation and properties of LiCoyMnxNi1− x− yO2 as a cathode for lithium ion batteries. *Journal of Power Sources* **2000,** *90*, 176.

14.   Schmuch, R.; Wagner, R.; Hörpel, G.; Placke, T.; Winter, M., Performance and cost of materials for lithium-based rechargeable automotive batteries. *Nature Energy* **2018,** *3* (4), 267-278.

15.   Sun, Y.-K.; Myung, S.-T.; Kim, M.-H.; Prakash, J.; Amine, K., Synthesis and characterization of Li[(Ni0.8Co0.1Mn0.1)0.8(Ni0.5Mn0.5)0.2]O2 with the microscale core−shell structure as the positive electrode material for lithium batteries. *J Am Chem Soc* **2005,** *127*, 13411-13418.

16.   Lim, B.-B.; Myung, S.-T.; Yoon, C. S.; Sun, Y.-K., Comparative study of Ni-rich layered cathodes for rechargeable lithium batteries: Li[Ni0.85Co0.11Al0.04]O2 and Li[Ni0.84Co0.06Mn0.09Al0.01]O2 with two-step full concentration gradients. . *ACS Energy Lett.* **2016,** *1*, 283-289.

17.   Qiu, B.; Zhang, M.; Wu, L.; Wang, J.; Xia, Y.; Qian, D.; Liu, H.; Hy, S.; Chen, Y.; An, K.; Zhu, Y.; Liu, Z.; Meng, Y. S., Gas–solid interfacial modifcation of oxygen activity in layered oxide cathodes for lithium-ion batteries. *Nat. Commun.* **2016,** *7*, 12108-12118.

18.   Hamers, R. J., Energy Storage Materials as Emerging Nano-Contaminants. *Chem. Res. Toxicol.* **2020**, Just Accepted.

19.   Zhu, M.; Park, J.; Sastry, A. M., Fracture analysis of the cathode in Li-ion batteries: A simulation study. . *J. Electrochem. Soc.* **2012,** *159*, A492-498.

20.   Hang, M. N.; Gunsolus, I. L.; Wayland, H.; Melby, E. S.; Mensch, A. C.; Hurley, K. R.; Pedersen, J. A.; Haynes, C. L.; Hamers, R. J., Impact of Nanoscale Lithium Nickel Manganese Cobalt Oxide (NMC) on the Bacterium Shewanella oneidensis MR-1. *Chemistry of Materials* **2016,** *28*, 1092-1100.

21.   Dominković, D. F.; Bačeković, I.; Pedersen, A. S.; Krajačić, G., The future of transportation in sustainable energy systems: Opportunities and barriers in a clean energy transition. *Renewable and Sustainable Energy Reviews* **2018,** *82*, 1823-1838.

22.   Shareef, H.; Islam, M. M.; Mohamed, A., A review of the stage-of-the-art charging technologies, placementmethodologies, and impacts of electric vehicles. *Renewable and Sustainable Energy Reviews* **2016,** *64*, 403-420.

23.   Zhang, X.; Li, L.; Fan, E.; Xue, Q.; Bian, Y.; Wu, F.; Chen, R., Toward sustainable and systematic recycling of spent rechargeable batteries. *Chem Soc Rev* **2018,** *47* (19), 7239-7302.

24.   Notter, D. A.; Gauch, M.; R., W.; Wagner, P.; Stamp, A.; Zah, R.; Althaus, H.-J., Contribution of Li-Ion Batteries to the Environmental Impact of Electric Vehicles. *Environ. Sci. Technol.* **2010,** *44*, 6550-6556.

25.   Zeng, X.; Li, M.; Abd El-Hady, D.; Alshitari, W.; Al-Bogami, A. S.; Lu, J.; Amine, K., Commercialization of Lithium Battery Technologies for Electric Vehicles. *Advanced Energy Materials* **2019,** *9* (27).

26.   Dunn, J. B.; Gaines, L.; Kelly, J. C.; James, C.; Gallagher, K. G., The significance of Li-ion batteries in electric vehicle life-cycle energy and emissions and recycling's role in its reduction. *Energy Environ. Sci.* **2015,** *8* (1), 158-168.

27.   Widmer, R.; Oswald-Krapf, H.; Sinha-Khetriwal, D.; Schnellmann, M.; Böni, H., Global perspectives on e-waste. *Environmental Impact Assessment Review* **2005,** *25* (5), 436-458.

28.   Zhang, K.; Schnoor, J. L.; Zeng, E. Y., E-waste recycling: where does it go from here? *Environ Sci Technol* **2012,** *46* (20), 10861-7.

29.   Winslow, K. M.; Laux, S. J.; Townsend, T. G., A review on the growing concern and potential management strategies of waste lithium-ion batteries. *Resources, Conservation and Recycling* **2018,** *129*, 263-277.

30.   Hicks, C.; Dietmar, R.; Eugster, M., The recycling and disposal of electrical and electronic waste in China—legislative and market responses. *Environmental Impact Assessment Review* **2005,** *25* (5), 459-471.

31.   Wong, M. H.; Wu, S. C.; Deng, W. J.; Yu, X. Z.; Luo, Q.; Leung, A. O.; Wong, C. S.; Luksemburg, W. J.; Wong, A. S., Export of toxic chemicals - a review of the case of uncontrolled electronic-waste recycling. *Environ Pollut* **2007,** *149* (2), 131-40.

32.   Zou, H.; Gratz, E.; Apelian, D.; Wang, Y., A novel method to recycle mixed cathode materials for lithium ion batteries. *Green Chemistry* **2013,** *15* (5).

33.   Wang, R.-C.; Lin, Y.-C.; Wu, S.-H., A novel recovery process of metal values from the cathode active materials of the lithium-ion secondary batteries. *Hydrometallurgy* **2009,** *99* (3-4), 194-201.

34.   Li, L.; Qu, W.; Zhang, X.; Lu, J.; Chen, R.; Wu, F.; Amine, K., Succinic acid-based leaching system: A sustainable process for recovery of valuable metals from spent Li-ion batteries:. *Journal of Power Sources* **2015,** *282*, 544-551.

35.   Li, L.; Ge, J.; Wu, F.; Chen, R.; Chen, S.; Wu, B., Recovery of cobalt and lithium from spent lithium ion batteries using organic citric acid as a leachant. *Journal of Hazardous Materials* **2010,** *176*, 288-293.

36.   Sun, C.; Xu, L.; Chen, X.; Qiu, T.; Zhou, T., Sustainable recovery of valuable metals from spent lithium-ion batteries using DL-malic acid: Leaching and kinetics aspect. *Waste Manag Res* **2018,** *36* (2), 113-120.

37.   Sun, L.; Qiu, K., Organic oxalate as leachant and precipitant for the recovery of valuable metals from spent lithium-ion batteries. *Waste Management* **2012,** *32*, 1575-1582.

38.   Nayaka, G. P.; Pai, K. V.; Santhosh, G.; Manjanna, J., Dissolution of cathode active material of spent Li-ion batteries using tartaric acid and ascorbic acid mixture to recover Co. *Hydrometallurgy* **2016,** *161*, 54-57.

39.   Chen, X.; Fan, B.; Xu, L.; Zhou, T.; Kong, J., An atom-economic process for the recovery of high value-added metals from spent lithium-ion batteries. *Journal of Cleaner Production* **2016,** *112*, 3562-3570.

40.   Li, L.; Lu, J.; Ren, Y.; Zhang, X.; Chen, R.; Wu, F.; Amine, K., Ascorbic-acid-assisted recovery of cobalt and lithium from spent Li-ion batteries. *Journal of Power Sources* **2012,** *218*, 21-27.

41.   Nayaka, G. P.; Pai, K. V.; Manjanna, J.; Keny, S. J., Use of mild organic acid reagents to recover the Co and Li from spent Li-ion batteries. *Waste Manag* **2016,** *51*, 234-238.

42.	Kang, D. H.; Chen, M.; Ogunseitan, O. A., Potential environmental and human health impacts of rechargeable lithium batteries in electronic waste. *Environ Sci Technol* **2013,** *47* (10), 5495-503.

43.	Gunsolus, I. L.; Hang, M. N.; Hudson-Smith, N. V.; Buchman, J. T.; Bennett, J. W.; Conroy, D.; Mason, S. E.; Hamers, R. J.; Haynes, C. L., Influence of nickel manganese cobalt oxide nanoparticle composition on toxicity toward Shewanella oneidensis MR-1: redesigning for reduced biological impact. *Environ. Sci.: Nano* **2017,** *4* (3), 636-646.

44.	Buchman, J. T.; Bennett, E. A.; Wang, C.; Abbaspour Tamijani, A.; Bennett, J. W.; Hudson, B. G.; Green, C. M.; Clement, P. L.; Zhi, B.; Henke, A. H.; Laudadio, E. D.; Mason, S. E.; Hamers, R. J.; Klaper, R. D.; Haynes, C. L., Nickel enrichment of next-generation NMC nanomaterials alters material stability, causing unexpected dissolution behavior and observed toxicity to S. oneidensis MR-1 and D. magna. *Environmental Science: Nano* **2020,** *7*, 571-587.

45.	Feng, Z. V.; Miller, B. R.; Linn, T. G.; Pho, T.; Hoang, K. N. L.; Hang, M. N.; Mitchell, S. L.; Hernandez, R. T.; Carlson, E. E.; Hamers, R. J., Biological impact of nanoscale lithium intercalating complex metal oxides to model bacterium B. subtilis. *Environ Sci Nano* **2019,** *6* (1), 305-314.

46.	Bozich, J.; Hang, M.; Hamers, R.; Klaper, R., Core Chemistry Influences the Toxicity of Multicomponent Metal Oxide Nanomaterials, Lithium Nickel Manganese Cobalt Oxide, and Lithium Cobalt Oxide to *Daphnia magna*. *Environmental Toxicology and Chemistry* **2017,** *36* (9), 2493-2592.

47.	Melby, E. S.; Cui, Y.; Borgatta, J.; Mensch, A. C.; Hang, M. N.; Chrisler, W. B.; Dohnalkova, A.; Van Gilder, J. M.; Alvarez, C. M.; Smith, J. N.; Hamers, R. J.; Orr, G., Impact of

lithiated cobalt oxide and phosphate nanoparticles on rainbow trout gill epithelial cells. *Nanotoxicology* **2018,** *12* (10), 1166-1181.

48.   Mensch, A. C.; Mitchell, H. D.; Markillie, L.; Laudadio, E. D.; Schwartz, M. P.; Hamers, R. H.; Orr, G., Impact of toxic and subtoxic doses of lithium cobalt oxide nanoparticles and their ions on molecular pathways in trout gill epithelial cells. . *Environ. Sci.: Nano* **2020**, Under Review.

49.   Mitchell, S. L.; Hudson-Smith, N. V.; Cahill, M. S.; Reynolds, B. N.; Frand, S. D.; Green, C. M.; Wang, C.; Hang, M. N.; Hernandez, R. T.; Hamers, R. J.; Feng, Z. V.; Haynes, C. L.; Carlson, E. E., Chronic exposure to complex metal oxide nanoparticles elicits rapid resistance in Shewanella oneidensis MR-1. *Chem Sci* **2019,** *10* (42), 9768-9781.

50.   Niemuth, N. J.; Curtis, B. J.; Hang, M. N.; Gallagher, M. J.; Fairbrother, D. H.; Hamers, R. J.; Klaper, R. D., Next-Generation Complex Metal Oxide Nanomaterials Negatively Impact Growth and Development in the Benthic Invertebrate Chironomus riparius upon Settling. *Environ Sci Technol* **2019,** *53* (7), 3860-3870.

51.   Grassian, V. H.; Haes, A. J.; Mudunkotuwa, I. A.; Demokritou, P.; Kane, A. B.; Murphy, C. J.; Hutchison, J. E.; Isaacs, J. A.; Jun, Y.-S.; Karn, B.; Khondaker, S. I.; Larsen, S. C.; Lau, B. L. T.; Pettibone, J. M.; Sadik, O. A.; Saleh, N. B.; Teague, C., NanoEHS – defining fundamental science needs: no easy feat when the simple itself is complex. *Environ. Sci.: Nano* **2016,** *3*, 15-27.

52.   Nowack, B.; Ranville, J. F.; Diamond, S.; Gallego-Urrea, J. A.; Metcalfe, C.; Rose, J.; Horne, N.; Koelmans, A. A.; Klaine, S. J., POTENTIAL SCENARIOS FOR NANOMATERIAL RELEASE AND SUBSEQUENT ALTERATION IN THE ENVIRONMENT. *Environmental Toxicology and Chemistry* **2012,** *31* (1), 50-59.

53.   Mahapatra, I.; Clark, J. R. A.; Dobson, P. J.; Owen, R.; Lynch, I.; Lead, J. R., Expert perspectives on potential environmental risks from nanomedicines and adequacy of the current guideline on environmental risk assessment. *Environmental Science: Nano* **2018,** *5* (8), 1873-1889.

54.   Stauber, R. H.; Siemer, S.; Becker, S.; Ding, G. B.; Strieth, S.; Knauer, S. K., Small Meets Smaller: Effects of Nanomaterials on Microbial Biology, Pathology, and Ecology. *ACS Nano* **2018,** *12* (7), 6351-6359.

55.   Ribeiro, A. R.; Leite, P. E.; Falagan-Lotsch, P.; Benetti, F.; Micheletti, C.; Budtz, H. C.; Jacobsen, N. R.; Lisboa-Filho, P. N.; Rocha, L. A.; Kühnel, D.; Hristozov, D.; Granjeiro, J. M., Challenges on the toxicological predictions of engineered nanoparticles. *NanoImpact* **2017,** *8*, 59-72.

56.   Lowry, G. V.; Gregory, K. B.; Apte, S. C.; Lead, J. R., Transformations of Nanomaterials in the Environment. *Environ. Sci. Technol.* **2012,** *46*, 6893-6899.

57.   Keller, A. A.; McFerran, S.; Lazareva, A.; Suh, S., Global life cycle releases of engineered nanomaterials. *J Nanopart Res* **2013,** *15*, 1692-1709.

58.   Pettibone, J. M.; Cwiertny, D. M.; Scherer, M.; Grassian, V. H., Adsorption of Organic Acids on TiO2 Nanoparticles: Effects of pH, Nanoparticle Size, and Nanoparticle Aggregation. *Langmuir* **2008,** *24*, 6659-6667.

59.   Gong, W., A real time in situ ATR-FTIR spectroscopic study of linear phosphate adsorption on titania surfaces. *International Journal of Mineral Processing* **2001,** *63*, 147-165.

60.   Ho, T. A.; Greathouse, J. A.; Lee, A. S.; Criscenti, L. J., Enhanced Ion Adsorption on Mineral Nanoparticles. *Langmuir* **2018,** *34*, 5926-5934.

61.   Mensch, A. C.; Hernandez, R. T.; Kuether, J. E.; Torelli, M. D.; Feng, Z. V.; Hamers, R. J.; Pedersen, J. A., Natural Organic Matter Concentration Impacts the Interaction of Functionalized

Diamond Nanoparticles with Model and Actual Bacterial Membranes. *Environ. Sci. Technol.* **2017,** *51* (19), 11075-11084.

62.   Chen, J.; Xiu, Z.; Lowry, G. V.; Alvarez, P. J., Effect of natural organic matter on toxicity and reactivity of nano-scale zero-valent iron. *Water Res* **2011,** *45* (5), 1995-2001.

63.   Rubasinghege, G.; Kyei, P. K.; Scherer, M. M.; Grassian, V. H., Proton-promoted dissolution of a-FeOOH nanorods and microrods: Size dependence, anion effects (carbonate and phosphate), aggregation and surface adsorption. *Journal of Colloid and Interface Science* **2012,** *385*, 15-23.

64.   Levard, C.; Hotze, E. M.; Lowry, G. V.; Brown, G. E., Jr., Environmental transformations of silver nanoparticles: impact on stability and toxicity. *Environ Sci Technol* **2012,** *46* (13), 6900-14.

65.   ADAMO R. PETOSA; DEB P. JAISI; IVAN R. QUEVEDO; MENACHEM ELIMELECH; TUFENKJI, N., Aggregation and Deposition of Engineered Nanomaterials in Aquatic Environments: Role of Physicochemical Interactions. *Environ. Sci. Technol.* **2010,** *44*, 6532–6549.

66.   Fu, L.; Hamzeh, M.; Dodard, S.; Zhao, Y. H.; Sunahara, G. I., Effects of TiO2 nanoparticles on ROS production and growth inhibition using freshwater green algae pre-exposed to UV irradiation. *Environ Toxicol Pharmacol* **2015,** *39* (3), 1074-80.

Chapter 2. Impact of Phosphate Adsorption on Complex Cobalt Oxide Nanoparticle Dispersibility in Aqueous Media.

The following chapter is adapted from the article published in *Environmental Science & Technology*, **2018**, *52*(17),10186-10195 (DOI: 10.1021/acs.est.8b02324), with the co-authors Joseph W. Bennett, Curtis M. Green, Sara E. Mason, Robert J. Hamers.

All of the experiments, data acquisition and analysis, and manuscript preparation and revision were done by Elizabeth D. Laudadio under the advisement of Robert J. Hamers except for the following:

Curtis M. Green collected the transmission electron micrographs in Figure 2.1b and 2.1c. Joseph W. Bennett and Sara E. Mason made intellectual contributions to the analysis of phosphate adsorption, which appears in Section 2.3.3. The ICP-MS data shown in Table 1 was collected by the Wisconsin State Hygiene Laboratory.

2.1 Introduction.

It is widely recognized that the transport, bioavailability, and environmental impact of engineered nanomaterials is largely controlled by the physicochemical properties of the species present at their surfaces.[1] The presence of surface ligands, coatings acquired by interaction with naturally occurring organic materials, and adsorption of ions from solution can play a role by altering surface charge and hydrophilicity and by inducing physical and chemical transformations of the materials.[2-5]

The interaction of small ions with minerals has been extensively studied in the field of geochemistry as a pathway to surface alteration and ultimately the formation of surface transformation products.[6-12] In addition, the capability of metal oxide materials to adsorb ions has

often been intentionally employed for water purification purposes.[13-16] However, the influence of small ions on the properties of engineered nanoparticles has received less attention, as the interaction between engineered materials and the environment is considered secondary to their performance and operational conditions.[17-20] Recent work has shown that the surface transformations of engineered nanomaterials in the environment are at most times unknown: specifically, the chemical changes that influence reactivity, transport, and ultimate fate.[21-25] Among engineered nanomaterials of potential environmental impact, cobalt-based metal oxides are of particular interest.[26-27] Recent studies have shown that cobalt-based oxides interact with high concentrations of phosphate to produce highly effective catalysts[28-30] while lithium intercalation compounds based on $LiCoO_2$ have novel catalytic properties and are widely used as cathode materials for lithium ion batteries.[31-36] The rapid commercialization in the use of $LiCoO_2$ and related oxides such as $Li_xNi_yMn_zCo_{(1-y-z)}O_2$ in nanostructured form for applications such as electric vehicles (amounts of ~40 kg per automobile)[37] has led to increased interest in understanding how small ions may impact the colloidal stability and rate of metal ion release from nanoparticles in this emerging class of complex metal oxides.

Here we report an investigation of the interaction of $LiCoO_2$ with aqueous phosphate ion over a range of concentrations down to micromolar levels, which are commensurate with levels found in natural freshwaters. We characterize the adsorption of phosphate on nanoscale $LiCoO_2$ using in situ attenuated total reflectance-Fourier transform infrared (ATR-FTIR) spectroscopy, X-ray photoelectron spectroscopy, dynamic light scattering, laser doppler microelectrophoresis, and UV−visible spectroscopy. We find that phosphate ion, even at environmentally relevant concentrations of 1 μM,[38-40] adsorbs irreversibly to $LiCoO_2$, significantly altering the surface charge of the nanomaterial and its dispersibility. Though phosphate adsorption renders $LiCoO_2$

more stable in solution, the increased dispersibility does not have an impact on cobalt release from the material. These results suggest that phosphate ions present in natural water systems may significantly enhance the colloidal stability of $LiCoO_2$ and related complex metal oxides materials in the environment.

2.2 Materials and Methods.

2.2.1. Lithium Cobalt Oxide Nanoparticle Synthesis.

We synthesized sheet-like nanoparticles of Li_xCoO_2 as described previously.[41] Briefly, we prepared the $Co(OH)_2$ precursor by dropwise addition of a 1 M $Co(NO_3)_2 \cdot 6H_2O$ to a 0.1 M solution of LiOH ([OH] 5% stoichiometric excess for $Co^{2+} + 2OH^- \rightarrow Co(OH)_2$). The precipitate was isolated by centrifugation (4696 g, 3 min), decanting the supernatant, redispersion of the pellet in water, and centrifuging again; this process was repeated twice more in water. The pellet was then redispersed in methanol and isolated through centrifugation (4696 g, 25 min). We dried the product in a vacuum oven at 30 °C overnight and then at 60 °C for 3 h. To transform the $Co(OH)_2$ particles to Li_xCoO_2, we heated a 10 g mixture of 6:4 molar ratio of $LiNO_3$:LiOH to 200 °C in a poly-(tetrafluoroethylene) container with magnetic stirring, forming a molten salt flux. Once molten, we added 0.20 g of the $Co(OH)_2$ particles to the flux. After 30 min, we quenched the molten flux with water and washed/isolated the precipitate through five cycles of dispersion/isolation via centrifugation in water. The product was then dried in a vacuum oven at 60 °C for 3 h followed by 30 °C overnight.

2.2.2. Crystal Structure Characterization Using X-ray Diffraction (XRD).

We obtained X-ray diffraction patterns of the nanoparticles using a Bruker D8 Advance powder diffractometer with a Cu Kα source and a Lynxeye detector. Powders were adhered to a

zero-diffraction plate (MTI Corp) using vacuum grease and pressed flat. The powder XRD pattern was acquired using a step size of 0.10° and dwell time of 67 s at each point.

2.2.3. Morphology Characterization Using Scanning Electron Microscopy (SEM) and Transmission Electron Microscopy (TEM).

For SEM imaging, $LiCoO_2$ nanosheets were dispersed in methanol and spin-coated onto B-doped Si wafers. Images were acquired using a Leo Supra55 VP SEM, 3 kV electron energy, using a secondary electron detector. The morphology of $LiCoO_2$ nanoparticles was analyzed using a transmission electron microscope (TEM, FEI Tecnai T12) operated at 120 kV. TEM grids were prepared by drop-casting suspensions of $LiCoO_2$ nanoparticles in water onto a carbon supported TEM grid, which was allowed to dry overnight. Images were analyzed using ImageJ software, and the width of the particles was determined based on the average width of 25 particles viewed edge-on.

2.2.4. Quantification of Phosphate Adsorption with X-ray Photoelectron Spectroscopy (XPS).

To quantify the time-dependent adsorption of phosphate onto $LiCoO_2$, we used XPS to measure the P(2p) and Co(2p) intensities. Detailed sample preparation and analysis procedures are reported in the Appendix.

2.2.5. Preparation of $LiCoO_2$ Layers for in situ ATR-FTIR Measurements.

Thin layers of $LiCoO_2$ were prepared by spin-coating $LiCoO_2$ suspensions onto a zinc selenide (ZnSe) trapezoidal prism acting as a 10-bounce internal reflection element (IRE). Samples (2 mL) of 1000 mg/L $LiCoO_2$ in methanol were sonicated for 1 h in a cup ultrasonicator with cooling water (10 s on, 10 s off for 30 min total sonication time). ZnSe IREs were rinsed with ultrapure water and ethanol, dried with N_2 gas, and exposed to UV light from a low-pressure Hg

grid lamp (UV Products) for 10 min. The $LiCoO_2$ solution was then spin-coated onto the clean ZnSe IREs using 25 repeated applications of 75 μL each and spinning for 30 s at 1000 rpm after each application. The layer was then gently cured by heating in a box furnace at 400 °C for 5 min. The ZnSe element was allowed to cool for at least 12 h before using.

2.2.6. ATR-FTIR Studies of Phosphate Adsorption to $LiCoO_2$ Surfaces.

Attenuated total internal reflectance Fourier-transform infrared (ATR-FTIR) spectra were acquired using the previously described $LiCoO_2$-coated ZnSe IREs assembled in a flow cell (Specac) and with a Bruker Vertex 70 FTIR instrument. More detailed measurement information can be found in Appendix 2.

2.2.7. Dynamic Light Scattering Characterization of Nanosheet Diffusion Coefficient and Zeta Potential in Phosphate Solutions.

Dynamic light scattering (DLS) and laser Doppler microelectrophoresis measurements were taken with a Malvern Zetasizer Nano ZS. A 250 mg/L stock solution of $LiCoO_2$ was prepared in 1 mL of ultrapure water and sonicated for 1 h in a cup ultrasonicator with cooling water (10 s on, 10 s off for 30 min total sonication time) before analysis. DLS measurements were performed on 5 mg/L $LiCoO_2$ solutions, prepared by adding an aliquot of the $LiCoO_2$ stock solution to the phosphate/NaCl solutions. Ionic strength was kept constant at 30 mM for all samples through the addition of NaCl, and pH of all samples was controlled as described in the Appendix. After addition of the $LiCoO_2$ (t = 0 h), we immediately measured the nanoparticle diffusion coefficient via DLS and then measured the zeta potential (ZP) by laser Doppler microelectrophoresis. These measurements were repeated after sonication of the nanoparticle solutions for an additional 3.5 h. The results reported are the averages and standard deviations of three sample replicates, with five DLS measurements and three ZP measurements made per sample. The stock $LiCoO_2$ solution was

left sonicating between measurements. The stock solution was imaged following experiments to ensure that sonication was not fracturing the materials (Figure A.2.5).

2.2.8. UV−Visible Absorption Spectroscopy (UV−Vis) Analysis of LiCoO₂ Sedimentation in Phosphate.

A 1000 mg/L stock solution of $LiCoO_2$ was prepared in 2 mL of ultrapure water and sonicated for 30 min in a cup ultrasonicator with cooling water (10 s on, 10 s off for a total of 15 min sonication time) before analysis. We measured the apparent absorbance (Appendix) of 50 mg/L $LiCoO_2$ solutions in three concentrations of phosphate, 1, 10, and 25 mM Na_2HPO_4, compared with ionic strength controls of NaCl at 3, 30, and 75 mM, respectively. The absorbance at 414 and 350 nm was recorded every 6 s for 20 min. Absorbance values at the baseline (350 nm) were subtracted from the absorbance at the $LiCoO_2$ peak (414 nm, which we believe to correspond to the band gap of the material[42-43]) and normalized to t = 0. The decrease in normalized absorbance was tracked as a function of time.

2.2.9. Characterization of Cobalt Release from LiCoO₂ in Model Aqueous Systems.

Moderately hard water (MHW) was prepared by making a 96 mg/L $NaHCO_3$, 60 mg/L $CaSO_4$, 60 mg/L $MgSO_4$, and 4 mg/L KCl solution in ultrapure water. The solution was aerated for 72 h before use and used within 14 days of preparation. The release of cobalt from 0.5 mg/L $LiCoO_2$ or 50 mg/L $LiCoO_2$ into MHW and into MHW containing either 1 or 100 μM Na_2HPO_4 was analyzed using inductively coupled plasma-mass spectrometry (ICP-MS). More detailed information can be found in the Appendix.

2.3 Results and Discussion.

2.3.1. Synthesis and Characterization.

Figure 2.1a shows a representative SEM image of the Li_xCoO_2 particles; corresponding TEM images are shown in Figure 2.1b and 2.1c (an enlarged section of the region indicated in Figure 2.1b) and in Figure A.2.1. SEM and TEM both show that the particles have a sheet-like morphology. Analysis of the TEM images shows that the nanosheets have a diameter of 20−30 nm and a thickness of 5.3 ± 1.7 nm. The TEM image in Figure 2.1c clearly reveals the lattice planes characteristic of the layered Li_xCoO_2 structure. Figure 2.1d shows the powder XRD pattern obtained of these nanomaterials.

We used EVA software for pattern matching; peaks were indexed based on literature patterns of Li_xCoO_2 single crystals indexed to the $R\bar{3}m$ crystal phase.[44] In order to ensure the formation of nanoparticles and not micron-sized particles, our synthesis was performed at relatively low temperature. Consequently, the resulting nanoparticles have lower crystallinity in comparison to bulk particles synthesized by other methods such as hydrothermal,[45] sol−gel,[46] and high-temperature sintering.[47] The (003) peak at $2\theta = 18°$ is associated with the order of stacked layers and is expected to be the highest intensity peak for a fully ordered $R\bar{3}m$ layered material. The truncated intensity of this peak is an indication of some degree of disorder in the material. This disorder may be attributed to the low temperature of the nanoparticle synthesis, the presence of spinel phases, or the lack of full lithiation of the particles. ICP-OES analysis of the ratio of cobalt to lithium in the particles yields a Li:Co ratio of 0.62:1.00. We were not able to confirm if this low ratio of lithium to cobalt comes from the synthesis itself or dissolution of lithium from the lattice during isolation and rinsing of the particles in water. The charge disparity from the lack of

stoichiometric consistency between cobalt and lithium may be compensated through disorder in the materials and potentially incorporation of some other crystalline phases, such as spinel.[48]

Though these materials are imperfectly crystalline, we believe them to be an accurate model for the breakdown materials of modern nanostructured lithium ion battery cathodes that may enter the environment due to improper disposal. Previous studies have shown cathode materials in lithium intercalation batteries can mechanically fracture following electrochemical cycling[49] and that, through repeated deintercalation, restructuring of the material into spinel phases is common.[50-51] For these reasons, our nanoparticles are a good model for the degradation products of lithium ion batteries that may be released into the environment.

2.3.2. ATR-FTIR Studies of Phosphate Adsorption to LiCoO$_2$ Surfaces.

We wanted to understand how phosphate interacted with LiCoO$_2$ surfaces and if these interactions were reversible or not. To assess this, we used in situ ATR-FTIR, a highly sensitive technique for obtaining vibrational spectra at surfaces. By depositing LiCoO$_2$ nanoparticles onto a ZnSe internal reflection element via spin-coating, thin, uniform layers of LiCoO$_2$ can be prepared while maintaining the nanoscale properties of the material (Figure A.2.2). Following deposition, the individual nanoparticles are oriented randomly on the surface and maintain the same primary particle size as they do in solution. For this reason, we believe these LiCoO$_2$ layers are adequate models for how the nanomaterials interact in solution. The assembly of this element into a flow cell allows us to obtain in situ spectra with time-course resolution throughout the duration of the experiment.

Figure 2.2 shows ATR-FTIR spectra from a LiCoO$_2$-coated ZnSe prism after exposure to phosphate (gray traces) and after further rinsing (orange traces) over a wide spectral range (Figure 2.2a) and an expanded view of the P$-$O stretching region near 1050 cm^{-1} (Figure 2.2b). The spectra

exhibit the appearance of a large absorption feature in the spectral region from $\sim$1100 to 900 cm^{-1} where P$-$O stretches are typically observed.[52] Spectra were continuously taken as phosphate was flowed over the surface. These spectra show that under our experimental conditions the P$-$O peak grows in over the course of phosphate exposure, reaching a constant value (absorbance difference between sequential traces <0.0002) after about 60 min of exposure, as shown in Figure A.2.3. This time dependence suggests that the interaction with the LiCoO$_2$ film is complete; the gray traces in Figure 2.2 represent this "saturated" condition.

After the 1 h exposure, we rinsed the films with ultrapure water for an additional hour to remove any excess phosphate from the flow cell that may be contributing to the observed spectrum, yielding the orange "surface" spectra in Figure 2.2. A comparison of the gray and orange traces shows that rinsing leaves the spectrum nearly unchanged, indicating that the phosphate is strongly bound to the surface. Rinsing does produce some small changes in the shape of the peak, as the large peak associated with phosphate-related vibrations is broadened and encompasses multiple peaks. Similar broadening has been reported as evidence of the formation of inner-sphere coordination of citric acid on TiO$_2$ nanoparticles[19] and in molecular orbital theory models of phosphate adsorption onto ferrihydrite.[53]

To gain insight into the nature of phosphate bonding on LiCoO$_2$, we used peak-fitting methods to analyze the phosphate peak and identified five distinct vibrations between 1100 and 900 cm^{-1} as shown in the Figure 2.2c. Four of these peaks, at 1074, 1030, 993, and 930 cm^{-1}, can be assigned to specific vibrational modes by comparing them to the spectrum of phosphate in solution and the associated mode assignments.[52, 54] Prior studies have shown that four peaks in the aqueous spectrum of H$_2$PO$_4^-$ correspond to four P$-$O modes, divided into two sets of doublets.[52, 54] One set of peaks at 1155 and 1075 cm^{-1} is attributed to the asymmetric and symmetric P$-$O

vibrations of the deprotonated P−O groups, and the other set of peaks at 940 and 874 is attributed to the asymmetric and symmetric P−O stretching modes of the P−O−H asymmetric and symmetric vibrational stretches.[52, 54] The existence of four major features in our phosphate adsorbed spectrum suggests that phosphate on the surface of $LiCoO_2$ has the same symmetry (C_{2v}) and therefore the same infrared active vibrational modes as $H_2PO_4^-$. For phosphate bound to $LiCoO_2$, we attribute the two higher frequency features at 1074 and 1030 cm^{-1} to the symmetric and asymmetric CoO_2−PO_2 vibrations. This doublet is expected to occur at lower frequency than the $(HO)_2PO_2^-$ doublet in aqueous $H_2PO_4^-$ since the P−O bond when bound to a metal is weaker than in the free molecule, as observed previously for phosphate on goethite,[52] TiO_2,[54] and ferrihydrite.[53]

In our spectrum the two lower frequency features at 993 and 930 cm^{-1} correspond to the symmetric and asymmetric CoO−P vibrations. The CoO−P doublet occurs at higher wavenumbers than the CoO−H doublet, as the P−O bond in CoO−P is stronger than that in HO−P, as observed previously for phosphate on goethite,[52] TiO_2,[54] and ferrihydrite.[53] These prior studies of phosphate adsorption on goethite,[52] ferrihydrite.[53] and TiO_2[54] correlate these vibrational modes with a deprotonated, inner-sphere, bidentate complex on the surface. Previous studies of phosphate adsorption to titanium dioxide also report a peak present at 1008 cm^{-1} and have attributed it to an orthophosphate (PO_4^{3-}) molecule with Td symmetry electrostatically bound to the surface.[54] While the P−O region is quite complex, our peak-fitting analysis (Figure 2.2c) does not indicate the presence of a peak at 1008 cm^{-1}. The absence of this feature in our spectra suggests that adsorption on $LiCoO_2$ is predominantly inner sphere deprotonated bidentate, though we cannot rule out the possibility of some outer sphere, electrostatically bound $H_2PO_4^-$ species. In addition to the four peaks attributed to the deprotonated bidentate structure of phosphate on the metal oxide surface, the P−O stretching region encompasses a smaller feature at 1141 cm^{-1} which may represent a

P−O−H bending mode, indicating that some of the phosphate at the surface may be protonated.[55] Figure 2.3 depicts a combined view of the potential binding that can be inferred from the FTIR spectra: deprotonated bidentate (Figure 2.3a), outer sphere adsorption of diprotonated $H_2PO_4^-$ (Figure 2.3b), and monoprotonated bidentate (Figure 2.3c).

ATR-FTIR studies confirm that phosphate interacts strongly and irreversibly with $LiCoO_2$ surfaces. The deconvolution of the spectrum elucidates specific vibrational modes consistent with the formation of a deprotonated, bidentate inner sphere complex on the $LiCoO_2$ particles. It is expected that such a coordination would have an impact on the surface charge of these nanoparticles, which we investigated through DLS and ZP measurements.

2.3.3. Phosphate Adsorption Quantification with X-ray Photoelectron Spectroscopy (XPS).

We then wanted to understand to what extent phosphate was able to coat the surface of $LiCoO_2$ nanoparticles. To study this, we employed XPS, a surface-sensitive and element-specific spectroscopic technique, to quantify the amount of phosphorus relative to cobalt on the surface of $LiCoO_2$ nanoparticles exposed to phosphate in solution for varying amounts of time. $LiCoO_2$ was exposed to phosphate in solution at a ratio of 1 mg $LiCoO_2$:0.1 mmol Na_2HPO_4 (pH 7.3). Aliquots were removed at specific time intervals and analyzed with XPS. Figure 2.4b and 2.4c show representative X-ray photoelectron spectra for the Co(2p) and P(2p) regions.

Applying Equation 1 (Appendix) to the calculated peak areas of the Co(2p) and P(2p) peaks for each time point allows for the calculation of the phosphate coverage in atoms/nm^2, as shown in Figure 2.4a. Stable coverages around 2 atoms/nm^2 are observed over a time scale of 24−72 h. This value decreases to 1.2 atoms/nm^2 by 172 h, which is potentially due to a pH change over time as a consequence of $LiCoO_2$ dissolution; dissolution of lithium intercalation nanomaterials has been described previously.[56-58] Previous studies of phosphate sorption by hematite and goethite

have reported maximum surface adsorption values of 2.51 μmol/m^2, or 1.5 atoms of phosphorus/nm^2, which is comparable to the values we report here.[59-60]

Upon introduction of LiCoO$_2$, the pH of 1 mM Na$_2$HPO$_4$ solutions was elevated from 7.3 to 7.8. Previous DFT studies on LiCoO$_2$ demonstrated that dissolution of surface Li is thermodynamically favored in aqueous environments and that there is a concurrent surface exchange of Li$^+$ and H$^+$ from surrounding water to produce an H-terminated LiCoO$_2$ surface.[61] If the H$^+$ is removed from water, then it most likely leaves behind OH$^-$. The net result of the surface transformation would be an H-terminated LiCoO$_2$ surface and both Li$^+$ cations and OH$^-$ anions in solution, effectively increasing the pH.[61-62]

The increase in pH also means that the concentration of HPO$_4^{2-}$ will increase relative to the concentration of H$_2$PO$_4^-$ in solution. Both species have the capability to bind to the surface, but they are able to bind through different coordination. HPO$_4^{2-}$ can bind in a monodentate coordination, resulting in the loss of one water molecule, whereas H$_2$PO$_4^-$ can bind bidentate, resulting in the loss of two water molecules. The entropy increase for bidentate adsorption is larger than for the monodentate, resulting in an increase in adsorption energy, and so it is expected to be favorable over monodentate adsorption.[61] Both adsorption processes are expected to occur through the Eigen−Wilkins mechanism of adsorption, where phosphate binds first in an outer-sphere coordination before inner sphere.[63-64] This has been shown computationally for phosphate adsorption onto LiCoO$_2$ previously.[61]

The effect of initial phosphate concentration on phosphate coverage on LiCoO$_2$ surfaces was also explored. Three equivalents of LiCoO$_2$ nanoparticles were suspended and stirred in each of 1, 10, and 100 mM Na$_2$HPO$_4$ for 1 h, isolated, rinsed, dried, and analyzed via XPS. The results in Figure A.2.4 show that over short time scales, coverage values achieved for each concentration

are comparable, at approximately 2 atoms/nm^2. This further suggests that the adsorption process is not kinetically limited and that long-term changes to phosphate coverage on LiCoO$_2$ may be the result of pH changes and/or dissolution processes.

2.3.4. Dynamic Light Scattering Characterization of Nanosheet Size and Zeta Potential in Phosphate.

Our ATR-FTIR spectroscopy results were consistent with the formation of a deprotonated, bidentate inner-sphere phosphate complex on the surface of our LiCoO$_2$ nanoparticles. Considering this coordination on the surface, we would expect that phosphate adsorption would decrease the surface charge of LiCoO$_2$ nanoparticles in solution. If the surface charge was significantly altered, phosphate adsorption would allow for electrostatic stabilization of LiCoO$_2$ nanoparticles in solution, which would be evidenced by decreased aggregation in comparison to particles in the absence of phosphate.

To probe these hypotheses, we employed DLS to study the impact of phosphate concentration on the size and diffusion coefficient of LiCoO$_2$ nanoparticles and ZP measurements to see how the zeta potential of LiCoO$_2$ nanoparticles in solutions changed with increasing phosphate concentration. Zeta potential in polar/ionic solvent is traditionally calculated from the electrophoretic mobility of the particles using the Smoluchowski model, which is derived for spherical particles. The Smoluchowski model includes a value of the Henry function (F($\kappa\alpha$)) of 3/2, which assumes that the Debye length (1/κ) is much larger than the size of the particle. However, this is not necessarily true for nanoparticles.[65] We estimate our typical nanoparticle thickness to be 5 nm from edge-on TEM micrographs (Figure 2.1b, c). Particles in a 1 mM salt concentration have a Debye length of approximately 10 nm, yielding a $\kappa\alpha$ of 0.5 nm, and a value for F($\kappa\alpha$) of 1.[66] Because ZP is inversely proportional to F($\kappa\alpha$), we expect the overestimation of

F(κα) by the Smoluchowski model to yield underestimated values of ZP magnitude in the data reported here. Additionally, because our particles are non-spherical and therefore do not have a single radius, the application of the Henry function is not straightforward. For this reason, interpretation of our zeta potential measurements focuses on the observed trends rather than absolute values.

Sonication of the stock $LiCoO_2$ solution during the duration of the experiment allows for complete dispersion of the nanoparticles in the aqueous matrix, ensuring that the starting nanoparticle dispersibility between the initial measurements and later time point measurements is the same. SEM images of the $LiCoO_2$ solution following this amount of sonication show that the primary particle size is not impacted as evidenced in Figure A.2.5. Figure 2.5 compares DLS measurements and ZP measurements for $LiCoO_2$ in phosphate both measured immediately after introduction of $LiCoO_2$ to the phosphate solution ($t = 0$ h; open blue circles) and also after allowing the sample to sonicate for a few hours ($t = 3.5$ h; filled red circles). Since larger particles move more slowly than smaller particles,[67-68] we expect that more highly aggregated $LiCoO_2$ particles will have smaller diffusion coefficients, and more dispersed $LiCoO_2$ particles will have larger diffusion coefficients. Figure 2.5a shows that the diffusion coefficients of $LiCoO_2$ in all concentrations of phosphate studied were similar at $t = 0$ h but decreased in low concentrations of phosphate after 3.5 h. At the highest two concentrations of phosphate, 10^{-3} and 10^{-2} M, an increase in diffusion coefficient is observed after 3.5 h, consistent with the hypothesis that $LiCoO_2$ nanomaterials in high concentrations of phosphate may form more stable colloidal suspensions than in either pure water or in NaCl solutions.

A comparison of the zeta potential of $LiCoO_2$ in phosphate solutions provides insight into the observations described above. Figure 2.5b shows that the zeta potential of $LiCoO_2$ decreases

with increasing phosphate concentration. At phosphate concentrations of 10^{-4} M and larger, zeta potentials are negative with magnitudes of 30 mV or more, which is in the range of values generally accepted to represent stable colloidal suspensions.[67, 69] At these phosphate concentrations, the zeta potentials of $LiCoO_2$ are large enough to stabilize the particles through electrostatic repulsion. Consequently, the particles do not aggregate as significantly over time in high concentrations of phosphate than without phosphate present, consistent with the diffusion coefficient data presented in Figure 2.5a.

The trends described from Figure 2.5a and 2.5b are observed at lower concentrations of phosphate; however, analysis of these samples was at our instrumental limits, and so the data are not shown here. Nevertheless, the data shown span a range of phosphate concentrations that are relevant to freshwater sources. The concentration of dissolved phosphate in lakes varies within the sub-micromolar to micromolar range, while in polluted rivers the concentration can be elevated to tens or hundreds of micromolar.[40, 70]

2.3.5. UV−Vis Tracking of $LiCoO_2$ Sedimentation in Phosphate.

To further probe the impact of phosphate adsorption on $LiCoO_2$ dispersibility in solution, we employed UV−visible spectroscopy. We tracked the apparent UV−vis absorbance (i.e., the total extinction, determined by the sum of true absorption and optical scattering) of $LiCoO_2$ in three concentrations of phosphate, 1, 10, and 25 mM Na_2HPO_4, with corresponding ionic strength controls of 3, 30, and 75 mM NaCl, respectively, yielding the data in Figure 2.6. The spectrum in Figure 2.6a shows the $LiCoO_2$ peak at 414 nm, from which we subtracted the absorbance at baseline (350 nm), normalized to t = 0, and tracked the decay over 20 min. Figure 2.6b shows the final absorbance values as a function of phosphate concentration with respect to the NaCl ionic strength controls.

Figure A.2.6 shows that for both $LiCoO_2$ in phosphate and NaCl, an initial drop in absorbance occurs at early time points, followed by stabilization of the absorbance over the 20 min time frame. This early decay in absorbance followed by stabilization over longer time scales is similar to that reported in previous studies for low concentrations (7 mg/L) of magnetic iron nanoparticle suspensions in water[71] and high concentrations (100 mg/L) of ZnO nanoparticles with natural organic matter at different ionic strengths.[72] We found that the absorbance of $LiCoO_2$ in phosphate decayed less significantly than the ionic strength control at all phosphate concentrations, consistent with our hypothesis that particles in the presence of phosphate are stabilized in suspension. The change in absorbance at all concentrations of phosphate is similar, meaning that the stabilizing impact of phosphate on $LiCoO_2$ is observed across all concentrations studied. This result is consistent with the particles being comparably coated with phosphate at each concentration, in agreement with the phosphate coverage on $LiCoO_2$ measured via XPS. For example, for these experiments, at 1 mM Na_2HPO_4 there are approximately 3.6×10^{18} phosphate molecules present in solution, while only 2.6×10^{16} phosphate molecules are required to achieve the ~2 atoms P/nm^2 coverage values obtained from the XPS experiments at this concentration of $LiCoO_2$. Therefore, at each phosphate concentration studied here, there is at least a 100-fold excess of phosphate compared to the amount required to achieve the coverages observed via XPS. Additionally, each concentration presented here is comparable to or larger than the highest concentrations studied in the ZP measurements, which show that at phosphate concentrations 1 mM and higher, the ZP becomes increasingly more negative, with a magnitude larger than the value of ~30 mV typically associated with stable colloidal suspensions. For the ionic strength control experiments, we observed a more significant decay in absorbance over time with increasing concentration of a noninteracting ion source (NaCl). This is consistent with DLVO theory, which

predicts that colloidal stability decreases as ionic strength increases. The difference in $LiCoO_2$ stability in phosphate solution compared with NaCl at the same ionic strength shows that the enhanced stability in the presence of phosphate is not due to an ionic strength effect but is due to a specific chemical interaction between phosphate and $LiCoO_2$ that increases particle stability.

2.3.6. Dissolution of $LiCoO_2$ in Model Aqueous Environments.

Previous studies have shown that metal release from complex metal oxide nanomaterials can have an adverse impact on organisms.[56-58] We studied the dissolution of 0.5 mg/L $LiCoO_2$ in moderately hard water (MHW) and MHW + 1 μM Na_2HPO_4 as a model for a freshwater environment to discern if phosphate had a significant impact on cobalt release from $LiCoO_2$. We also studied the dissolution of 50 mg/L $LiCoO_2$ in MHW and MHW + 100 μM Na_2HPO_4 to discern if concentration played a significant role in the differences between cobalt release with and without phosphate. Table 2.1 shows that the presence of phosphate did not significantly impact the dissolution of $LiCoO_2$ at either low or high concentrations of $LiCoO_2$ and phosphate as compared to the dissolution without phosphate present. While phosphate adsorption increases the dispersibility of $LiCoO_2$ and therefore more surface area of $LiCoO_2$ is exposed to solution, we do not observe a corresponding increase in cobalt release. This is potentially due to the phosphate adsorbed on the surface mitigating dissolution by preventing the release of Co from the material, which has been reported previously.[10, 73] This is supported by prior studies on the dissolution of $LiCoO_2$-type materials in aqueous media, where it was shown that surface transition metal dissolution of Co is most likely mediated by OH^-.[62]

2.4 Environmental Impact.

This work is important to long-term understanding of the potential environmental impact of lithium-ion battery materials. The ubiquitous use of $LiCoO_2$ and related Co-based lithium

intercalation compounds in mobile electronics (e.g., laptops, cell phones, electric vehicles) is expected to lead to dramatic increases in production and use during the next decade; these increases are driven largely by increased worldwide demand for electric vehicles.[36] However, there is currently little worldwide infrastructure for recycling of lithium ion batteries.[36, 74-75] As a result, LIBs are an increasingly important component of electronic waste ("E-waste"), much of which is disposed of in developing countries that have less restrictive waste management practices.[36, 74-78] Our work is relevant to understanding the interaction of lithium-ion battery cathodes when exposed to environmental conditions, such as those that might arise from improper disposal or other uncontained release. Our work shows that the interaction of $LiCoO_2$ nanomaterials with phosphate ion at environmentally relevant concentrations irreversibly alters the $LiCoO_2$ surface charge and therefore dispersibility in aqueous media. This result has environmental impact because the irreversible adsorption of phosphate at environmentally relevant concentrations suggests that phosphate may play a significant role in the transport of $LiCoO_2$ and related materials in soil and into freshwater environments and may therefore be important in understanding the transport and subsequent biological impact of $LiCoO_2$ and related compounds.

2.5 Figures.
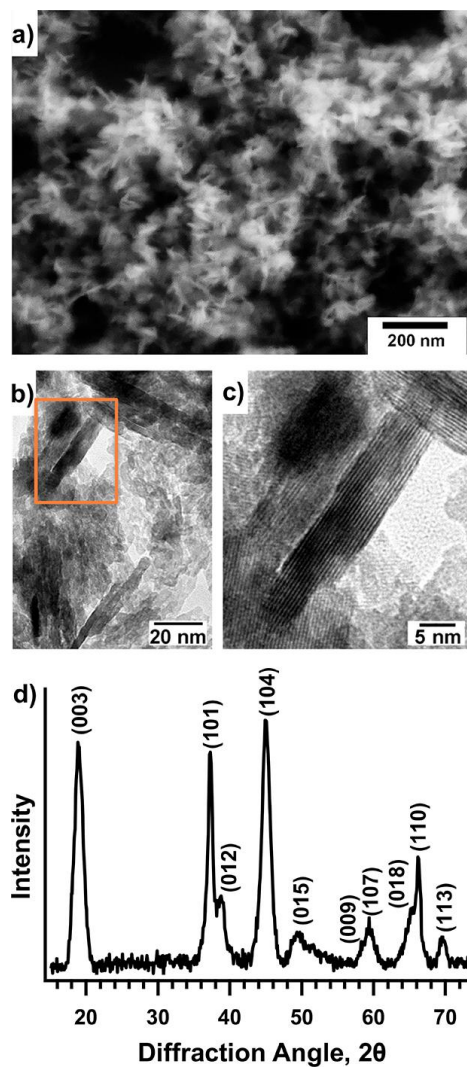
Figure 2.1. Characterization of Li_xCoO_2 nanosheets: (a) SEM micrograph; (b) TEM micrograph; (c) enlarged version of the region highlighted in (b) revealing edge-on lattice planes of Li_xCoO_2 sheet; (d) powder X-ray diffraction pattern.
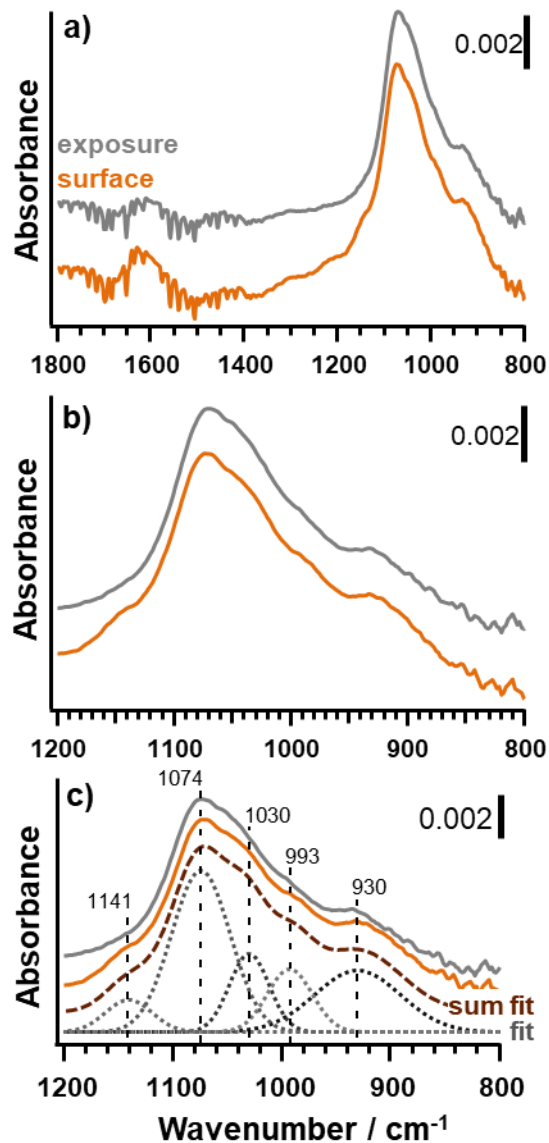
Figure 2.2. (a) ATR-FTIR spectrum of phosphate on $LiCoO_2$ (gray trace) after exposure and (orange trace) after rinsing with water. (b) Zoom of P−O stretching region from top spectrum. (c) Multipeak fit of middle spectrum.
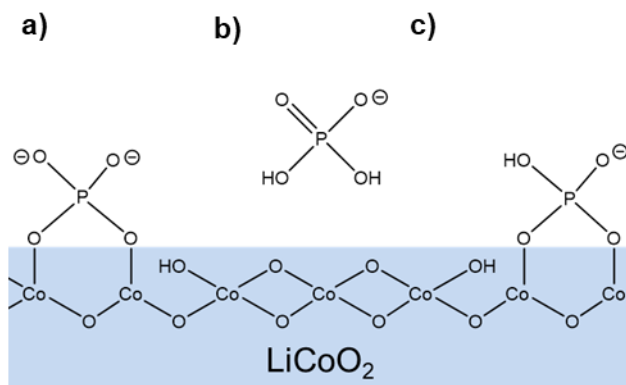
Figure 2.3. Potential binding configurations supported by the ATR-FTIR spectra of phosphate on the surface of LiCoO$_2$: (a) inner sphere deprotonated bidentate, (b) outer sphere diprotonated, and (c) inner sphere mono-protonated bidentate.
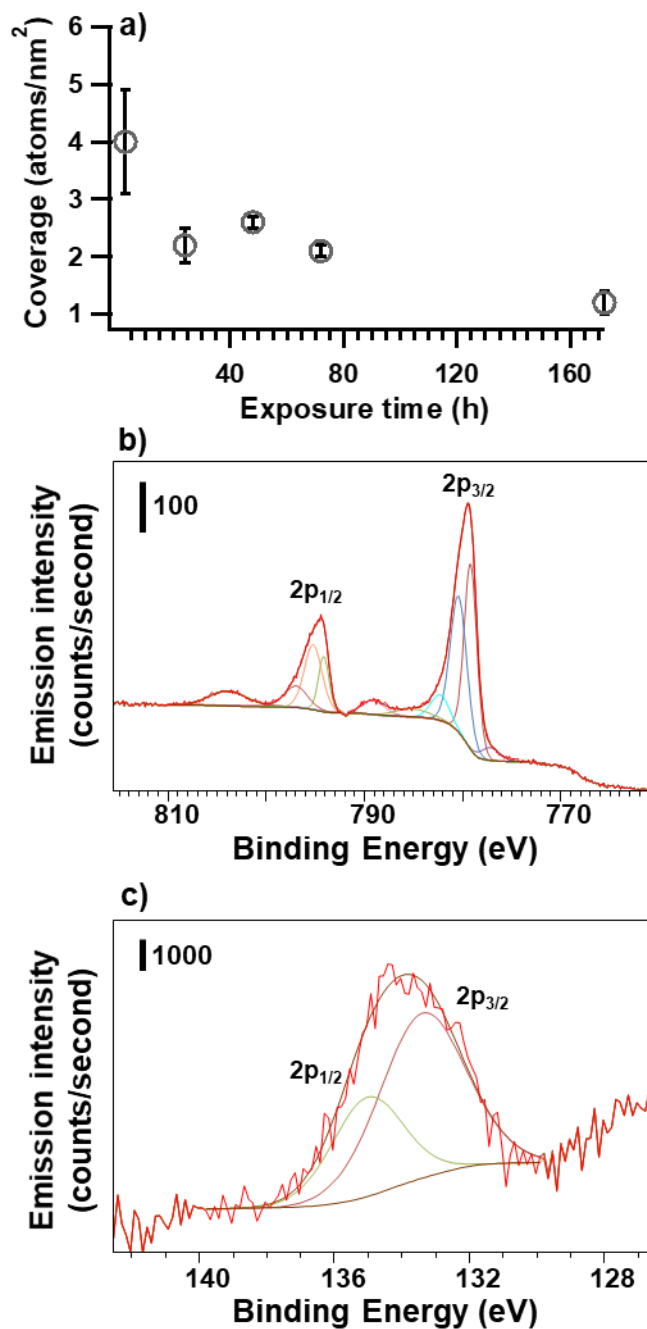
Figure 2.4. (a) Atomic coverage of phosphorus on LiCoO$_2$ nanoparticles following exposure as calculated from XPS. (b) Representative Co(2p) X-ray photoelectron spectrum. (c) Representative P(2p) Xray photoelectron spectrum.
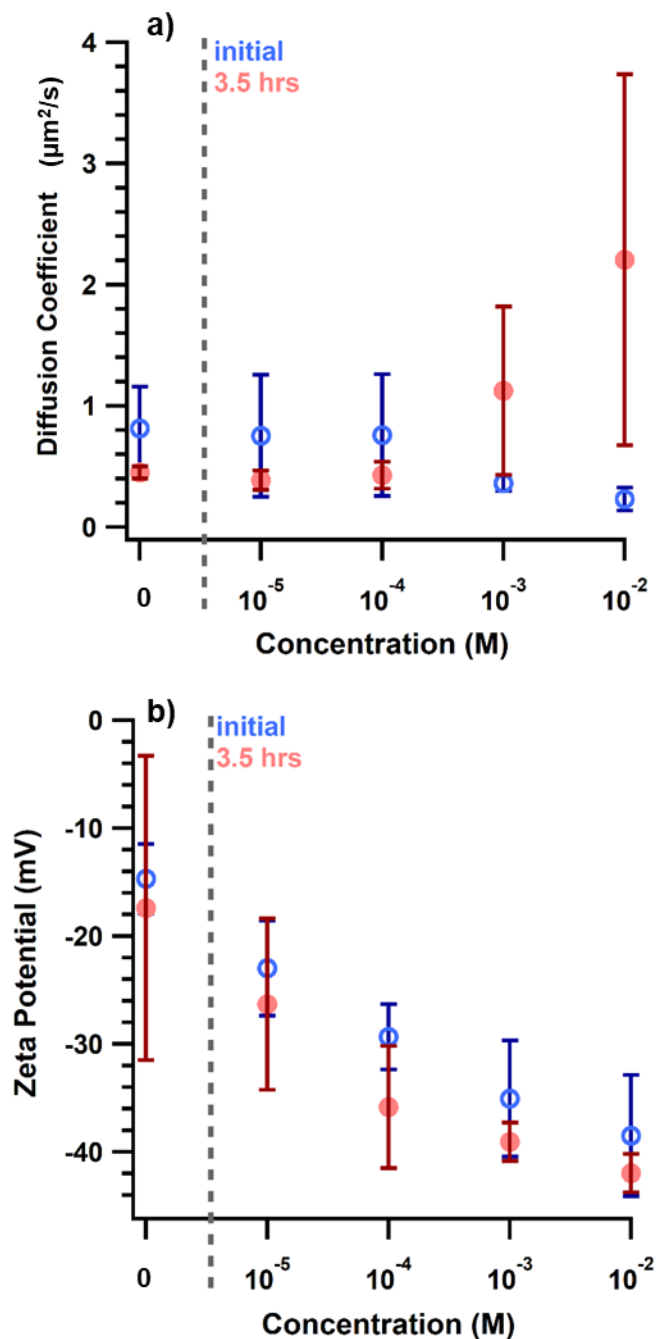
Figure 2.5. (a) Diffusion coefficient of LiCoO$_2$ in phosphate vs concentration of phosphate. (b)

Zeta potential of LiCoO$_2$ in phosphate vs concentration of phosphate. Open blue circles represent

measurements taken immediately after the addition of LiCoO$_2$ to phosphate. Filled red circles

represent measurements taken after 3.5 h sonication of the LiCoO$_2$ in phosphate. The dashed line

indicates a break in the scale after the 0 M Na_2HPO_4 (ionic strength control, 30 mM NaCl) data point.
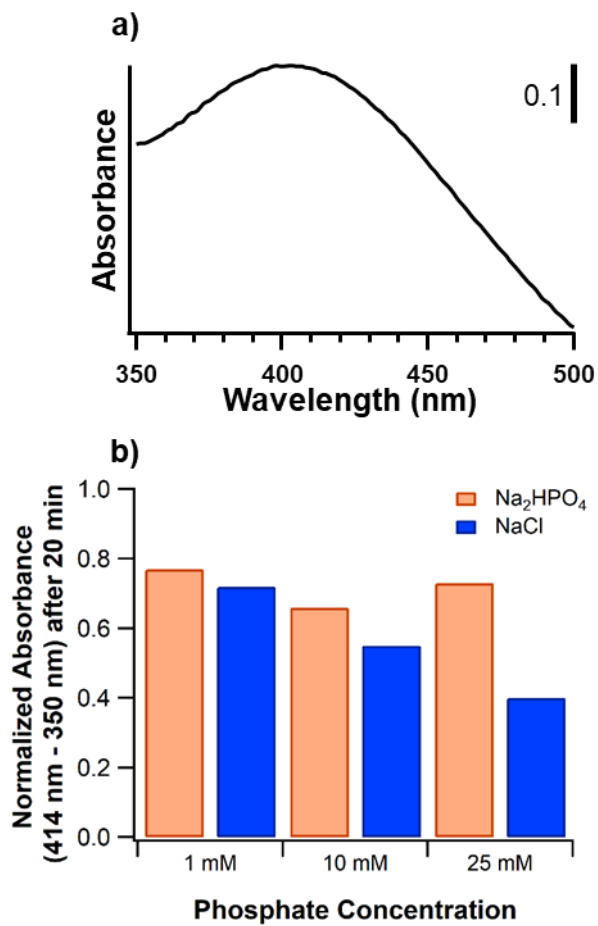
Figure 2.6. (a) Representative normalized absorbance spectrum for $LiCoO_2$ in suspension. Scale bar represents absorbance of 0.25. (b) Normalized peak absorbance of $LiCoO_2$ after 20 min in solution as a function of phosphate concentration (orange bars), compared to the NaCl ionic strength control (blue bars).

	Co released in MHW (ppb)	Co released in MHW + Na$_2$HPO4 (ppb)
0.5 mg/L LiCoO$_2$ 1 μM Na$_2$HPO$_4$	7.3 ± 9.0	6.9 ± 5.7
50 mg/L LiCoO$_2$ 100 μM Na$_2$HPO$_4$	64.8 ± 14.6	70.0 ± 3.8

Table 2.1. Co Released into MHW, MHW with Phosphate Present at Two Concentrations of LiCoO$_2$ and Phosphate.

2.6 References.

1.   Grassian, V. H.; Haes, A. J.; Mudunkotuwa, I. A.; Demokritou, P.; Kane, A. B.; Murphy, C. J.; Hutchison, J. E.; Isaacs, J. A.; Jun, Y.-S.; Karn, B.; Khondaker, S. I.; Larsen, S. C.; Lau, B. L. T.; Pettibone, J. M.; Sadik, O. A.; Saleh, N. B.; Teague, C., NanoEHS – defining fundamental science needs: no easy feat when the simple itself is complex. *Environ. Sci.: Nano* **2016,** *3*, 15-27.

2.   Petosa, A. R.; Jaisi, D. P.; Quevedo, I. R.; Elimelech, M.; Tufenkji, N., Aggregation and Deposition of Engineered Nanomaterials in Aquatic Environments: Role of Physicochemical Interactions. *Environ. Sci. Technol.* **2010,** *44*, 6532-6549.

3.   Levard, C.; Hotze, E. M.; Lowry, G. V.; Gordon E. Brown, J., Environmental Transformations of Silver Nanoparticles: Impact on Stability and Toxicity. *Environ. Sci. Technol.* **2012,** *46*, 6900-6914.

4.   Lowry, G. V.; Gregory, K. B.; Apte, S. C.; Lead, J. R., Transformations of Nanomaterials in the Environment. *Environ. Sci. Technol.* **2012,** *46*, 6893-6899.

5.   Rathnayake, S.; Unrine, J. M.; Judy, J.; Miller, A.-F.; Rao, W.; Bertsch, P. M., Multitechnique Investigation of the pH Dependence of Phosphate Induced Transformations of ZnO Nanoparticles. *Environ. Sci. Technol.* **2014,** *48*, 4757-4764.

6.   Ler, A.; Stanforth, R., Evidence for Surface Precipitation of Phosphate on Goethite. *Environ Sci Technol* **2003,** *37* (2694-2700).

7.   Chen, Y.; Butler, J. N.; Stumm, W., Kinetic Study of Phosphate Reaction with Aluminum Oxide and Kaolinite. *Environ Sci Technol* **1973,** *7* (4), 327-332.

8.   Huang, C.-P.; Stumm, W., Specific Adsorption of Cations on Hydrous Al2O3. *Journal of Colloid and Interface Science* **1972,** *43* (2), 409-420.

9.   Borggaard, O. K., The influence of iron oxides on phosphate adsorption by soil. *Journal of Soil Science* **1983,** *34*, 333-341.

10.   Stumm, W.; Wollast, R., COORDINATION CHEMISTRY OF WEATHERING: Kinetics of the Surface-Controlled Dissolution of Oxide Minerals. *Reviews of Geophysics* **1990,** *28* (1), 53-59.

11.   Appel, C.; Rhue, D.; Kabengi, N.; Harris, W., Calorimetric Investigation of the Nature of Sulfate and Phosphate Sorption on Amorphous Aluminum Hydroxide. *Soil Science* **2013,** *178* (4), 180-188.

12.   Sabur, M. A.; Goldberg, S.; Gale, A.; Kabengi, N.; Al-Abadleh, H. A., Temperature-Dependent Infrared and Calorimetric Studies on Arsenicals Adsorption from Solution to Hematite Nanoparticles. *Langmuir* **2015,** *31*, 2749-2860.

13.   Li, M.; Liu, J.; Xu, Y.; Qian, G., Phosphate adsorption on metal oxides and metal hydroxides: A comparative review. *Environ. Rev.* **2016,** *24*, 319-332.

14.   Penke, Y. K.; Anantharaman, G.; Ramkumar, J.; K.K., K., Aluminum Substituted Cobalt Ferrite (Co−Al−Fe) Nano adsorbent for arsenic adsorption in aqueous Systems and detailed redox behavior study with XPS. *ACS Appl. Mater. Interfaces* **2017,** *9*, 11587-11598.

15.   Zhao, D.; Joo, S. H., Environmental dynamics of metal oxide nanoparticles in heterogeneous systems: A review. *J. Hazard. Mater.* **2017,** *322*, 29-47.

16.   Amde, M.; Liu, J.; Tan, Z.; Bekana, D., Transformation and bioavailability of metal oxide nanoparticles in aquatic and terrestrial environments. *Environ. Pollut.* **2017,** *230*, 250-267.

17.   Bian, S.-W.; Mudunkotuwa, I. A.; Rupasinghe, T.; Grassian, V. H., Aggregation and Dissolution of 4 nm ZnO Nanoparticles in Aqueous Environments: Influence of pH, Ionic Strength, Size, and Adsorption of Humic Acid. *Langmuir* **2011,** *27*, 6059-6068.

18.   Mudunkotuwa, I. A.; Grassian, V. H., Histidine adsorption on TiO2 nanoparticles: an integrated spectroscopic, thermodynamic, and molecular-based approach toward understanding nano-bio interactions. *Langmuir* **2014,** *30* (29), 8751-60.

19.   Mudunkotuwa, I. A.; Grassian, V. H., Citric Acid Adsorption on TiO2 Nanoparticles in Aqueous Suspensions at Acidic and Circumneutral pH- Surface Coverage, Surface Speciation, and Its Impact on Nanoparticle-Nanoparticle Interactions. *Journal of the American Chemical Society* **2010,** *132*, 14986-14994.

20.   Pettibone, J. M.; Cwiertny, D. M.; Scherer, M.; Grassian, V. H., Adsorption of Organic Acids on TiO2 Nanoparticles: Effects of pH, Nanoparticle Size, and Nanoparticle Aggregation. *Langmuir* **2008,** *24*, 6659-6667.

21.   He, X.; Aker, W. G.; Fu, P. P.; Hwang, H.-M., Toxicity of engineered metal oxide nanomaterials mediated by nano–bio–eco–interactions: a review and perspective. *Environ. Sci.: Nano* **2015,** *2*, 564-582.

22.   Ribeiro, A. R.; Leite, P. E.; Falagan-Lotsch, P.; Benetti, F.; Micheletti, C.; Budtz, H. C.; Jacobsen, N. R.; Lisboa-Filho, P. N.; Rocha, L. A.; Kuhnel, D.; Hristozov, D.; Granjeiro, J. M., Challenges on the toxicological predictions of engineered nanoparticles. *NanoImpact* **2017,** *8*, 59-72.

23.   Nowack, B.; Ranville, J. F.; Diamond, S.; Gallego-Urrea, J. A.; Metcalfe, C.; Rose, J.; Horne, N.; Koelmans, A. A.; Klaine, S. J., POTENTIAL SCENARIOS FOR NANOMATERIAL RELEASE AND SUBSEQUEN TALTERATIO N IN THE ENVIRONMENT. *Environmental Toxicology and Chemistry* **2012,** *31* (1), 50-59.

24.   Farre, M.; Sanchis, J.; Barcelo, D., Analysis and assessment of the occurrence, the fate and the behavior of nanomaterials in the environment. *Trends in Analytical Chemistry* **2011,** *30* (3), 517-527.

25.   Keller, A. A.; McFerran, S.; Lazareva, A.; Suh, S., Global life cycle releases of engineered nanomaterials. *J Nanopart Res* **2013,** *15*.

26.   Dunn, J. B.; Gaines, L.; Kelly, J. C.; James, C.; Gallagher, K. G., The significance of Li-ion batteries in electric vehicle life-cycle energy and emissions and recycling's role in its reduction. *Energy Environ. Sci.* **2015,** *8* (1), 158-168.

27.   Ellingsen, L. A.; Hung, C. R.; Majeau-Bettez, G.; Singh, B.; Chen, Z.; Whittingham, M. S.; Stromman, A. H., Nanotechnology for environmentally sustainable electromobility. *Nat Nanotechnol* **2016,** *11* (12), 1039-1051.

28.   Zhong, D. K.; Cornuz, M.; Sivula, K.; Gratzel, M.; Gamelin, D. R., Photo-assisted electrodeposition of cobalt–phosphate (Co–Pi) catalyst on hematite photoanodes for solar water oxidation. *Energy Environ. Sci.* **2011,** *4*, 1759-1764.

29.   Kanan, M. W.; Surendranath, Y.; Nocera, D. G., Cobalt–phosphate oxygen-evolving compound. *Chemical Society Reviews* **2009,** *38*, 109-114.

30.   Lu, Z. Y.; Wang, H. T.; Kong, D. S.; Yan, K.; Hsu, P. C.; Zheng, G. Y.; Yao, H. B.; Liang, Z.; Sun, X. M.; Cui, Y., Electrochemical tuning of layered lithium transition metal oxides for improvement of oxygen evolution reaction. *Nat. Commun.* **2014,** *5*, 7.

31.   Whittingham, M. S., Lithium Batteries and Cathode Materials. *Chem. Rev.* **2004,** *104*, 4271-4301.

32.   Ruffo, R.; Wessells, C.; Huggins, R. A.; Cui, Y., Electrochemical behavior of LiCoO2 as aqueous lithium-ion battery electrodes. *Electrochem. Commun.* **2009,** *11* (2), 247-249.

33.   Tang, W.; Zhu, Y. S.; Hou, Y. Y.; Liu, L. L.; Wu, Y. P.; Loh, K. P.; Zhang, H. P.; Zhu, K., Aqueous rechargeable lithium batteries as an energy storage system of superfast charging. *Energy & Environmental Science* **2013,** *6* (7), 2093-2104.

34.   Tang, W.; Liu, L. L.; Tian, S.; Li, L.; Yue, Y. B.; Wu, Y. P.; Guan, S. Y.; Zhu, K., Nano-LiCoO2 as cathode material of large capacity and high rate capability for aqueous rechargeable lithium batteries. *Electrochem. Commun.* **2010,** *12* (11), 1524-1526.

35.   Li, L.; Bian, Y. F.; Zhang, X. X.; Guan, Y. B.; Fan, E. S.; Wu, F.; Chen, R. J., Process for recycling mixed-cathode materials from spent lithium-ion batteries and kinetics of leaching. *Waste Manage.* **2018,** *71*, 362-371.

36.   Richa, K.; Babbitt, C. W.; Gaustad, G.; Wang, X., A future perspective on lithium-ion battery waste flows from electric vehicles. *Resour. Conserv. Recycl.* **2014,** *83*, 63-76.

37.   Notter, D. A.; Gauch, M.; R., W.; Wagner, P.; Stamp, A.; Zah, R.; Althaus, H.-J., Contribution of Li-Ion Batteries to the Environmental Impact of Electric Vehicles. *Environ Sci Technol* **2010,** *44*, 6550-6556.

38.   Hudson, J. J.; Taylor, W. D.; Schindler, D. W., Phosphate concentrations in lakes. *Nature* **2000,** *406*, 54-56.

39.   Halmann, M.; Stiller, M., Turnover and uptake of dissolved phosphate in freshwater. *Limnology and Oceanography* **1974,** *19* (5), 774-783.

40.   Froelich, P. N., Kinetic control of dissolved phosphate in natural rivers and estuaries: A primer on the phosphate buffer mechanism. *Limnology and Oceanography* **1988,** *33* (4), 649-668.

41.   Chen, H.; Grey, C. P., Molten Salt Synthesis and High Rate Performance of the ''Desert-Rose'' form of LiCoO2**. *Advanced Materials* **2008,** *20*, 2206-2210.

42.   Wei, G.; Haas, T. E.; Goldner, R. B., Thin films of lithium cobalt oxide. *Solid State Ionics* **1992,** *58*, 115-122.

43.   van Elp, J.; Wieland, J. L.; Eskes, H.; Kuiper, P.; Sawatzky, G. A.; de Groot, F. M. F.; Turner, T. S., Electronic structure of CoO, Li-doped CoO, and LiCoO2. *Physical Review B* **1991,** *44* (12), 6090-6103.

44.   Ou-Yang, T. Y.; Huang, F.-T.; Shu, G. J.; Lee, W. L.; Chu, M.-W.; Liu, H. L.; Chou, F. C., Electronic phase diagram of LixCoO2 revisted with potentiostatically deintercalated single crystals. *Physical Review B* **2012,** *85* (035120-1), 1-8.

45.   Okubo, M.; Hosono, E.; Kim, J.; Enomoto, M.; Kojima, N.; Kudo, T.; Zhou, H.; Honma, I., Nanosize Effect on High-Rate Li-Ion Intercalation in LiCoO2 Electrode. *Journal of the American Chemical Society* **2007,** *129*, 7444-7452.

46.   Sun, Y.-K.; Oh, I.-H.; Hong, S.-A., Synthesis of ultrafine LiCo02 powders by the sol-gel method. *Journal of Materials Science* **1996,** *31*, 3617-3621.

47.   Xiao, X.; Liu, X.; Wang, L.; Zhao, H.; Hu, Z.; He, X.; Li, Y., LiCoO2 Nanoplates with Exposed (001) Planes and High Rate Capability for Lithium-Ion Batteries. *Nano. Res.* **2012,** *5* (6), 395-401.

48.   Maiyalagan, T.; Jarvis, K. A.; Therese, S.; Ferreira, P. J.; Manthiram, A., Spinel-type lithium cobalt oxide as a bifunctional electrocatalyst for the oxygen evolution and oxygen reduction reactions. *Nat. Commun.* **2014,** *5*, 1-8.

49.   Zhu, M.; Park, J.; Sastry, A. M., Fracture Analysis of the Cathode in Li-Ion Batteries: A Simulation Study. *Journal of The Electrochemical Society* **2012,** *159* (4), A392-A498.

50.   Gummow, R. J.; Liles, D. C.; Thackeray, M. M., Spinel versus layered structures for lithium cobalt oxide synthesised at 400°C. *Materials Research Bulletin* **1993,** *28* (3), 235-246.

51.   Vetter, J.; Novak, P.; Wagner, M. R.; Veit, C.; Moller, K.-C.; Besenhard, J. O.; Winter, M.; Wohlfahrt-Mehrens, M.; Vogler, C.; Hammouche, A., Ageing mechanisms in lithium-ion batteries. *Journal of Power Sources* **2005,** *147*, 269-281.

52.   Tejedor-Tejedor, M. I.; Anderson, M. A., Protonation of Phosphate on the Surface of Goethite As Studied by CIR-FTIR and Electrophoretic Mobility. *Langmuir* **1990,** *6* (3), 602-611.

53.   Kwon, K. D.; Kubicki, J. D., Molecular Orbital Theory Study on Surface Complex Structures of Phosphates to Iron Hydroxides: Calculation of Vibrational Frequencies and Adsorption Energies. *Langmuir* **2004,** *20*, 9249-9254.

54.   Gong, W., A real time in situ ATR-FTIR spectroscopic study of linear phosphate adsorption on titania surfaces. *International Journal of Mineral Processing* **2001,** *63*, 147-165.

55.   Connor, P. A.; McQuillan, A. J., Phosphate Adsorption onto TiO2 from Aqueous Solutions: An in Situ Internal Reflection Infrared Spectroscopic Study. *Langmuir* **1999,** *15*, 2916-2921.

56.   Bozich, J.; Hang, M.; Hamers, R.; Klaper, R., Core Chemistry Influences the Toxicity of Multicomponent Metal Oxide Nanomaterials, Lithium Nickel Manganese Cobalt Oxide, and Lithium Cobalt Oxide to *Daphnia magna*. *Environmental Toxicology and Chemistry* **2017,** *36* (9), 2493-2592.

57.   Gunsolus, I. L.; Hang, M. N.; Hudson-Smith, N. V.; Buchman, J. T.; Bennett, J. W.; Conroy, D.; Mason, S. E.; Hamers, R. J.; Haynes, C. L., Influence of nickel manganese cobalt oxide nanoparticle composition on toxicity toward Shewanella oneidensis MR-1: redesigning for reduced biological impact. *Environ. Sci.: Nano* **2017,** *4* (3), 636-646.

58.   Hang, M. N.; Gunsolus, I. L.; Wayland, H.; Melby, E. S.; Mensch, A. C.; Hurley, K. R.; Pedersen, J. A.; Haynes, C. L.; Hamers, R. J., Impact of Nanoscale Lithium Nickel Manganese

Cobalt Oxide (NMC) on the Bacterium Shewanella oneidensis MR-1. *Chemistry of Materials* **2016,** *28*, 1092-1100.

59.   Torrent, J.; Schwertmann, U.; Barron, V., Phosphate sorption by natural hematites. *European Journal of Soil Science* **1994,** *45* (1), 45-51.

60.   Strauss, R.; Brummer, G. W.; Barrow, N. J., Effects of crystallinty of goethite: II. Rates of sorption and desorption of phosphate. *European Journal of Soil Science* **1997,** *48*, 101-114.

61.   Huang, X.; Bennett, J. W.; Hang, M. N.; Laudadio, E. D.; Hamers, R. J.; Mason, S. E., Ab Initio Atomistic Thermodynamics Study of the (001) Surface of LiCoO2 in a Water Environment and Implications for Reactivity under Ambient Conditions. *The Journal of Physical Chemistry C* **2017,** *121* (9), 5069-5080.

62.   Bennett, J. W.; Jones, D.; Huang, X.; Hamers, R. J.; Mason, S. E., Dissolution of complex metal oxides from first-principles and thermodynamics: Cation removal from the (001) surface of Li(Ni1/3Mn1/3Co1/3)O2. *Environ. Sci. Technol.* **2018,** *52* (10), 5972-5802.

63.   Bennett, J. W.; Bjorklund, J. L.; Forbes, T. Z.; Mason, S. E., Systematic Study of Aluminum Nanoclusters and Anion Adsorbates. *Inorganic Chemistry* **2017,** *56*, 13014-13028.

64.   Wilkins, R. G., *The study of kinetics and mechanism of reactions of transition metal complexes*. Allyn and Bacon, Inc: Boston, Massachusetts, 1974.

65.   Lowry, G. V.; Hill, R. J.; Harper, S.; Rawle, A. F.; Hendren, C. O.; Klaessig, F.; Nobbmann, U.; Sayre, P.; Rumble, J., Guidance to improve the scientific value of zeta-potential measurements in nanoEHS. *Environ. Sci.: Nano* **2016,** *3* (953-965).

66.   Swan, J. W.; Furst, E. M., A simpler expression for Henry's function describing the electrophoretic mobility of spherical colloids. *Journal of Colloid and Interface Science* **2012,** *388*, 92-94.

67.   Bhattacharjee, S., DLS and zeta potential - What they are and what they are not? *Journal of Controlled Release* **2016,** *235*, 337-351.

68.   Satoh, A.; Chantrell, R. W.; Coverdale, G. N., Brownian Dynamics Simulations of Ferromagnetic Colloidal Dispersions in a Simple Shear Flow. *Journal of Colloid and Interface Science* **1999,** *209*, 44-59.

69.   Patel, V. R.; Agrawal, Y. K., Nanosuspension: An approach to enhance solubility of drugs. *J. Adv. Pharm. Tech. Res.* **2011,** *2* (2), 81-87.

70.   Fox, L. E.; Sager, S. L.; Wofsy, S. C., Factors controlling the concentrations of soluble phosphorus in the Mississippi estuary. *Limnology and Oceanography* **1985,** *30* (4), 826-832.

71.   Phenrat, T.; Saleh, N.; Sirk, K.; Tilton, R. D.; Lowry, G. V., Aggregation and Sedimentation of Aqueous Nanoscale Zerovalent Iron Dispersions. *Environ. Sci. Technol.* **2007,** *41*, 284-290.

72.   Zhou, D.; Keller, A. A., Role of morphology in the aggregation kinetics of ZnO nanoparticles. *Water Research* **2010,** *44*, 2948-2956.

73.   Arai, Y.; Sparks, D. L., ATR–FTIR Spectroscopic Investigation on Phosphate Adsorption Mechanisms at the Ferrihydrite–Water Interface. *Journal of Colloid and Interface Science* **2001,** *241* (2), 317-326.

74.   Babbitt, C. W.; Williams, E.; Kahhat, R., Institutional Disposition and Management of End-of-Life Electronics. *Environ. Sci. Technol.* **2011,** *45* (12), 5366-5372.

75.   Wang, X.; Gaustad, G.; Babbitt, C. W.; Bailey, C.; Ganter, M. J.; Landi, B. J., Economic and environmental characterization of an evolving Li-ion battery waste stream. *J. Environ. Manage.* **2014,** *135*, 126-134.

76.   Zeng, X. L.; Li, J. H.; Liu, L. L., Solving spent lithium-ion battery problems in China: Opportunities and challenges. *Renew. Sust. Energ. Rev.* **2015,** *52*, 1759-1767.

77.   Li, J. H.; Zeng, X. L.; Chen, M. J.; Ogunseitan, O. A.; Stevels, A., "Control-Alt-Delete": Rebooting Solutions for the E-Waste Problem. *Environ. Sci. Technol.* **2015,** *49* (12), 7095-7108.

78.   Ali, S. H.; Giurco, D.; Arndt, N.; Nickless, E.; Brown, G.; Demetriades, A.; Durrheim, R.; Enriquez, M. A.; Kinnaird, J.; Littleboy, A.; Meinert, L. D.; Oberhänsli, R.; Salem, J.; Schodde, R.; Schneider, G.; Vidal, O.; Yakovleva, N., Mineral supply for sustainable development requires resource governance. *Nature* **2017,** *543*, 367.

Chapter 3. Interaction of Phosphate with Lithium Cobalt Oxide Nanoparticles: A Combined Spectroscopic and Calorimetric Study.

All of the experiments, data acquisition and analysis, and manuscript preparation and revision were done by Elizabeth D. Laudadio under the advisement of Robert J. Hamers except for the following:

Curtis M. Green collected the transmission electron micrographs shown in Figure 3.1.b and 3.1.c. Poorandokht Ilani-Kashkouli collected and analyzed the flow microcalorimetry data and ion chromatography data shown in Figure 3.2a, 3.2b, and 3.3a under the advisement of Nadine J. Kabengi.

3.1 Introduction.

The rapid growth in the use of transition metal oxides in emerging technologies such as energy storage brings with it a desire to understand the chemical transformations that these oxides and other nanomaterials undergo in the environment.[1-4] One of the key challenges in understanding the long-term fate of nanomaterials in the environment is that interaction with aqueous systems, adsorption of ions, and acquisition of surface coatings can all alter nanoparticle properties.[5-8] Lithium cobalt oxide ($LiCoO_2$) is a good model system for investigation as it is representative of the broader class of layered oxides being used in energy storage[9-12] and as catalysts for water oxidation and other reactions.[13-15] The transformation of $LiCoO_2$ and related materials in model environmental and biological systems has been shown to have impacts both on nanomaterial

properties and model organisms.[16-20] Phosphate ion is a particularly important model adsorbate because of its well-known role in stabilizing surfaces of geochemical importance and the widespread presence of phosphate in surface waters.[21-23]

One of the key challenges in understanding interaction of phosphate and other small ions with nanomaterials is the difficulty in characterizing the important kinetic and thermodynamics factors that control their interaction. We showed previously that phosphate ion irreversibly adsorbs to $LiCoO_2$, altering the surface charge and therefore the dispersibility of the nanomaterials in aqueous solutions.[6] To understand the chemical bonding in more detail, chemically specific probes such as time-course in situ infrared spectroscopy can provide information on structure and bonding, while thermodynamic measurements such as microcalorimetry can determine the energetics of ion adsorption.[24-31] Together, these in situ measurements provide new insights into the nature of bonding at complex oxide surfaces and the thermodynamics of ion adsorption.

Here, we present an investigation combining in situ FTIR with in situ flow microcalorimetry to probe the structure and energetics of phosphate ion interaction with nanosheets of $LiCoO_2$ at different pH values relevant to environmental systems.[32-33] The use of high surface area nanoparticles provides the sensitivity needed to investigate adsorption at sub-monolayer coverages, while layered 2D nanosheets expose almost entirely one crystal plane which thereby minimizes heterogeneity of the exposed surfaces.[34-35] To help overcome spectral broadening and analyze the temporal evolution of the spectra, we use two-dimensional correlation analysis of FTIR data obtained as a function of time.[36-38] Our work directly reveals that phosphate adsorption at circumneutral pH occurs by two distinct steps that we interpret as a transition from a monodentate coordinated phosphate to a bidentate coordinated phosphate. This study highlights need for powerful and complimentary in situ techniques to assess all aspects of these interactions.

3.2 Experimental Section.

3.2.1. General.

All experiments were conducted using ACS reagent grade chemicals, and all aqueous solutions were prepared in ultrapure water (18.2 MΩ) unless otherwise noted. All sonication was performed in a Cole Parmer Ultrasonic Processor operating with a maximum power of 750 W.

3.2.2. LiCoO$_2$ nanoparticle synthesis and characterization.

We synthesized sheet-like nanoparticles of LiCoO$_2$ as described previously.[6, 34] Briefly, we synthesized a Co(OH)$_2$ precursor by dropwise addition of 20 mL of 1 M Co(NO$_3$)$_2$•6H$_2$O to 420 mL of 0.1 M solution of LiOH, ensuring a [OH] 5% stoichiometric excess for Co^{2+} + 2OH$^-$ → Co(OH)$_2$. The precipitate was isolated by centrifuging into a pellet (4696×g, 3 min) and decanting the supernatant. The product was then washed a total of three more times by redispersing in water and collecting the pellet by centrifugation. After the final rinse, we decanted the supernatant and dried the product in a vacuum oven at 30 °C overnight. Once dried, 0.5 g of the Co(OH)$_2$ precursor was massed for the lithiation step. A 20 g mixture of a 6:4 molar ratio of LiNO$_3$:LiOH was heated at 200 °C in a polytetrafluoroethylene container and assembled in a silicone oil bath under magnetic stirring, forming a molten salt flux. The Co(OH)$_2$ precursor was added to the molten salt and after 30 min, the flux was quenched with water. The product was then collected and washed through four cycles of dispersion/isolation via centrifugation in water, as described above. The product was then dried in a vacuum oven at 30 °C overnight.

3.2.3. Characterization of LiCoO$_2$ nanoparticles.

We obtained x-ray diffraction (XRD) patterns of the LiCoO$_2$ nanoparticles using a Bruker D8 Advance powder diffractometer with a Cu Kα source and a Lynxeye detector. Concentrated dispersions of LiCoO$_2$ powders in isopropyl alcohol were prepared through ultrasonication. The

mixture was then drop-cast onto a zero diffraction plate (MTI Corp) and allowed to dry, forming a uniform film of material. The powder XRD pattern was acquired using a step size of 0.20° and dwell time of 165 s at each point. To characterize nanoparticle morphology using scanning electron microscopy (SEM), $LiCoO_2$ was dispersed in methanol and spin-coated onto low-resistivity (<0.1 $\Omega\cdot$cm) B-doped Si wafers. Images were acquired using a Leo Supra55 VP SEM, 3 kV electron energy, using a secondary electron detector. The morphology of $LiCoO_2$ nanoparticles was further analyzed with a transmission electron microscope (TEM, FEI Tecnai T12) at 120 kV. TEM grids were prepared by drop-casting suspensions of $LiCoO_2$ nanoparticles in water onto a carbon-supported TEM grid, which was allowed to dry overnight. The lithiation state of the $LiCoO_2$ nanoparticles was assessed by digesting the particles in aqua regia (3:1 v/v ratio of 39% HCl and 68% HNO_3, *caution: highly corrosive!*) and analyzing ion concentrations using inductively coupled plasma – optical emission spectroscopy (ICP-OES), yielding a nanoparticle stoichiometry of $Li_{0.92}CoO_2$.

3.2.4. Flow Microcalorimetry.

The flow microcalorimeter used in this study was custom-designed and fabricated in the Kabengi laboratory at Georgia State University. A description of the instrumentation and basic operation has been detailed previously.[26-27, 29] Only a brief description outlining the basic principles of obtaining data and experimental procedures relevant to this study is provided here. To prepare samples for microcalorimetry, we homogeneously packed a 10.0 ± 0.5 mg sample of $LiCoO_2$ nanoparticles into a small region of the flow path and equilibrated with 1 mM LiCl at a flow rate of 0.30 ± 0.02 mL/min. During operation, the liquid temperature was continuously monitored by two thermistors flanking the sample holder and the temperature of each thermistor was recorded every 5.0 s. This voltage across the thermistor was amplified and recorded as a function of time.

After thermal equilibrium was reached, the input solution was switched to a solution of 0.9 mM LiCl and 0.1 mM LiH_2PO_4, i.e. keeping the total concentration of Li^+ at 1 mM. The differential thermal signal resulting from the interaction of phosphate species with the $LiCoO_2$ sample was recorded, and the calorimetric peak thus obtained numerically integrated and converted to energy units (Joules) by calibrating the instrument response using heat pulses of known energy. The amount of phosphate adsorbed on the surface was determined by a mass balance calculation using the known total mass injected and a measurement of the mass recovered from effluent samples, which were analyzed for total aqueous concentration of phosphate using High-Performance Liquid Chromatography – Ion conductivity (Metrohm, USA).

We probed the interaction of phosphate with $LiCoO_2$ nanoparticles at three pH values: 5.60 ± 0.05, 7.4 ± 0.5, and 9.0 ± 0.5. In order to avoid possible effects due to competitive adsorption that can occur when using buffer solutions, we did not use buffers and instead controlled solution pH by monitoring the value and adjusting as needed using 2 µL increments of 0.1 M LiOH or 0.1 M HCl as needed. Changes in total concentration and ionic strength resulting from pH adjustments were determined to be less than $\leq 1\%$. The pH of the influent and effluent solutions was monitored to ensure it remained constant during the course of the experiments.

3.2.5. Quantification of phosphate adsorption with X-ray Photoelectron Spectroscopy (XPS).

To quantify the adsorption of phosphate onto $LiCoO_2$, we used XPS measurements of photoelectron emission from the P(2p) and Co(2p) levels. We prepared samples for XPS by suspending 5 mg $LiCoO_2$ nanoparticles in 50 mL of a 1 mM Na_2HPO_4 solution at the three pH values studied (pH 5.6, pH 7.4, pH 9.0, pH of solutions adjusted using either 1 M HCl or 1 M NaOH) After suspending for hour, we isolated the particles through centrifugation (4696×g, 5

min), redispersed in water, and isolated again through centrifugation (14104×g) for 5 minutes. The pellet of particles was then dried under vacuum overnight. We pressed the dried particles into indium foil on a copper foil backing to ensure the sample was of homogenous flatness and thickness and could make good electrical contact with the sample holder. XPS spectra were measured using a Thermo Fisher Scientific K-alpha XPS using at a 45° photoelectron takeoff angle, measuring the Li (1s), Co(2p), O(1s), Na(1s), C(1s) and P(2p) peaks. XPS spectra were fit using CasaXPS software.[38] Co(2p) and P(2p) peak areas were used for quantitative analysis of surface coverage using the following equation:

$$Coverage = \frac{A_{P,2p}}{A_{Co,2p}} \times \frac{SF_{Co,2p}}{SF_{P,2p}} \times \frac{Scans_{Co,2p}}{Scans_{P,2p}} \times \rho_{Co,2p} \times \lambda_{Co,2p} \times cos\,\theta$$

Where A = peak area, SF = atomic sensitivity factor ($SF_{Co,2p}$ = 18.23529, $SF_{P,2p}$=1.352941), ρ= density of cobalt in $LiCoO_2$ (30 atoms/nm^3), λ = inelastic mean free path (IMFP) of Co electron emitted from $LiCoO_2$ (1.9 nm, calculated from the NIST database[39] via the TPP-2M equation.[39-40]), θ= Angle of the analyzer to the surface normal (45° for the instrument used here). The coverage equation makes the assumption that the adsorbed layer is thinner than the IMFP of a Co(2p) photoelectron, 1.9 nm. Scans refers to the number of scans that were averaged to achieve the total peak area. Spectra were background subtracted with a Shirley function and peaks were fit using a 30% Gaussian, 70% Lorentzian line shape.

3.2.6. Characterization of LiCoO₂ nanosheet zeta potential.

Dynamic Light Scattering (DLS) and Laser Doppler Microelectrophoresis measurements were taken with a Malvern Zetasizer Nano ZS. A 250 mg/L stock solution of $LiCoO_2$ was prepared in 1 mL of ultrapure water and sonicated for 1 h in a water-cooled cup ultrasonicator (10 s on, 10 s off for 30 min total sonication time) before analysis. DLS measurements were performed on 1 mg/L $LiCoO_2$ suspensions either in 300 µM NaCl as an approximate ionic strength control, or 100

μM Na_2HPO_4 at the pH values studied (pH 5.6, pH 7.4, pH 9.0). The pH values were achieved by additions of microliter quantities of either 1 M HCl or 1 M NaOH. Three size measurements were taken (approximately 6 minutes) followed by three zeta potential measurements (approximately 5 minutes). The data shown are averages of three experimental replicates for each data point. To avoid possible effects of aggregation, the stock $LiCoO_2$ solution was left sonicating between measurements. SEM images of stock solutions before and after sonication show no change in the nanoparticle morphology (Figure A.3.1).

3.2.7. Preparation of LiCoO₂ layers for attenuated total reflectance – FTIR (ATR-FTIR).

Thin layers of $LiCoO_2$ were prepared by spin-coating $LiCoO_2$ suspensions onto a zinc selenide (ZnSe) trapezoidal prism acting as a 10-bounce internal reflection element (IRE). We prepared $LiCoO_2$ suspensions of 1000 mg/L in 2 mL methanol. Solutions were sonicated for 1 h in a cup ultrasonicator with cooling water (10 s on, 10 s off for 30 min total sonication time). To ensure that the ZnSe IREs were clean, we rinsed them with water followed by methanol, dried with N_2, and exposed to UV light from a low-pressure Hg grid lamp (UV Products) in air for at least 10 min before use. We then spin-coated the $LiCoO_2$ suspension onto the clean ZnSe IREs using 25 repeated applications of 75 μL each and spinning for 30 s at 1000 rpm after each application. The layer was then stabilized by heating in a box furnace at 400 °C for 5 min. The ZnSe element was allowed to cool for at least 12 h before using. SEM images of $LiCoO_2$ layers prepared on Si wafers using this method show that the nanoparticles are randomly oriented (Figure A.3.2).

3.2.8. ATR-FTIR studies of phosphate adsorption to LiCoO₂ surfaces.

ATR-FTIR spectra were acquired using the previously described $LiCoO_2$-coated ZnSe IREs assembled in a flow cell (Specac) using a Bruker Vertex 70 FTIR spectrometer. Spectra were

acquired at 4 cm^{-1} resolution, averaging 500 scans per spectrum. The experiment was performed at a fixed pH of 7.4, using solutions of 100 µM Na_2HPO_4 or pH-adjusted water, where pH was controlled by addition of microliter quantities of 1 M HCl or 1 M NaOH as needed. In each experiment, at reference spectrum was obtained after flowing 1 mL of pH 7.4 water over the $LiCoO_2$-coated ZnSe at 0.5 mL/min. After obtaining the water baseline, a solution of 100 µM pH 7.4 Na_2HPO_4 was then flowed (0.5 mL/min) while continually collecting spectra (approximately 2 minutes per spectrum) for a total duration of 1 hr. All spectra shown here are presented as absorption spectra at different times t, defined as, $A(\tilde{v}, t) = -log_{10}\left(\frac{I(\tilde{v},t)}{I(\tilde{v},0)}\right)$ where I($\tilde{v}$,t) is the observed intensity of transmitted light as a function of wavenumber($\tilde{v}$) measured at time t, and t=0 corresponds to the initial spectrum taken after flowing pH 7.4 water over the $LiCoO_2$ film. The volume of the cell is 0.55 mL, and so for each 1 hr interval during which solutions were flowed at 0.5 mL/min, approximately 54 full volume exchanges of the flow cell occurred. FitYK software was used to peak fit the final spectrum.[41]

3.2.9. Two-dimensional correlation spectroscopic analysis of ATR-FTIR data.

Two-dimensional correlation spectroscopy (2D-COS) analysis of infrared spectra is a method used to investigate spectral changes as a function of an external perturbation or variable.[36-38] We employed this technique to assess spectral changes as a function of time. Time-course ATR-FTIR spectra were obtained as detailed above. Using a custom program in Igor Pro software, calculated the time-dependent absorption spectra and removed residual baselines in the region of primary interest (1200 - 800 cm^{-1}) by a simple linear fit to the absorbance at the edges of this region (1400 – 750 cm^{-1}). The 2D-COS plots were obtained Fourier-transforming the spectra obtained at different times and taking the cross-correlation in the frequency domain using the equation:

$$\phi_{(v_1,v_2)} + i\psi_{(v_1,v_2)} = \frac{1}{\pi T} \sum_{n=0}^{n=N-1} \tilde{Y}_1(\tilde{v}_1, \omega = n\omega_0)\tilde{Y}_2^*(\tilde{v}_2, \omega = n\omega_0)$$

In this equation, $\tilde{Y}_1(\tilde{v}_1, \omega)$ is the Fourier transform (in time) of the absorbance spectra $A(\tilde{v}, t)$, which were measured at N equally spaced time intervals Δt over a total time T such that $T=n\Delta t$ where $n = 0, \dots N - 1$. We calculated the discrete Fourier transform $\tilde{Y}_1(\tilde{v}, \omega)$ as:

$$\tilde{Y}_1(\tilde{v}, \omega) = \frac{1}{2\pi} \sum_{m=0}^{m=N-1} e^{2\pi im/N} A(\tilde{v}, t = n\Delta t)$$

where $\omega = m\omega_0$ (m=0,...,N/2) and $\omega_0 = 2\pi/T$. Note that the frequency ω is related to the times t at which the spectra were acquired, while $\tilde{v}$ refers to the spectral frequencies as conventionally represented in wavenumbers, cm^{-1}. The resulting complex function yields two-dimensional data, where $\phi_{(v_1,v_2)}$ is the synchronous 2D correlation plot and $\psi_{(v_1,v_2)}$ is the asynchronous 2D correlation plot. The synchronous and asynchronous correlation plots can be analyzed via Noda's rules,[36] which describe the relationship between the signs of the cross peaks and the changes in spectral intensity.[36-38] Cross-peaks of identical sign in the synchronous plot indicate that the changes in the absorbance of these regions as a function of time either increase or decrease in the same direction, whereas cross-peaks of opposite signs indicate that the changes occur such that one band increases while the other decreases. The sequential order of the changes in bands can then be determined by relating the signs of the synchronous plot to asynchronous plot. If the signs of the features in the asynchronous and synchronous plots are the same, the change in the X axis band ($\tilde{v}_1$) occurs before the Y axis band ($\tilde{v}_2$). If the signs are opposite, the change in the X axis band ($\tilde{v}_1$) occurs after the Y axis band ($\tilde{v}_2$). The symmetry properties of the above calculations

force the synchronous plot to be symmetric about the diagonal, while the asynchronous plot must be anti-symmetric about the diagonal.

3.3 Results and Discussion.

3.3.1. LiCoO₂ nanoparticle synthesis characterization.

Figure 3.1a shows a representative SEM micrograph of nanoparticles used for this study. SEM reveals a sheet-like morphology of LiCoO$_2$ nanoparticles. Further morphology analysis with TEM is shown in Figure 3.1b and 3.1c, where individual particles imaged edge-on reveal the lattice planes of the layered material. Figure 3.1d shows a powder XRD pattern collected from these particles. The pattern can be indexed to the R$\bar{3}$m space group by comparison of the collected XRD pattern to that of single crystal LiCoO$_2$.[35] While the lack of full separation of the (018) and (110) peaks may indicate the presence of residual spinel phases,[42] the inability to resolve these individual peaks could also be due to the peak-broadening that occurs when acquiring XRD patterns of nanoparticles. We expect these particles to be reasonable models for the degradation of the cathode materials in lithium ion batteries, where mechanical fracture following electrochemical cycling is common.[43] We note that while in the pristine material the basal plane of LiCoO$_2$ is terminated in lithium, because the material is an intercalation compound, the lithium ions are highly mobile and likely to undergo Li$^+$/H$^+$ exchange in solution. This has been demonstrated experimentally[44] as well as computationally.[45] Analysis of lithium release from LiCoO$_2$ in the presence of phosphate shows that approximately 30% of the total lithium is released, which we believe is consistent with the total amount of lithium released being mostly limited to the surface lithium (Figure A.3.3). We therefore expect the surface of the materials in aqueous solutions to be hydroxylated instead of lithium terminated.

3.3.2. Energetics of interaction from flow microcalorimetry.

Figure 3.2a shows microcalorimetry data obtained from phosphate exposure to $LiCoO_2$ at three different values of pH; pH 5.6 (pink trace), pH 7.4 (green trace), and pH 9.0 (blue trace). In each case, when LiCl is substituted with Li_2HPO_4-containing solutions, a positive calorimetric signal is detected. This sign is consistent with heat being released following phosphate interaction with $LiCoO_2$, indicating a negative enthalpy of adsorption. However, the shapes of the heat release profiles at each pH are significantly different.

This is most obvious at pH 7.4, where the heat release is greatest in magnitude at each time point and shows two distinct features: an initial heat of release over ~20 minutes, followed by a slower release of heat over ~40-60 minutes. The calorimetric signal can be converted to a heat of adsorption (Q_{ads}) by integrating the curves and using the calibration of an internal standard to convert V•min to mJ, which was then normalized by the mass of the $LiCoO_2$ in each experiment.

Figure 3.2b shows the values of Q_{ads} obtained at each pH studied. The value of Q_{ads} at pH 7.4 is -5.16 mJ/mg, which is approximately twice of what is released at pH 5.6, -2.28 mJ/mg. Q_{ads} at pH 9.0 is the smallest in magnitude, at -0.90 mJ/mg.

3.3.3. Determination of Surface Coverage.

We determined the amount of phosphate adsorbed to $LiCoO_2$ using two complementary approaches. In one, we collected the effluent from the microcalorimetry apparatus and measured phosphate concentration (via ion chromatography) and effluent volume to get the total number of moles of phosphate in the effluent, and subtracted this from the total moles of phosphate introduced into the system during the same time interval. The resulting difference represents the amount of phosphate adsorbed to the $LiCoO_2$ nanoparticles during the microcalorimetry experiment. Figure

3.3a shows that the amount adsorbed at pH 5.6 and 7.4 were similar to one another, while the amount adsorbed at pH 9.0 was much lower.

We also quantified the phosphate adsorption using XPS by exposing samples to phosphate at different pH values. We determined the absolute surface coverage of phosphorus using the area of the Co(2p) peaks as an internal standard (Figure A.3.4) which were analyzed to yield the coverage values shown in Figure 3.3. We confirmed the coverage using the bulk O(1s) intensity as an internal standard, with nearly identical results. These data show that the phosphate coverage (in atoms phosphorus / nm^2) decreases from 1.4 at pH 5.6 to 0.6 at pH 9.0. A single-factor ANOVA test reveals that the phosphate coverage at pH 5.6 and pH 7.4 are indistinguishable, while the lower coverage at pH 9.0 is statistically lower than the values at pH 5.6 and pH 7.5 ($p < 0.02$).

Both the microcalorimetry data and XPS data show that the phosphate coverage is similar at pH 5.6 and 7.4, but significantly lower at pH 9. By using the specific surface area of the nanoparticles as determined from Brunauer-Emmett-Teller adsorption analysis, the microcalorimetry data can be represented as an atomic number density (atoms / nm^2), the same units of the coverages from XPS analysis (detailed calculation in Supporting Information). Coverage values from ion chromatography when converted to units of atoms/nm^2 are 0.6 at pH 5.6, 0.7 at pH 7.4, and 0.07 at pH 9.0. These values are slightly lower than those determined by XPS, potentially reflecting the fact that in the microcalorimetry experiments some of the surface area that is accessible to gaseous species (as in BET analysis) maybe inaccessible in the geometry of the microcalorimetry experiment. Nevertheless, one important outcome of these experiments is that since the amount of phosphate adsorbed at pH 7.4 is comparable to that adsorbed at pH 5.6, we conclude that the higher amount of heat evolved at pH 7.4 cannot be accounted for on the basis

of greater phosphate adsorption, but rather indicates that the specific chemical processes occurring at pH 7.4 are more exothermic.

3.3.4. Analysis of apparent zeta potential as an indication of relative surface charge.

We characterized the influence of phosphate exposure on the nanoparticle surface charge using measurements of the electrophoretic mobility and apparent zeta potential. Because our nanoparticles have a flake-like geometry, the hydrodynamic equations typically used to relate mobility to zeta potential are not strictly applicable.[46-47] We therefore include the measured electrophoretic mobilities values and also the apparent zeta potential as derived from Henry's Equation, which is defined as $\frac{U}{E} = \frac{2\varepsilon\zeta F(\kappa\alpha)}{3\eta}$, where U/E is the electrophoretic mobility, ζ is the apparent zeta potential, ε is the solvent dielectric permittivity constant, η is the viscosity of the solvent, and F($\kappa\alpha$) is Henry's function, which is approximated to 3/2 in the Smoluchowski model, which is most commonly used for nanomaterials in polar solvent.[46-47]

To control for the influence of solution-phase ions on apparent zeta potential measurements, we also did control experiments using a NaCl solution having a similar ionic strength to the phosphate solutions used here. Figure 3.4 shows the mobilities and apparent zeta potential of LiCoO$_2$ nanoparticles in 100 µM Na$_2$HPO$_4$ (open, orange circles) and in a control experiment consisting of 300 µM NaCl (filled blue circles) at pH 5.6, 7.4 and 9.0. At all pHs studied here, the LiCoO$_2$ nanoparticles have a net negative charge in phosphate and in the NaCl control solution. At pH 5.6, the zeta potential is nearly the same in both NaCl and phosphate, while at higher pH values the LiCoO$_2$ nanoparticles have higher mobility (more negative apparent zeta potential) than those in the NaCl control. We note that the apparent zeta potential of the LiCoO$_2$ nanoparticles in the phosphate solution are approximately -30 mV at the two higher pH values, a value often considered a threshold for forming stable colloids.[48-49] Dynamic light scattering

measurements show that neither pH nor presence of phosphate impact the diffusion coefficient of LiCoO$_2$ under these conditions (Figure A.3.5). When this result is considered in conjunction with the data showing that adsorption of phosphate onto LiCoO$_2$ at pH 7.4 is higher than at pH 9.0, the combination of these results, and the exotherm from the calorimetry experiment, suggest that the difference in the interaction of phosphate with LiCoO$_2$ at pH 7.4 cannot be explained by the surface charge of LiCoO$_2$ as a function of pH. There is a higher amount of phosphate adsorbed, and higher heat released from phosphate interaction with LiCoO$_2$ at pH 7.4 compared with pH 9.0, despite the surface charge of LiCoO$_2$ both in the presence and absence of phosphate being indistinguishable between pHs 7.4 and 9.0.

3.3.5. ATR-FTIR and 2D-COS analysis of the evolution of phosphate vibrational modes on LiCoO$_2$.

In order to understand the thermodynamic trajectory of phosphate interaction with LiCoO$_2$ at pH 7.4, we used ATR-FTIR to characterize the geometry of phosphate adsorbed to LiCoO$_2$ over time. Figure 3.5a shows the final spectrum after the one hour of exposure of phosphate to LiCoO$_2$. Consistent with our prior study[6], adsorption of phosphate species to LiCoO$_2$ results in a single broad feature in the region from 1200 – 800 cm^{-1} that is composed of multiple vibrational contributions. Here we show that the broad feature can be fit to five individual peaks at 1143, 1085, 1032, 993 and 956 cm^{-1}. By comparing the number and frequency of the vibrational modes on the surface of LiCoO$_2$ to a free H$_2$PO$_4^-$ molecule, the final geometry of phosphate on the surface of LiCoO$_2$ can be assigned to a bidentate structure.[50-51] A bidentate geometry on the surface of LiCoO$_2$ has the same symmetry as that of the H$_2$PO$_4^-$ molecule (i.e., Co$_2$PO$_4^-$), and therefore should have the same number of primary infrared active vibrational modes.

The two peaks between 1000 – 900 cm^{-1} are analogous to HO-P asymmetric and symmetric vibrations in $H_2PO_4^-$, shifted to higher wavenumbers on the surface of $LiCoO_2$ due to the difference in bond strength of CoO-P versus HO-P.[50-51] Likewise, the two peaks between 1100 – 1000 cm^{-1} are analogous to the symmetric and asymmetric $(HO)_2PO_2$ vibrations in $H_2PO_4^-$, shifted to lower wavenumbers when bound to $LiCoO_2$ due to the weaker bond strength of $(CoO)_2PO_2$ versus $(HO)_2PO_2$.[50-51] The fifth peak between 1200 – 1100 cm^{-1} can be assigned to a P-OH bending vibration which has been reported to be both broad and weak in spectra.[52] This final binding geometry assignment is consistent with our previous work, though those experiments were done at lower phosphate concentrations.[6]

A close examination of the spectra collected as a function of time (Figure A.3.6) shows that the structure of the phosphate peak changes with time, indicating that there are time-dependent changes in the phosphate geometry on the $LiCoO_2$ surface that occur over the timescale of one hour. These changes are challenging to interpret by eye, as they are subtle differences in the overall broad feature. Employing 2D-COS analysis allows for these subtle differences to be clarified over time. The spectra as obtained over the course of phosphate exposure consist of vibrational contributions from both the adsorbed phosphate and the free phosphate in solution within the penetration depth of the ATR element Because 2D-COS is only sensitive to changes in vibrational modes over time, the confounding signal from the free phosphate is effectively removed in the analysis.

The synchronous plot of the 2D-COS analysis is shown in Figure 3.5b, and the asynchronous plot is shown in Figure 3.5c. The symmetry properties of the correlation analysis dictate that the synchronous spectrum must be symmetric with respect to reflection about the diagonal, while the asynchronous spectrum is antisymmetric (i.e., inverts the sign) across the

diagonal. As a result, the information in the upper-left half-space and lower-right half-space of the plot is redundant. We therefore confine our discussion to the lower-right half-space of each plot.

The synchronous plot in Figure 3.5b shows a single large positive (red) feature in the region from $1200 - 900$ cm^{-1}. The single positive feature indicates that the absorbance of this entire region increasing monotonically as a function of time. This is consistent with the evolution of the one-dimensional spectra over time as shown in Figure A.3.4, where the absorbance of the entire region is seen to be increasing between each spectrum collected over the time interval.

Analysis of the location and sign of the features in the asynchronous plot in Figure 3.5c yields information about the sequential order in which the absorption peaks occur. The asynchronous plot shows two major features. The existence of these correlated features is evidence that the vibrational modes of phosphate, and thus the geometry of phosphate on the surface of LiCoO$_2$, is evolving with time. This is consistent with the microcalorimetry data that indicates the interaction of phosphate and LiCoO$_2$ occurs in two separate exothermic steps over time.

There is a positive (red) peak in the asynchronous plot that is centered at $\tilde{v}_1 = 940 - 910$ cm^{-1} and $\tilde{v}_2 = 1065 - 1030$ cm^{-1}, labeled A in Figure 3.5c. The positive sign of this feature indicates that the absorbance of the modes at $940 - 910$ cm^{-1} is increasing before those at $1065 - 1030$ cm^{-1}. The vibrational analysis conducted on the one-dimensional spectrum in Figure 3.5a revealed two peaks between $1000 - 900$ cm^{-1} that correspond to CoO-P vibrations, and two peaks between $1100 - 1000$ cm^{-1} that correspond to (CoO)$_2$PO$_2$ vibrations, as have been assigned in related studies on different materials.[50-51] The appearance of CoO-P vibrations before (CoO)$_2$PO$_2$ vibrations may indicate that modes related to phosphate binding to LiCoO$_2$ through a single cobalt on the surface are occurring before the modes related to phosphate bound to LiCoO$_2$ through two cobalt atoms, as is such in the final bidentate structure.

The remaining feature in the asynchronous plot is a negative (blue) peak centered at $\tilde{\nu}_1 =$ 1080 – 1000 cm^{-1} and $\tilde{\nu}_2 = 1130 – 1080$ cm^{-1}, labeled B in Figure 3.5c. The negative value of this peak indicates that the vibrational modes at 1130 – 1080 cm^{-1} increase in intensity before the modes at 1080 – 1000 cm^{-1}. The vibrational analysis of the one-dimensional spectrum in Figure 3.5a revealed two peaks between 1100 – 1000 cm^{-1} that correspond to $(CoO)_2PO_2$ vibrations, and a single peak between 1200 – 1100 cm^{-1} that corresponds to P-OH bending vibrations, as have been assigned in related studies on different materials.[50-51]

Our interpretation of this negative feature (labeled B in the asynchronous plot) is that the vibrational modes relating to the P-OH bending motion are occurring in the spectra before the vibrational modes relating to the $(CoO)_2PO_2$ vibrations of the final bidentate surface structure. The two features in the asynchronous plot are consistent with CoO-P and P-OH vibrations both growing into the spectra before $(CoO)_2PO_2$ vibrations. This information, in combination with the flow microcalorimetry results, allow us to propose a hypothesized mechanism of phosphate adsorption onto LiCoO$_2$ at pH 7.4.

3.3.6. Proposed mechanism.

Taking into consideration all of the data presented here, we propose a mechanism for how phosphate interacts with the LiCoO$_2$ surface at pH 7.4. Both XPS and flow calorimetry calculations of phosphate surface coverage on LiCoO$_2$ revealed that a comparable amount of phosphorus is retained on the surface of LiCoO$_2$ at both pH 5.6 and pH 7.4, indicating that the noticeable difference in the profile of the heat release in the flow microcalorimetry data cannot be due to a larger amount of phosphate adsorbing to the surface. The 2D-COS analysis revealed correlations in time evolution between the vibrational modes of phosphate, indicating that both P-OH bending modes and CoO-P modes occur before the $(CoO)_2PO_2$ vibrations. Scheme 1 shows the proposed

mechanism of interaction based on the whole of the data presented here. We propose that phosphate in the form of $H_2PO_4^-$ (roughly 50% of phosphate present at pH 7.4) first forms a hydrogen bond with the hydroxylated $LiCoO_2$ surface as shown in the step labeled A of Scheme 1. Density functional theory calculations have shown that this step is thermodynamically favorable on a partially hydroxylated $LiCoO_2$ surface.[45] Following hydrogen bond formation, a phosphoryl transfer reaction results in the loss of water and formation of a covalent bond between the phosphate and the $LiCoO_2$ surface, forming a monodentate structure on the surface as shown in the second structure of Scheme 1 labeled B. The loss of water is an exothermic process, and we attribute the first peak in the flow calorimetry data to this surface reaction. At this point, the adsorbed phosphate molecule can exhibit both CoO-P stretching modes and P-OH bending modes, consistent with these modes developing first in the 2D-COS plots of the FTIR spectra. The phosphate in the structure labeled "B" can then further react with another hydroxylated group on $LiCoO_2$ through a subsequent phosphoryl transfer reaction. Another molecule of water is released, consistent with the second exothermic process identified in the flow microcalorimetry. The phosphate molecule is then in a bidentate geometry on the $LiCoO_2$ surface, consistent with the 2D-COS analysis showing that the $(CoO)_2PO_2$ vibrations grow into the spectra later than the other modes. If the two distinct features in the calorimetry trace are fit separately, the area under each curve is comparable, consistent with the exothermic process at each step resulting from a similar reaction: the release of a water molecule. The P-OH bending vibrations do not decrease in the spectra, which may suggest that the phosphate can be further protonated once adsorbed or that not all the monodentate structures are converted to bidentate. The observation that this bimodal interaction is not observed at other pH values may suggest that factors such as concentration of the different dissolved forms of hydrogen phosphate, relative proportions of hydroxylated groups on

$LiCoO_2$, as well as exposure time and flow rate are all likely to play a role in how the interaction of phosphate with $LiCoO_2$ surfaces progress with time. At pH 5.6, we speculate that the Step 1 of our proposed mechanism may occur more quickly due to the higher percentage of $H_2PO_4^-$ (~98%) and more positive surface charge of $LiCoO_2$, such that the available surface sites are filled before Step 2 can occur. At pH 9.0, only ~2% of the phosphate exists as $H_2PO_4^-$. We suspect that the more significant electrostatic repulsion between the surface and the dominant HPO_4^{2-} versus $H_2PO_4^-$ may be a factor in the lower coverage observed.

The oxygen-oxygen distance between nearest-neighbor oxygen atoms in the basal plane of $LiCoO_2$ (2.816 Å) is very similar to the oxygen distances in the orthophosphate molecule, and previous crystallographic comparisons on other materials have shown that the bidentate conformation of phosphate on the surface of other metal oxides is geometrically feasible.[53] The oxygen-oxygen distances in $LiCoO_2$ are further comparable to the oxygen-oxygen bond distances in several bulk cobalt phosphates such as where oxygen-oxygen distances are 2.5 – 2.8 Å on average for cobalt tetrametaphosphate[54], cobalt phosphate[55], and cobalt diphosphate,[56] which further supports the model of a bidentate surface adsorption and formation of an inorganic cobalt phosphate coating presented here.[54-56]

While the concentrations of phosphate studied here are higher than typical environmental concentrations, the final coordination of phosphate on the surface of $LiCoO_2$ at 100 μM phosphate is the same as we determined in our previous study at a more environmentally relevant concentration of 1 μM phosphate. The model present here is consistent with our previous study in which we found that phosphate adsorption occurs even at environmentally relevant concentration of $<10^{-4}$ M and that this adsorption was irreversible, demonstrated by the fact that rinsing phosphate-exposed $LiCoO_2$ with water did not dislodge phosphate once adsorbed to the surface.

Our present result indicate that the reason for this irreversible behavior is that phosphate interaction is not a simple adsorption process but is better described as a condensation reaction in which the free energy change associated with formation and release of water molecules drives the interaction to a new structure like that in Scheme 1.

The irreversible, exothermic nature of phosphate surface adsorption suggests that possibility that adsorption of phosphate to $LiCoO_2$ could be the first step of a transformation to a new bulk cobalt phosphate composition. To test whether the initial adsorption investigated here continues to form a bulk phosphate over longer periods of time, we conducted a limited number of experiments using nanoparticles that were exposed to 1 mM Na_2HPO_4 at pH 7.4 for 5 months. XPS analysis of nanoparticles after 5 months of exposure (Figure A.3.7a) yields coverage values on the order of ~1 atom P/nm^2, comparable to the values obtained after just one hour of exposure. This similarity suggests that phosphate adsorption is limited to the exterior surface of the nanomaterials.

SEM micrographs (Figure A.3.7b) show that the flake-like morphology is retained after long-term phosphate exposure, evidence of a self-limiting phosphate adsorption that does not alter the overall morphology of the material. However, powder XRD data (Figure A.3.7c) show that long-term exposure leads to a significant broadening of the diffraction features. Prior studies have shown that $LiCoO_2$ can easily undergo Li^+/H^+ site exchange by releasing Li^+ and intercalating H^+ to conserve overall charge neutrality, and that this occurs without disruption of the particle morphology.[57-58] Our data suggest that the diffraction peak broadening and associated loss of crystallinity arises from this H^+/Li^+ site exchange, forming a transformed material whose bulk composition more closely resembles that of a cobalt hydroxide, while the surface composition resembles a cobalt phosphate, with phosphate ions remaining adsorbed at the surface only.

3.4 Conclusions.

The studies presented here demonstrate that the combination of flow microcalorimetry and FTIR can provide unique molecular-level insights into the nature of molecular adsorption and reaction processes at solid-liquid interfaces. In the case of $LiCoO_2$, flow microcalorimetry data reveal two distinct exothermic surface processes occurring at pH 7.4. By combining flow microcalorimetry with in situ FTIR and correlation analysis, our data indicate that phosphate and $LiCoO_2$ interact via a two-step process at pH 7.4, in which evolution of water at two distinct steps in the adsorption process gives rise to two exothermic peaks in the flow calorimetry data. While this study demonstrates the power of both flow microcalorimetry and time-sequential FTIR measurements with 2D-COS analysis, it highlights the depth of information that is obtained by using the two techniques in conjunction with one another that is not possible with either one independently.

Our data indicate that the interaction of phosphate with $LiCoO_2$ is best described as a condensation reaction in which the release of water molecules provides a strong driving force for reaction, but this reaction is limited to only a surface layer and does not continue toward a bulk transformation under ambient conditions. Understanding the interaction of anions such as phosphate with transition metal oxide nanomaterials may have important consequences for understanding the long-term environmental impact associated with accidental release or improper disposal of nanomaterials. Since there is currently no large-scale infrastructure for recycling of $LiCoO_2$ and related transition metal oxides used in lithium ion batteries, understanding the transformations of these materials can help to predict the potential environmental impact associated with their overall life cycle.

3.5 Figures.
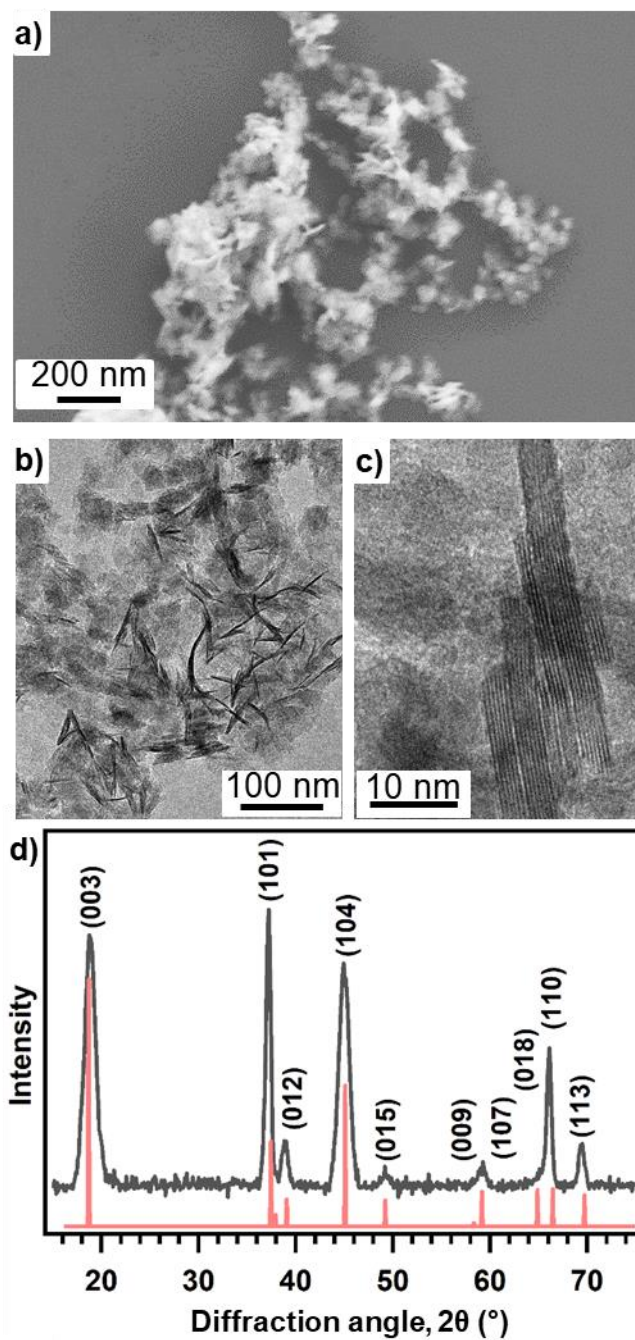
Figure 3.1. a) scanning electron micrograph of the nanosheets of $LiCoO_2$. b) transmission electron micrograph of $LiCoO_2$. c) higher magnification transmission electron micrograph of $LiCoO_2$ edge-on. d) powder x-ray diffraction pattern of $LiCoO_2$ nanosheets (gray) which can be indexed to the

R$\overline{3}$m spacegroup. The pattern from crystallographic information file of single crystal Li$_{0.68}$CoO$_2$ (pink) is shown for comparison.[32]
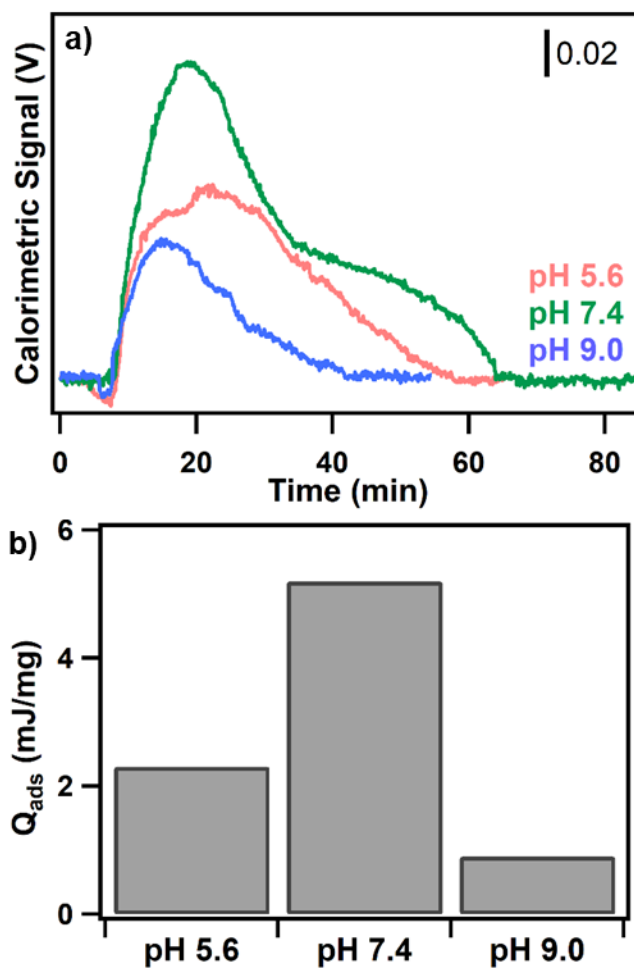
Figure 3.2. a) Calorimetric signals for phosphate interaction with $LiCoO_2$ at pH 5.6 (pink trace), 7.4 (green trace), and 9.0 (blue trace) as a function of time. An increase in voltage resulting in a positive peak corresponds to a release of energy and hence an exothermic reaction. b) heats of adsorption (Q_{ads}) obtained by converting the calorimetric peak area to energy units and normalizing by sample mass.
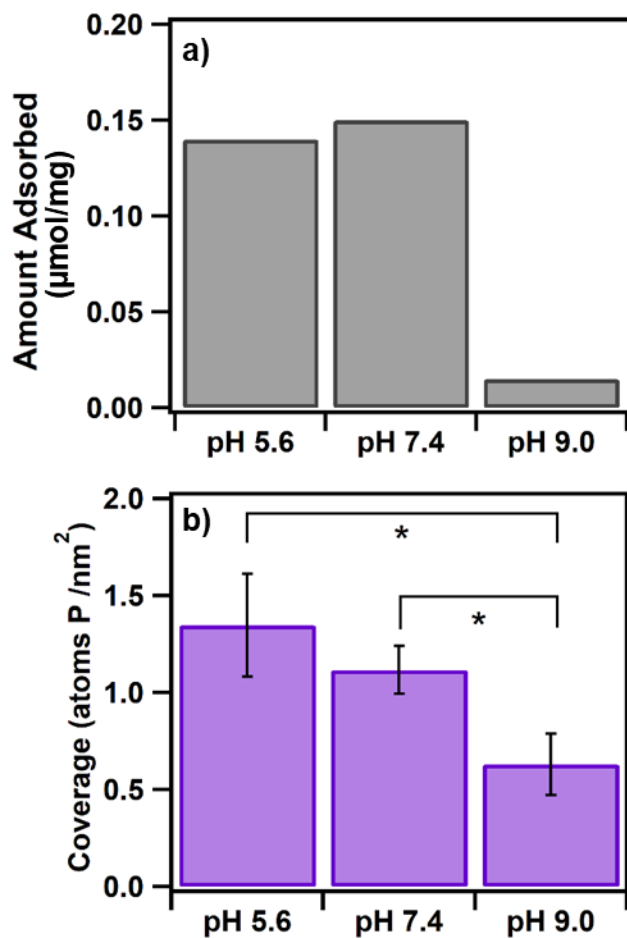
Figure 3.3. Phosphate coverage on LiCoO$_2$ as a function of pH. a) phosphate coverage in units of µmol/mg LiCoO$_2$, as determined from ion chromatography following calorimetry. b) phosphate coverage in atoms P/nm^2 as determined from XPS. Asterisks indicate significant difference between means as based on a single-factor ANOVA test.
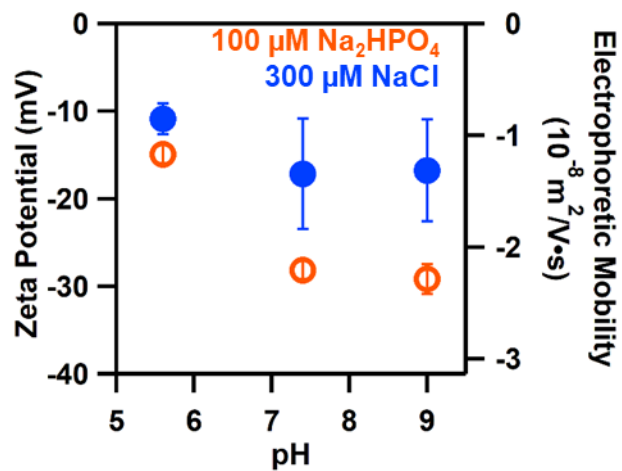
Figure 3.4. apparent zeta potential (left axis) and electrophoretic mobilities (right axis) of LiCoO$_2$ in 100 μM Na$_2$HPO$_4$ (orange, open markers) and comparable ionic strength non-interacting salt, 300 μM NaCl (blue, closed markers) as a function of pH.
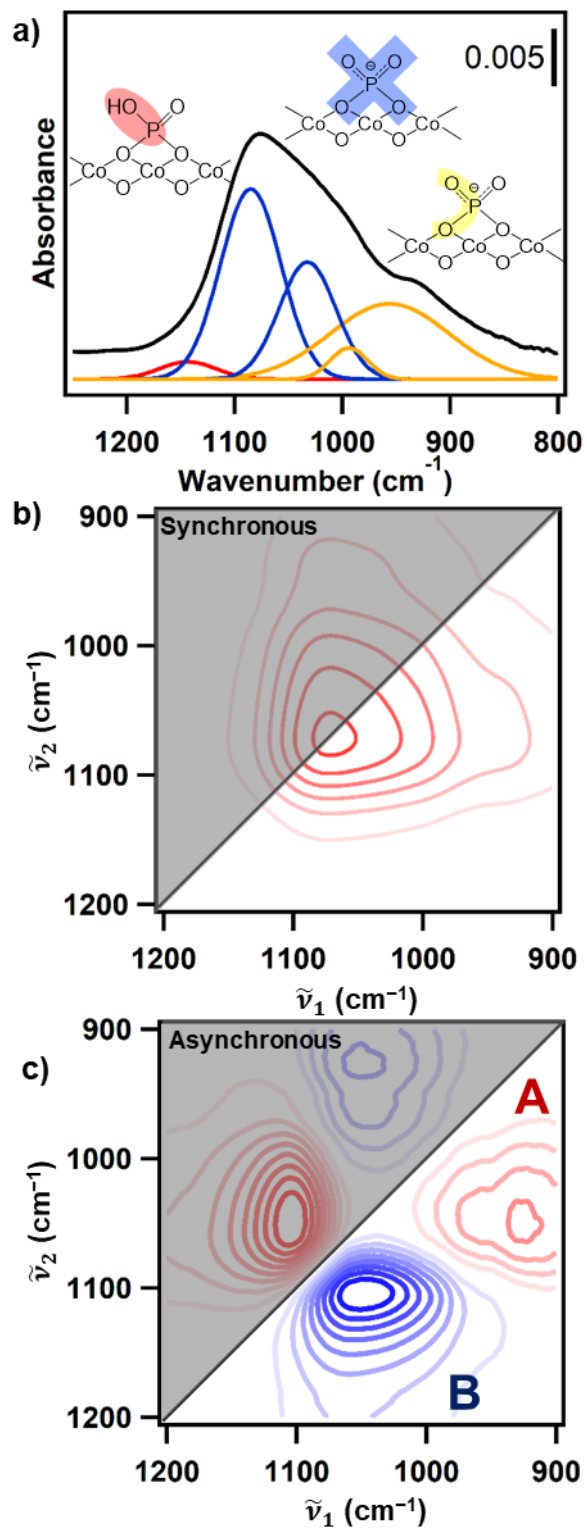
Figure 3.5. a) ATR-FTIR spectrum of phosphate on LiCoO₂, indicating the vibrational modes in each region. b) synchronous 2D correlation plot for phosphate exposure to LiCoO₂. c)

asynchronous 2D correlation plot for phosphate exposure to $LiCoO_2$. Positive contours are red,

negative contours are blue, with darker shades indicating larger values.
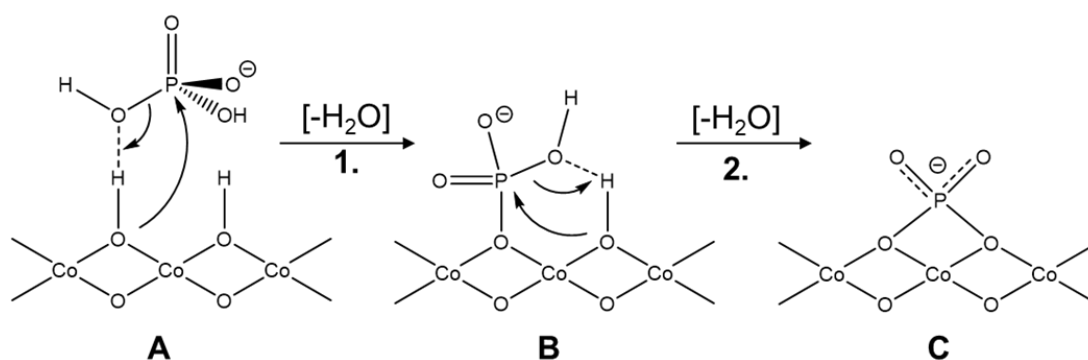
Scheme 3.1. Proposed mechanism of phosphate interaction with LiCoO$_2$ at pH 7.4. A) H$_2$PO$_4^-$ forms a hydrogen bond to a protonated oxygen on the surface of LiCoO$_2$. A subsequent phosphoryl transfer reaction releases a water molecule and a covalent bond between phosphate and the surface is formed. B) a second hydrogen bond between the surface CoHPO$_4^-$ and another protonated group on the surface forms, and a second phosphoryl transfer reaction releases a second water molecule. C) the final structure, a bidentate, deprotonated phosphate coordinated to the surface of LiCoO$_2$.

3.6 References.

1.   Murphy, C. J.; Vartanian, A. M.; Geiger, F. M.; Hamers, R. J.; Pedersen, J.; Cui, Q.; Haynes, C. L.; Carlson, E. E.; Hernandez, R.; Klaper, R. D.; Orr, G.; Rosenzweig, Z. e., Biological Responses to Engineered Nanomaterials: Needs for the Next Decade. *ACS Cent. Sci.* **2015,** *1* (3), 117-123.

2.   Grassian, V. H.; Haes, A. J.; Mudunkotuwa, I. A.; Demokritou, P.; Kane, A. B.; Murphy, C. J.; Hutchison, J. E.; Isaacs, J. A.; Jun, Y.-S.; Karn, B.; Khondaker, S. I.; Larsen, S. C.; Lau, B. L. T.; Pettibone, J. M.; Sadik, O. A.; Saleh, N. B.; Teague, C., NanoEHS – defining fundamental science needs: no easy feat when the simple itself is complex. *Environ. Sci.: Nano* **2016,** *3*, 15-27.

3.   Keller, A. A.; McFerran, S.; Lazareva, A.; Suh, S., Global life cycle releases of engineered nanomaterials. *J Nanopart Res* **2013,** *15*, 1692-1709.

4.   Lowry, G. V.; Gregory, K. B.; Apte, S. C.; Lead, J. R., Transformations of Nanomaterials in the Environment. *Environ. Sci. Technol.* **2012,** *46*, 6893-6899.

5.   Mensch, A. C.; Hernandez, R. T.; Kuether, J. E.; Torelli, M. D.; Feng, Z. V.; Hamers, R. J.; Pedersen, J. A., Natural Organic Matter Concentration Impacts the Interaction of Functionalized Diamond Nanoparticles with Model and Actual Bacterial Membranes. *Environ. Sci. Technol.* **2017,** *51* (19), 11075-11084.

6.   Laudadio, E. D.; Bennett, J. W.; Green, C. M.; Mason, S. E.; Hamers, R. J., Impact of Phosphate Adsorption on Complex Cobalt Oxide Nanoparticle Dispersibility in Aqueous Media. *Environ. Sci. Technol.* **2018,** *52*, 10186-10195.

7.   Ho, T. A.; Greathouse, J. A.; Lee, A. S.; Criscenti, L. J., Enhanced Ion Adsorption on Mineral Nanoparticles. *Langmuir* **2018,** *34*, 5926-5934.

8.   Ho, T. A.; Criscenti, L. J.; Greathouse, J. A., Revealing Transition States during the Hydration of Clay Minerals. *J. Phys. Chem. Lett.* **2019,** *10*, 3704-3709.

9.   Ellingsen, L. A.; Hung, C. R.; Majeau-Bettez, G.; Singh, B.; Chen, Z.; Whittingham, M. S.; Stromman, A. H., Nanotechnology for environmentally sustainable electromobility. *Nat Nanotechnol* **2016,** *11* (12), 1039-1051.

10.   Whittingham, M. S., Lithium Batteries and Cathode Materials. *Chem. Rev.* **2004,** *104*, 4271-4301.

11.   Notter, D. A.; Gauch, M.; R., W.; Wagner, P.; Stamp, A.; Zah, R.; Althaus, H.-J., Contribution of Li-Ion Batteries to the Environmental Impact of Electric Vehicles. *Environ. Sci. Technol.* **2010,** *44*, 6550-6556.

12.   Dunn, J. B.; Gaines, L.; Kelly, J. C.; James, C.; Gallagher, K. G., The significance of Li-ion batteries in electric vehicle life-cycle energy and emissions and recycling's role in its reduction. *Energy Environ. Sci.* **2015,** *8* (1), 158-168.

13.   Kanan, M. W.; Surendranath, Y.; Nocera, D. G., Cobalt–phosphate oxygen-evolving compound. *Chemical Society Reviews* **2009,** *38*, 109-114.

14.   Xiao, X.; Liu, X.; Wang, L.; Zhao, H.; Hu, Z.; He, X.; Li, Y., LiCoO2 Nanoplates with Exposed (001) Planes and High Rate Capability for Lithium-Ion Batteries. *Nano. Res.* **2012,** *5* (6), 395-401.

15.   Lu, Z. Y.; Wang, H. T.; Kong, D. S.; Yan, K.; Hsu, P. C.; Zheng, G. Y.; Yao, H. B.; Liang, Z.; Sun, X. M.; Cui, Y., Electrochemical tuning of layered lithium transition metal oxides for improvement of oxygen evolution reaction. *Nat. Commun.* **2014,** *5*, 7.

16.   Dogangun, M.; Hang, M. N.; Machesky, J.; McGeachy, A. C.; Dalchand, N.; Hamers, R. J.; Geiger, F. M., Evidence for Considerable Metal Cation Concentrations from Lithium

Intercalation Compounds in the Nano−Bio Interface Gap. *J. Phys. Chem. C* **2017,** *121*, 27473-27482.

17.   Dogangun, M.; Hang, M. N.; Troiano, J. M.; McGeachy, A. C.; Melby, E. S.; Pedersen, J. A.; Hamers, R. J.; Geiger, F. M., Alteration of Membrane Compositional Asymmetry by LiCoO2 Nanosheets. *ACS Nano* **2015,** *9* (9), 8755-8765.

18.   Bozich, J.; Hang, M.; Hamers, R.; Klaper, R., Core Chemistry Influences the Toxicity of Multicomponent Metal Oxide Nanomaterials, Lithium Nickel Manganese Cobalt Oxide, and Lithium Cobalt Oxide to *Daphnia magna*. *Environmental Toxicology and Chemistry* **2017,** *36* (9), 2493-2592.

19.   Gunsolus, I. L.; Hang, M. N.; Hudson-Smith, N. V.; Buchman, J. T.; Bennett, J. W.; Conroy, D.; Mason, S. E.; Hamers, R. J.; Haynes, C. L., Influence of nickel manganese cobalt oxide nanoparticle composition on toxicity toward Shewanella oneidensis MR-1: redesigning for reduced biological impact. *Environ. Sci.: Nano* **2017,** *4* (3), 636-646.

20.   Hang, M. N.; Gunsolus, I. L.; Wayland, H.; Melby, E. S.; Mensch, A. C.; Hurley, K. R.; Pedersen, J. A.; Haynes, C. L.; Hamers, R. J., Impact of Nanoscale Lithium Nickel Manganese Cobalt Oxide (NMC) on the Bacterium Shewanella oneidensis MR-1. *Chemistry of Materials* **2016,** *28*, 1092-1100.

21.   Li, M.; Liu, J.; Xu, Y.; Qian, G., Phosphate adsorption on metal oxides and metal hydroxides: A comparative review. *Environ. Rev.* **2016,** *24*, 319-332.

22.   Borggaard, O. K., The influence of iron oxides on phosphate adsorption by soil. *Journal of Soil Science* **1983,** *34*, 333-341.

23.   Ler, A.; Stanforth, R., Evidence for Surface Precipitation of Phosphate on Goethite. *Environ. Sci. Technol.* **2003,** *37*.

24.   Appel, C.; Rhue, D.; Kabengi, N.; Harris, W., Calorimetric Investigation of the Nature of Sulfate and Phosphate Sorption on Amorphous Aluminum Hydroxide. *Soil Science* **2013,** *178* (4), 180-188.

25.   Kabengi, N. J.; Chrysochoou, M.; Bompoti, N.; Kubicki, J. D., An integrated flow microcalorimetry, infrared spectroscopy and density functional theory approach to the study of chromate complexation on hematite and ferrihdyrite. *Chemical Geology* **2017,** *464*, 23-33.

26.   Kabengi, N. J.; Daroub, S. H.; Rhue, R. D., Energetics of arsenate sorption on amorphous aluminum hydroxides studied using flow adsorption calorimetry. *Journal of Colloid and Interface Science* **2006,** *297*, 86-94.

27.   Kabengi, N. J.; Rhue, R. D.; Daroub, S. H., USING FLOW CALORIMETRY TO DETERMINE THE MOLAR HEATS OF CATION AND ANION EXCHANGE AND THE POINT OF ZERO NET CHARGE ON AMORPHOUS ALUMINUM HYDROXIDES. *Soil Science* **2006,** *171* (1), 13-20.

28.   Namayandeh, A.; Kabengi, N., Calorimetric study of the influence of aluminum substitution in ferrihydrite on sulfate adsorption and reversibility. *Journal of Colloid and Interface Science* **2019,** *540*, 20-29.

29.   Rhue, R. D.; Appel, C.; Kabengi, N., MEASURING SURFACE CHEMICAL PROPERTIES OF SOIL USING FLOW CALORIMETRY. *Soil Science* **2002,** *167* (12), 782-790.

30.   Sabur, M. A.; Goldberg, S.; Gale, A.; Kabengi, N.; Al-Abadleh, H. A., Temperature-Dependent Infrared and Calorimetric Studies on Arsenicals Adsorption from Solution to Hematite Nanoparticles. *Langmuir* **2015,** *31*, 2749-2860.

31.   Kubicki, J. D.; Paul, K. W.; Kabalan, L.; Zhu, Q.; Mrozik, M. K.; Aryanpour, M.; Pierre-Louis, A.-M.; Strongin, D. R., ATR−FTIR and Density Functional Theory Study of the Structures, Energetics, and Vibrational Spectra of Phosphate Adsorbed onto Goethite. *Langmuir* **2012,** *28*, 14573-14587.

32.   Baker, L. A.; Brezonik, P. L.; Edgerton, E. S., Sources and Sinks of Ions in a Soft Water, Acidic Lake in Florida. *Water Resources Research* **1986,** *22* (5), 715-722.

33.   Kenoyer, G. J.; Anderson, M. P., GROUNDWATER'S DYNAMIC ROLE IN REGULATING ACIDITY AND CHEMISTRY IN A PRECIPITATION-DOMINATED LAKE *Journal of Hydrology* **1989,** *109*, 287-306.

34.   Chen, H.; Grey, C. P., Molten Salt Synthesis and High Rate Performance of the ''Desert-Rose'' form of LiCoO2**. *Advanced Materials* **2008,** *20*, 2206-2210.

35.   Takahashi, Y. K., N.; Dokko, K.; Nishizawa, M.; Akimoto, J.; Uchida, I., Structure and electron density analysis of electrochemically and chemically delithiated Li Co O2 single crystals. *Journal of Solid State Chemistry* **2007,** *180*, 313-321.

36.   Noda, I.; Ozaki, Y., *Two-dimensional Correlation Spectroscopy – Applications in Vibrational and Optical Spectroscopy*. John Wiley & Sons, Ltd: 2004.

37.   Chen, W.; Qian, C.; Liu, X.-Y.; Yu, H.-Q., Two-Dimensional Correlation Spectroscopic Analysis on the Interaction between Humic Acids and TiO2 Nanoparticles. *Environ. Sci. Technol.* **2014,** *48*, 1119-11126.

38.   Wu, H.; Gonzalez-Pech, N. I.; Grassian, V. H., Displacement reactions between environmentally and biologically relevant ligands on TiO2 nanoparticles: insights into the aging of nanoparticles in the environment. *Environ. Sci.: Nano* **2019,** *6*, 489-504

39.   Powell, C. J.; Jablonski, A. *NIST Electron Effective-Attenuation-Length Database*, version 1.3; National Institute of Standards and Technology: Gaithersburg, MD, 2011.

40.   Tanuma, S.; Powell, C. J.; Penn, D. R., Calculation of Electron Inelastic Mean Free Paths (IMFPs) VII. Reliability of the TPP-2M IMFP Predictive Equation. *Surf. Interface Anal.* **2003,** *35*, 268-275.

41.   Wojdyr, M., Fityk: a general-purpose peak fitting program. *J. Appl. Cryst.* **2010,** *43*, 1126-1128.

42.   Maiyalagan, T.; Jarvis, K. A.; Therese, S.; Ferreira, P. J.; Manthiram, A., Spinel-type lithium cobalt oxide as a bifunctional electrocatalyst for the oxygen evolution and oxygen reduction reactions. *Nat. Commun.* **2014,** *5*, 1-8.

43.   Tang, W.; Liu, L. L.; Tian, S.; Li, L.; Yue, Y. B.; Wu, Y. P.; Guan, S. Y.; Zhu, K., Nano-LiCoO2 as cathode material of large capacity and high rate capability for aqueous rechargeable lithium batteries. *Electrochem. Commun.* **2010,** *12* (11), 1524-1526.

44.   Fernandez-Rodriguez, J. M.; Hernan, L.; Morales, J.; Tirado, J. L., Low-temperature hydrothermal transformations of LiCoO2 and HCoO2. *Mat. Res. Bull* **1988,** *23*, 899-904.

45.   Huang, X.; Bennett, J. W.; Hang, M. N.; Laudadio, E. D.; Hamers, R. J.; Mason, S. E., Ab Initio Atomistic Thermodynamics Study of the (001) Surface of LiCoO2 in a Water Environment and Implications for Reactivity under Ambient Conditions. *The Journal of Physical Chemistry C* **2017,** *121* (9), 5069-5080.

46.   Lowry, G. V.; Hill, R. J.; Harper, S.; Rawle, A. F.; Ogilvie Hendersen, C.; Klaessig, F.; Nobbmann, U.; Sayre, P.; Rumble, J., Guidance to improve the scientific value of zetapotential measurements in nanoEHS. *Environ. Sci.: Nano* **2016,** *3*, 953-965.

47.   Swan, J. W.; Furst, E. M., A simpler expression for Henry's function describing the electrophoretic mobility of spherical colloids. *Journal of Colloid and Interface Science* **2012,** *388*, 92-94.

48.   Bhattacharjee, S., DLS and zeta potential – What they are and what they are not? *Journal of Controlled Release* **2016,** *235*, 337-351.

49.   Patel, V. R.; Agrawal, Y. K., Nanosuspension: An approach to enhance solubility of drugs. *J. Adv. Pharm. Tech. Res.* **2011,** *2* (2), 81-87.

50.   Gong, W., A real time in situ ATR-FTIR spectroscopic study of linear phosphate adsorption on titania surfaces. *International Journal of Mineral Processing* **2001,** *63*, 147-165.

51.   Tejedor-Tejedor, M. I.; Anderson, M. A., Protonation of Phosphate on the Surface of Goethite As Studied by CIR-FTIR and Electrophoretic Mobility. *Langmuir* **1990,** *6* (3), 602-611.

52.   Connor, P. A.; McQuillan, A. J., Phosphate Adsorption onto TiO2 from Aqueous Solutions: An in Situ Internal Reflection Infrared Spectroscopic Study. *Langmuir* **1999,** *15*, 2916-2921.

53.   Goldberg, S.; Sposito, G., On the mechanism of specific phosphate adsorption by hydroxylated mineral surfaces: A review. *Commun. In Soil sci. Plant Anal.* **1985,** *16* (8), 801-821.

54.   Nord, A. G., The structure of cobalt(II) tetrametaphosphate, Co2 P4 O12. *Crystal Structure Communications* **1982,** *11*, 1467-1474.

55.   Nord, A. G.; Stefanidis, T., Structure refinements of Co3(PO4)2. A note on the reliability of powder diffraction studies. *Acta Chemica Scandinavica, Series A* **1983,** *37*, 715-721.

56.   Krishnamachari, N.; Calvo, C., The Crystal Structure of Cobalt Diphosphate. *Acta Cryst.* **1972,** *B28*, 2883-2891.

57.   Alcántara, R.; Lavela, P.; Tirado, J. L.; Zhecheva, E.; Stoyanova, R., Recent advances in the study of layered lithium transition metal oxides and their application as intercalation electrodes. *Journal of Solid State Electrochemistry* **1999,** *3* (3), 121-134.

58.   Zhecheva, E.; Stayanova, R., Li1-x-yHyCoO2: Metastable Layered Phases Obtained by Acid Digestion of LiCoO2(O3). *Journal of Solid State Chemistry* **1994,** *109* (1), 47-52.

Chapter 4. The Influence of Organic Acids on Lithium Cobalt Oxide Nanoparticle Dissolution and Interaction with Phosphate

Elizabeth D. Laudadio, Robert J. Hamers

All of the experiments, data acquisition and analysis, preparation and revision of this chapter were done by Elizabeth D. Laudadio under the advisement of Robert J. Hamers.

4.1 Introduction.

Lithium cobalt oxide ($LiCoO_2$) is a lithium intercalation metal oxide that is widely used in lithium ion battery cathodes, energy storage devices and catalysis applications.[1-4] As the battery industry pushes towards the nanoscale,[5-6] there is a growing concern regarding the safety of these nanomaterials.[7-11] In particular, the mass of cathode materials in electric vehicles can be on the order of 40 kilograms per car.[12] As the market for electric vehicles continues to increase, the likelihood of accidental release of these materials into the environment increases as well, especially considering the lack of a formal infrastructure and economic incentive for recycling.[13-14]

Upon release into the environment, the reactions at the interface between a nanoparticle surface and aqueous environmental systems will dictate the fate, transport and impact of these materials. We have shown previously that lithium cobalt oxide nanoparticles interact strongly with the phosphate oxyanion.[15-16] Phosphate adsorbs irreversibly to the surface of these particles through a thermodynamically favorable process at environmentally relevant concentrations and pHs. The impact of this adsorption is enhanced colloidal stability as a result of enhanced electrostatic repulsion between particles, owing to the negative surface charge that the deprotonated phosphate structure imparts on the particle. While this discovery sheds some light on

the potential transformations of nanomaterials in aqueous environments, the contents of actual environmental waters such as wastewater treatment plants, natural waters, aquatic sediments and soils are more complex than single component solutions. Natural organic matter (NOM) in particular is an important competitor for interaction with nanoparticle surfaces to consider. NOM is one of the most abundant chemical species in environmental waters, being present at concentrations varying from tens of mg/L to hundreds of mg/L of organic carbon. NOM exists of alkyl and aromatic carbons with a variety of functional groups including phenolics, hydroxyls, carboxylic acids and quinones.[17] NOM has been shown to bind to nanomaterials, which can impact their toxicity to model organisms.[17] It has been shown that for naturally occurring metal oxides and hydroxides, almost complete surface coverage of organic material can be expected at natural pH levels, with adsorption decreasing as a function of increasing pH.[18] Interaction of nanomaterials and NOM has shown to lead to acquired coronas, increased mobility[18] or aggregation of nanoparticles,[19] or change in surface charge, with these interactions dependent on nanoparticle coatings and surface charge, as well as specific NOM properties and concentrations.

To draw more chemically specific conclusions from our studies on the influence of organic acids on $LiCoO_2$, we chose to use a variety of NOM surrogate molecules as opposed to full NOM. Specifically, we investigated the role of hydroxy-substituted benzoic acids, and the impact of the proximity of the alcohol group to the carboxylic acid group on how strongly and competitively the molecule interacts with $LiCoO_2$ both when exposed alone and when co-exposed with equal concentrations of phosphate. Previous studies have shown that the presence of lactate ion significantly enhances dissolution of complex metal oxide nanomaterials,[10-11] which is supported by DFT modeling of the complexation of released metal cations with lactate. The role that organic acids play in $LiCoO_2$ dissolution also holds importance for the recycling of these materials, where

greener recycling methods are being investigated by replacing strong acids with organic molecules.[20-25]

In the following studies, we investigate how the presence of organic acids in a phosphate solution impacted phosphate coverage on $LiCoO_2$, as well as dissolution of cobalt from the material. We also used attenuated total reflectance – FTIR (ATR-FTIR) to assess if and how the molecules bound to $LiCoO_2$ surfaces. While we expected these studies to yield comparable information on how adsorption to and dissolution from $LiCoO_2$ was functional-group specific, the findings were less linear than hypothesized. We found that lactic acid was the only acid studied that led to decreased phosphate adsorption when co-exposed, as characterized via X-ray photoelectron spectroscopy (XPS). XPS results did not support organic acid binding to LCO surfaces, though ATR-FTIR results suggest otherwise. We found that lactic acid has more of an impact on cobalt release from $LiCoO_2$ than salicylic acid, and these studies will be expanded upon with the other molecules in the future.

4.2 Materials/Methods.

4.2.1. Lithium cobalt oxide nanoparticle synthesis and characterization.

We synthesized sheet-like nanoparticles of Li_xCoO_2 as described previously.[15-16, 26] Only a brief description of the synthetic process is described here. We synthesized a $Co(OH)_2$ precursor by dropwise addition of 1 M $Co(NO_3)_2 \cdot 6H_2O$ to 0.1 M LiOH, ensuring a [OH] 5% stoichiometric excess for $Co^{2+} + 2OH^- \rightarrow Co(OH)_2$).[26] The precipitate was isolated by centrifuging into a pellet and decanting the supernatant. The pellet was then washed by redispersion in water, centrifugation and removal of supernatant a total of three times. We dried the product in a vacuum oven at 30 °C overnight. To convert $Co(OH)_2$ to Li_xCoO_2, the $Co(OH)_2$ precursor was added to a molten salt flux of $LiNO_3$:LiOH in a 6:4 molar ratio. The flux was prepared by heating the mixture at 200 °C in a

polytetrafluoroethylene container with magnetic stirring. After the precursor had reacted in the flux for 30 min, we quenched the reaction with water and washed/isolated the precipitate through four cycles as described above. The product was then dried in a vacuum oven at 30 °C overnight.

4.2.2. Chemical characterization of Li_xCoO_2 nanoparticles.

We obtained powder x-ray diffraction (XRD) patterns of the Li_xCoO_2 nanoparticles with a Bruker D8 Advance powder diffractometer, equipped with a Cu Kα source and a Lynxeye detector. To prepare powders for analysis, concentrated dispersions of $LiCoO_2$ powders in isopropyl alcohol were formed through ultrasonication in a cup sonicator. The dispersion was drop-cast onto a zero diffraction plate and allowed to dry. The powder XRD pattern was acquired from 15 to 80 degrees 2θ using a step size of 0.20 ° and dwell time of 166 s at each point.

For morphology characterization with scanning electron microscopy (SEM), dilute dispersions of $LiCoO_2$ were prepared in methanol and drop-cast onto low-resistivity (<0.1 Ω•cm⁻¹) boron-doped silicon wafers. Micrographs were acquired with a Leo Supra55 VP SEM at 3 kV electron energy using a secondary electron detector.

4.2.3. Quantification of molecular adsorption with X-ray photoelectron spectroscopy (XPS).

To quantify the adsorption of phosphate and organic acids onto $LiCoO_2$, we used XPS measurements of electron emission from the P(2p), C(1s) and Co(2p) levels. We prepared samples for XPS by suspending 5 mg LCO nanoparticles in 50 mL of a 1 mM Na_2HPO_4 or a solution containing 1 mM Na_2HPO_4 and 1 mM of an organic acid, adjusted to a pH of 7.4 by addition of μL volumes of either 1 M NaOH or 1 M HCl as needed. We isolated the particles through centrifugation (4696×g, 5 min) after the exposure had taken place for one hour. After isolation, the supernatant was discarded, the pellet was redispersed in water, and the particles were isolated

again through centrifugation (14,000×g) for 1 minute. The pellet was then dried under vacuum overnight. We pressed the dried particles into indium foil on a copper foil backing to ensure the sample was of homogenous flatness and thickness and could make good electrical contact with the sample holder. XPS spectra were measured using either a Thermo Fisher Scientific K-alpha XPS using at a 45° photoelectron takeoff angle or a PHI VersaProbe III K-alpha XPS, measuring the Li (1s), Co(2p), O(1s), Na(1s), C(1s) and P(2p) peaks. XPS spectra were fit using CasaXPS software.[27] Co(2p) and P(2p) peak areas were used for quantitative analysis of surface coverage (Equation 1). The inelastic mean free path of Co was estimated at 1.9 nm using the NIST Effective Attenuation Length Database[28] via the TPP-2M equation.[28-29] We compared the coverage of P and C with and without the organic acids present.

$$Coverage\ P = \frac{Area_{P,2p\ or\ C,1s}}{SF_{P,2p\ or\ C,1s}} * \left[\frac{SF_{Co,2p3}}{A_{Co,2p3}} + \frac{SF_{Co,2p1}}{A_{Co,2p1}}\right] * \frac{Scans_{Co,2p}}{Scans_{P,2p\ or\ C,1s}} * \rho_{Co,LiCoO2} * \lambda_{Co,LiCoO2} * \cos(45°)$$

Equation 1. Absolute coverage determination via quantitative XPS analysis. A = peak area, SF = atomic sensitivity factor ($SF_{Co,2p}$ = 18.23529 for Thermo instrument, $SF_{Co,2p3/2}$ = 2.113 for Phi instrument, $SF_{Co,2p1/2}$ = 1.056 for Phi instrument, $SF_{P,2p}$=1.352941 for Thermo instrument, $SF_{P,2p}$= 0.525 for Phi instrument, $SF_{C,1s}$ = 1 for Thermo instrument, $SF_{C,1s}$ = 0.314 for Phi instrument), ρ= density of cobalt in $LiCoO_2$ (30 atoms/nm^3), λ = inelastic mean free path of Co electron emitted from $LiCoO_2$ (1.9 nm, calculated from the NIST database)[28], θ= Angle of the analyzer to the surface normal (45° for both instruments used here). Scans refers to the number of scans that were averaged to achieve the total peak area ($Scans_{Co,2p}$ = 10, $Scans_{P,2p}$ = 100, $Scans_{C,1s}$ = 30).

Representative spectra are shown in Figure A.4.1. Measurements were taken at three spots on each sample, and phosphorus and carbon coverages in atoms / nm^2 were calculated from Equation 1. A two-sided t-test assuming unequal variance was applied to the data to determine

values of significance between the organic acid containing and organic acid lacking samples. The phosphorus and carbon coverages for each dataset were then normalized to the phosphorus and carbon coverages for the organic acid lacking solutions, to compare the change in normalized coverage. The raw coverage values are shown in Figure A.4.2.

4.2.4. Preparation of LiCoO$_2$ layers for attenuated total reflectance – FTIR (ATR-FTIR).

Thin layers of LiCoO$_2$ were prepared by spin-coating LiCoO$_2$ suspensions onto a zinc selenide (ZnSe) internal reflection element (IRE) as reported previously.[15-16] Briefly, we prepared LiCoO$_2$suspensions of 1000 mg/L in methanol which were ultrasonicated for 1 hr in a cup ultrasonicator with cooling water (10 s on, 10 s off for 30 min total sonication time). ZnSe IREs were cleaned before use by rinsing with water followed by methanol, dried with N$_2$, and exposed to UV light from a low-pressure Hg grid lamp (UV Products) in air for at least 10 min before use. We then spin-coated the LiCoO$_2$ suspension onto the clean ZnSe IREs (80 µL per spin, 1000 rpm, 4 s per spin). The layer was then stabilized by heating in a box furnace at 400 $^{\circ}$C for 5 min.

4.2.5. ATR-FTIR studies of organic acid adsorption to LCO surfaces.

ATR-FTIR spectra were acquired using the previously described LiCoO$_2$-coated ZnSe IREs assembled in a flow cell (Specac) using a Bruker Vertex 70 FTIR spectrometer. Spectra were acquired at 4 cm^{-1} resolution, averaging 500 scans per spectrum. Each experiment was performed at pH 7.0. In each experiment, at reference spectrum was obtained after flowing 1 mL of pH-adjusted water over the LiCoO$_2$-coated ZnSe at 0.5 mL/min. The analyte solution of interest (10 mM concentrations of corresponding organic acid solution) was then flowed at a rate of 0.5 mL/min while acquiring repeated spectra (approximately 2 minutes per spectrum) for a total duration of 1 hr. We then flowed water through the cell at 0.5 mL/min while taking repeated spectra

for 1 h, in order to reveal the vibrational modes of the analyte remaining on the surface after rinsing away any excess in solution or weakly bound to the surface. All spectra shown here are presented as absorption spectra.

4.2.6. Procedure for pre-dosing LiCoO₂ nanoparticles with phosphate.

The procedure for pre-dosing $LiCoO_2$ nanoparticles with phosphate is identical to the procedure used in the XPS quantification of coverage experiments described above. As an ionic strength control, $LiCoO_2$ nanoparticles were exposed to 3 mM NaCl, pH 7.4 in parallel with exposure to 1 mM Na_2HPO_4, pH 7.4, and used as a control in subsequent dissolution experiments.

4.2.7. Dissolution of LiCoO₂ nanoparticles.

20 mg/L suspensions of $LiCoO_2$ nanoparticles were prepared by addition of 0.5 mg particles to 25 mL of the analyte solution of interest. Suspensions were placed on a shaker operating at 200 rpm at 28 °C for 3 hours. The samples were the centrifuged to crash out the nanoparticles via centrifugation at 14,000 x g for 20 minutes. The supernatant was removed from the samples and passed through a 0.1 μm filter. The samples were spiked to 2% HNO_3 through removal of 280 μL sample (of 10 mL) and addition of 280 μL high purity 70% HNO_3 and analyzed for Co and Li ion concentration using inductively coupled plasma – optical emission spectroscopy (ICP-OES). The concentrations determined from ICP-OES analysis were then adjusted to take into consideration the dilution from the acidification step. The data presented are the averages and standard deviations from three experimental replicates. For each data set a two-sided t-test assuming unequal variance was applied to determine values of significance.

4.2.8. Justification for model molecules used in this study.

Figure 4.1 shows the structure, name, and abbreviation for the molecules used in this study. This suite of molecules was chosen to probe several specific variables. Lactic acid (LA) and

salicylic acid (SA) were chosen to probe the effect of hydrophobicity on the impact to $LiCoO_2$. Benzoic acid (BA) and SA allow for the study of the role of the hydroxyl group adjacent to the carboxylic acid in interacting with $LiCoO_2$. SA, 3-hydroxybenzoic acid (3HB) and 4-hydroxybenzoic acid (4HB) were chosen to examine the role of the location of the hydroxyl group on interaction with $LiCoO_2$. The pKas of the carboxylic acids of all of these molecules is below pH 7, which is the pH used for these studies, and therefore the carboxylic acids of all of these molecules are expected to be deprotonated in these experiments. Therefore, while the names of the acids are being used, the molecules being introduced in each experiment are the conjugate bases.

4.3. Results and Discussion.

4.3.1. Nanoparticle synthesis and characterization.

Figure 4.2a shows a representative scanning electron micrograph of the as-synthesized $LiCoO_2$ nanoparticles. The nanoparticles have a sheet-like morphology, as reported previously, with diameters ranging from 20-50 nm and thicknesses around 5 nm.[15-16] Figure 4.2b shows the powder XRD pattern collected from the nanoparticles (blue trace) compared to a reference pattern from the crystallography open database of single crystal $LiCoO_2$ (gray trace).[30] The pattern collected from the nanomaterials can be indexed to the $R\bar{3}m$ space group, which is the delafossite (α-$NaFeO_2$) crystal structure.[4, 31] This layered crystal structure is consistent with what is intentionally produced for lithium ion batteries, as the lithium ions are intercalated between layers of corner-sharing CoO_6 octahedra,[32] which allow for high electrical conductivity.[33] Our collected XRD pattern is indexed to this space group, with the indices denoted above specific reflections. Full separation of the (018) and (110) peaks is not observed, which may suggest the presence of some residual spinel phases.[34] However, it is also possible that the inability to resolve these peaks is an artifact of the peak broadening that occurs when acquiring XRD patterns of nanoparticles.

While in the pristine material, the surface termination is Li$^+$, when in water, the surface lithium quickly dissociate and are replaced with protons, as has been observed both experimentally[16, 35] and computationally.[32] It is therefore expected that in the subsequent studies in aqueous solution, the surface of the particles is hydroxylated instead of lithium terminated.

4.3.2. Presence of organic acids impact on phosphate adsorption.

We have previously studied the robust adsorption of phosphate to LiCoO$_2$. We have seen that phosphate binds irreversibly to the surface of the particles,[15] forming covalent bonds to the surface through condensation reactions.[16] We wanted to investigate how co-exposure of LiCoO$_2$ to both phosphate and organic acids, in equimolar concentrations, may impact phosphate adsorption. To do this, we used XPS to analyze the coverage of phosphate on LiCoO$_2$ that had either been exposed to phosphate alone, or phosphate in addition to one of the organic acids of interest. Representative XP spectra are shown in Figure A.4.1. In each experiment, the data for phosphate adsorption without the organic acid present was used to normalized the phosphorus coverage to these baseline values. The raw coverage values are shown in Figure A.4.2. The normalized phosphorus coverages are presented in Figure 4.3a. We found that the only organic acid that significantly impacted how much phosphate adsorbed to the nanoparticles was LA (p $\leq$ 0.01). While we anticipated that at least SA would have a similar effect that LA has, due to their similar functionalities, this was not seen. While we had hypothesized that the hydrophobicity of SA could assist in partitioning to the nanoparticle surface, the results suggest that the hydrophobicity of BA and the various hydroxy-substituted BA molecules may instead hinder the molecule's ability to interact with the surface of LiCoO$_2$.

In addition to monitoring the phosphorus region to determine phosphate coverage, we also monitored the carbon region. The carbon region was fit to three peaks, a representative spectra of

which are shown in Figure A.4.1, with the lowest binding energy peak representing adventitious carbon (284.8 eV), the middle peak representing alcohol/ether groups (~286 eV), and the higher energy peak representing carboxyl groups (~288.5 eV).[36] Coverage of carbon on $LiCoO_2$ was calculated via Equation 1 and normalized to the carbon coverage obtained from the control (phosphate only, no organic acid) samples, the results of which are shown in Figure 4.3b. In none of the experiments did we find that there was more carbon on the surface of the particles when exposed to the organic acids and phosphate versus phosphate alone. For the four acids that were not seen to impact phosphate adsorption, this is consistent with the molecules not interacting with the surface of $LiCoO_2$ through adsorption themselves, as also evidenced by the lack of an increase in the carbon on the surface. This also suggests that the impact LA has on phosphate adsorption is not because LA itself is binding to the particle surface, but instead is either mitigating phosphate adsorption or causing desorption through another route.

It is worth noting that the carbon coverage on each sample was >10 atoms/nm^2, even when the organic acids were not present, as shown in Figure A.4.2. There is a few atom/nm^2 carbon coverage on the particles after synthesis, as shown in Figure A.4.3, and additional carbon adsorption may come from particle aging during storage, adsorbed species from solution or plasticware during sample prep, adsorbed atmospheric species after sample prep, or a combination of these. Because the baseline carbon coverage is fairly high, it is possible that there are changes due to organic acid adsorption, but they are not resolvable from the baseline.

As the results of this section were inconclusive for many of the molecules studied, the rest of this chapter will focus on comparing the interaction of LA and SA with $LiCoO_2$ as they have comparable functionalities (carboxyl and alcohol group) with the structural change and increased hydrophobicity/steric hindrance of SA versus LA being the chosen variable to study.

4.3.3. ATR-FTIR analysis of organic acid binding.

To gain a better understanding of if, and how, these small molecules interact with the LiCoO$_2$ surface, we turned to ATR-FTIR. ATR-FTIR is a surface-sensitive, in situ spectroscopic technique that can be used to observe molecular vibrations of molecules on LiCoO$_2$. For these experiments, it was necessary to use higher concentrations of the organic acids than used in the previously discussed XPS experiments, 10 mM SA and 100 mM LA, accordingly. This is because the technique was not sensitive enough for us to observe vibrational modes at lower concentrations. Because of this, it is important to note that while binding is observed in these experiments, it is not necessarily in conflict with the XPS results, as lower concentrations were used in those experiments. Not seeing evidence of binding in XPS may suggest the species are weakly adsorbed, and are removed in the isolation/rinsing process of XPS sample preparation. Also, as mentioned above, because the carbon coverage baseline is relatively high it is possible that the changes to carbon coverage are present, but not able to be resolved. Future studies will be done to unify the concentrations used between these experiments to clarify some of these potential scenarios.

Figure 4.4a shows the spectra obtained during LA exposure (light blue trace, labeled "exposure") and after rinsing with water following exposure (dark blue trace, labeled "surface"). Rinsing the cell with water after LA exposure removes any non-interacting or loosely bound LA, revealing the spectral features specific to LA bound to the LiCoO$_2$ surface. The surface spectrum of LA on LiCoO$_2$ is magnified in Figure 4.4.b. The peaks in the spectrum of LA during the exposure can be assigned to various vibrational modes of the molecule through comparison with past reports[37-38], as shown in Table 1. After rinsing, the spectrum on the surface has more peaks than the LA in solution (11 versus 9), and many of the peaks that are the same are shifted, most to lower wavenumbers.

Previous studies of lactate adsorption to TiO_2[39-40], CdS[39], or iron oxide minerals[37, 41] suggest that lactate binding through the carboxyl group would cause an increase of the split between the the $\nu_{as}(COO^-)$ at ~1575 cm^{-1} and the $\nu_s(COO^-)$ at ~1410 cm^{-1} (Δ_{free} = 165 cm^{-1}). While a slight increase in the split is seen here (Δ_{ads}= 170 cm^{-1}), it is not nearly as large as other studies have reported. This may suggest either that lactate is not adsorbed through the carboxyl, or that it is electrostatically adsorbed, in which case we would not see shifts in peaks. Peak shifts are observed for several vibrations, ruling out the possibility of electrostatic adsorption, as well as the fact that both the molecule and the surface are negatively charged.

The ν(C-O) of the alcohol group at 1041 cm^{-1} in the free molecule shifts to higher wavenumbers, 1057 cm^{-1} on the surface of $LiCoO_2$.[39] The shift of the combination band of $\rho(CH_3)$ + νAL(C-O) at 1124 cm^{-1} in the free molecule to 1117 cm^{-1} on the surface of $LiCoO_2$ is also evidence of the OH group involvement in adsorption.[41] This has been considered an indication of the involvement of the OH group in chelation to the surface, however it is surprising to see this shift with no shift to the carboxyl peaks.

One possible explanation for the inconsistencies in our spectrum versus what has been reported previously has to do with the emergence of new peaks on the surface at 1225 and 1196 cm^{-1}. The lactate ion is already in the lowest possible symmetry group, and so the appearance of new peaks cannot be due to a lowering of symmetry. Instead, these peaks may indicate the degradation of lactate to smaller molecules on the $LiCoO_2$ surface. The oxidation of aliphatic alcohols on the surfaces of TiO_2 has been reported[42-43] as well as other Group IVB metal oxide catalysts,[43] and photocatalytically from CdS quantum dots.[39] Recent work in our group suggests that $LiCoO_2$ may be able to oxidize molecules as well.[44] The discrepancy in the number of peaks seen from the molecules themselves, and the peaks seen on the surface of $LiCoO_2$, may suggest

that a similar transformation is going on. Lactic acid degradation on the surface of TiO_2 has shown the emergence of infrared peaks that may explain some of the unassigned peaks in our spectra.[40] The peak at 1225 and 1196 cm^{-1} in our surface spectrum may be due to degradation products; while the peak at 1225 is unidentified, the one at 1196 cm^{-1} is consistent with a peak in the spectrum of the pyruvate ion.[40] Additionally, if molecular degradation is occurring, this may explain why we observe vibrational modes at the surface of $LiCoO_2$ but the position and number of modes is not consistent with lactate bound through previously elucidated geometries.

Figure 4.4c shows the spectra obtained during SA exposure (light green trace, labeled "exposure") and after rinsing with water following exposure (dark green trace, labeled "surface"). Rinsing the cell with water after SA exposure removes any non-interacting or loosely bound molecules, revealing the spectral features specific to SA bound to the $LiCoO_2$ surface. The surface spectrum of SA on $LiCoO_2$ is magnified in Figure 4.4.d. The peaks in the spectrum of SA during the exposure can be assigned to various vibrational modes of the molecule through comparison with past reports,[45-46] as shown in Table 2. The geometry of adsorbed SA on $LiCoO_2$ can be assigned as well based on published studies of adsorption to goethite that observe the same spectral changes.[45] Vibrational modes related to the C-C ring structure change location and intensity as a result of adsorption, as the π-electron density is impacted. The spacing between the $\nu_{as}(COO^-)$ and $\nu_s(COO^-)$ bands increases on the surface in our spectrum, which is consistent with the formation of a monodentate mononuclear complex, as has been reported for SA on goethite.[45]

There is more clear evidence from the ATR-FTIR study that SA binds to $LiCoO_2$ than the evidence for LA binding. However in other studies, it has been shown that lactate adsorbs more strongly than larger molecules due to steric hinderance.[38] Future work will be aimed at

corroborating this finding by adjusting the concentrations of adsorbates used in XPS experiments to gain comparable data between the two studies.

4.3.4. Cobalt release during phosphate adsorption.

We have shown previously that phosphate adsorbs strongly to $LiCoO_2$, forming an amorphous surface layer on the particles that is stable over long timescales.[15-16] We wanted to test if this phosphate coating would protect the particles from dissolution, and mitigate Co^{2+} release in the presence of organic acids. We know from previous studies[10-11, 47-48] as well as the field of battery cathode recycling[20-25] that organic acids can have a large impact on metal release from $LiCoO_2$ and related materials.

In order to test if phosphate coatings were protective against dissolution, we first needed to know how much Co^{2+} is released in the process of coating $LiCoO_2$ with phosphate. The coating procedure is the same as what has been done here and in past studies for preparing phosphate-coated $LiCoO_2$ samples for XPS.[15-16] As a control, particles in a solution of equal ionic strength NaCl were put through the "coating" procedure to assess the difference in Co^{2+} release in the presence of phosphate. Figure 4.5 shows the percent of Co^{2+} from the nanoparticles that is released and detected via ICP-MS after the coating procedure. While more Co^{2+} is released from $LiCoO_2$ in phosphate than in NaCl, the amount of Co^{2+} released in both cases is <0.1% of the total cobalt in the material. The raw concentrations of dissolved ions from this experiment is shown in Figure A.4.4. The concentration of dissolved ions when organic acids are present in the dissolution matrix is expected to be orders of magnitude larger than what is observed during the coating process by comparison to previous related studies,[10-11, 48] and therefore we felt it was appropriate to assume any differences in total Co^{2+} released observed in future studies could be accounted to the organic acids, and not the coating procedure.

4.3.5. Organic acid impact on cobalt release from phosphate coated particles.

We then exposed the phosphate-coated particles to either 10 mM LA or 10 mM SA, with equal ionic strength solutions of NaCl as a control in each case. The left two bars of Figure 4.6 shows the concentration of Co^{2+} released from either uncoated (blue outline, blue fill) or P-coated (orange outline, blue fill) $LiCoO_2$ in the presence of LA. There is no statistical significance between the concentration of Co^{2+} released from uncoated or P-coated $LiCoO_2$ in the presence of LA. The right two bars of Figure 4.6 show the concentrations of Co^{2+} released from uncoated (blue outline, green fill) or P-coated (orange outline, green fill) $LiCoO_2$ in the presence of SA. Similar to the LA experiments, no statistical significance between the concentrations of Co^{2+} released between the uncoated and coated samples in the presence of SA. The results of these studies contradict our hypothesis that phosphate coatings can mitigate cobalt release from $LiCoO_2$. The fact that dissolution is not mitigated may suggest that the phosphate coating is not stable in the presence of acids, which is consistent with the XPS results for phosphate coverage on $LiCoO_2$ decreasing in the presence of LA, though not consistent with the phosphate coverage not being impacted in the presence of SA. However a direct comparison to the XPS results cannot be made as in the XPS studies the particles were exposed to both phosphate and the organic acid simultaneously and at equimolar concentrations.

4.3.6. Cobalt release in the presence of both phosphate and organic acids.

Our experiments on the impact of phosphate coating on Co^{2+} release in the presence of LA and SA clarified that the phosphate coating was not sufficient to mitigate dissolution. We then compared the amount of Co^{2+} released when uncoated $LiCoO_2$ particles were exposed to both 1 mM phosphate and 10 mM LA or SA, or just 10 mM LA or SA in an equal ionic strength control, to obtain more information about how $LiCoO_2$ is impacted when exposed to phosphate and organic

acids at the same time. This experiment is meant to more closely mimic the XPS coverage experiments, however the concentrations between studies are not consistent. Future XPS experiments at the same concentrations will be done to make better comparisons.

The left two bars in Figure 4.7 show the Co^{2+} concentrations measured via ICP-OES for $LiCoO_2$ exposed to LA (blue outline, blue bar) or LA and phosphate (orange outline, blue bar), and the right two bars show the results for SA (blue outline, green fill) or SA and phosphate (orange outline, green fill). For both LA and SA, more Co^{2+} is released from $LiCoO_2$ when exposed to a combination of the organic acid and phosphate. This may suggest that as phosphate is adsorbing to the particles, it is providing enhanced colloidal stability, as reported previously, which is effectively creating higher surface area of particles available for dissolution. Since the previous dissolution experiments showed that phosphate coatings do not mitigate dissolution, it is possible that in this case, when co-exposed, the adsorption of phosphate is actually leading to enhanced dissolution.

The concentration of Co^{2+} released from $LiCoO_2$ is larger in LA than in SA, both for the ionic strength control and phosphate containing samples. This is consistent with other studies that report aliphatic acids have larger impacts on metal release from minerals than aromatic acids. Our XPS results that suggest LA has more of an impact on phosphate adsorption, which may be indicative of LA interacting more strongly with the $LiCoO_2$ surface.[49-50] The ATR-FTIR results were not consistent with LA binding in an inner-sphere fashion to $LiCoO_2$, which may instead mean that the LA observed via ATR-FTIR is physiosorbed, and that LA does not bind to the particles, but instead enhances dissolution either through chelation or even by being oxidized by the Co^{2+} as it is reduced from Co^{3+} during dissolution, as the ATR-FTIR results and similar studies may suggest.[39-40, 44]

4.4. Conclusions.

Investigating the ways that organic acids interact with nanomaterials is an important step towards understanding the role of this class of molecules, and the functionality of these molecules, on the potential environmental impact of nanomaterials. While studying nanoparticle transformations in true environmental waters is challenging due to the presence of a variety of sometimes ill-defined molecules, building up complexity in model systems by developing an understanding of the impacts of different classes of molecules can lead to predictive ability when done in a systematic manner.

There is no doubt that organic acids have impacts on nanomaterials in solution, as has been shown previously on both related materials to $LiCoO_2$ and a broader class of model engineered nanomaterials as well as mineral systems. Understanding the competitive interactions between oxyanions such as phosphate and organic acids can aid in the development of a clearer picture of the important factors to consider for nanoparticle release into true environmental systems.

The results of this study highlight some of the challenges of using traditional analytical techniques to assess primarily carbon containing materials. We were unable to resolve changes in the carbon content of the samples via XPS, and assessing the IR spectrum of these molecules on $LiCoO_2$ can be challenging as well, as peaks tend to be broad and weak. Future work will be aimed at unifying the concentrations used in these studies to allow for more connections to be drawn between experiments.

While phosphate coatings on $LiCoO_2$ did not provide protection from dissolution as anticipated, this hints towards important competitive interactions happening at the surface of $LiCoO_2$ that we can continue to try to isolate using this suite of techniques and other complementary tools. It will also be important to investigate the role of the acids alone on

dissolution to complete this picture. It is worth noting that pH is an important factor in these experiments, and doing these experiments in phosphate had the added benefit of providing a pH buffer that was part of the system of study as opposed to an additional variable. Care will have to be taken to choose buffer systems that will not convolute the results of these future dissolution experiments.

Future studies to unify concentrations used, investigate Co^{2+} release from $LiCoO_2$ in the presence of different organic acids, resolve changes in carbon content from XPS, and apply time-course analysis to ATR-FTIR will allow for a deeper understanding of the phenomena observed in this report.
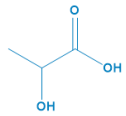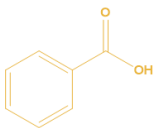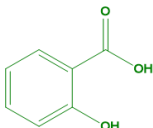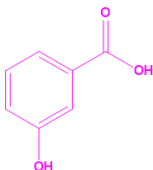
4.5. Figures.
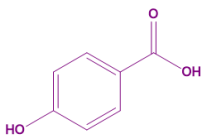
	Lactic acid (LA)	pKa = 3.8
	Benzoic acid (BA)	pKa = 4.25
	Salicylic acid (SA)	pKa = 2.81
	3-hydroxybenzoic acid (3HB)	pKa = 3.96
	4-hydroxybenzoic acid (4HB)	pKa = 4.36

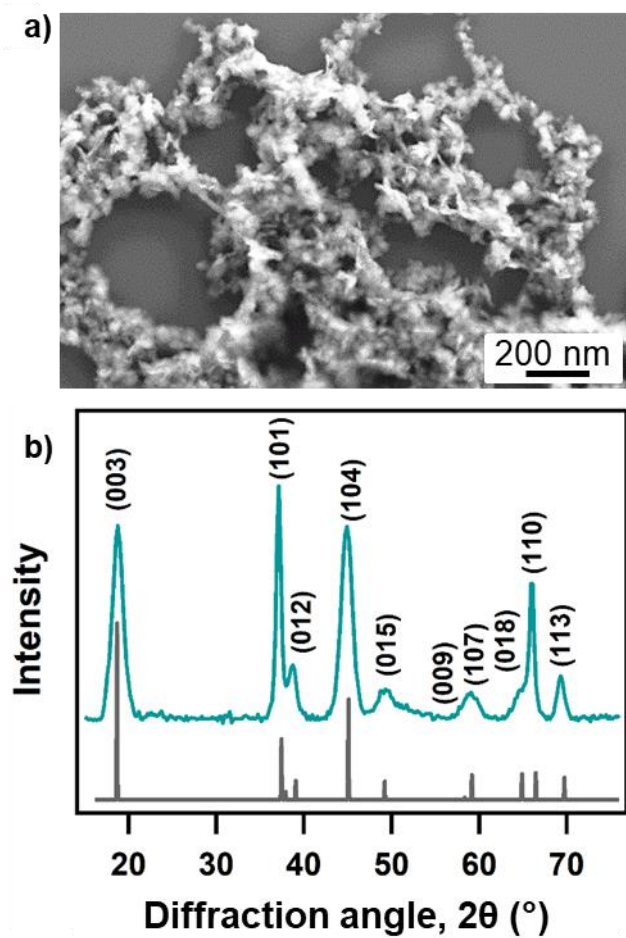Figure 4.1. Chemical structures, abbreviations, and pKa values for the acids used in this study.

Figure 4.2. a) Scanning electron micrograph of LiCoO$_2$ nanosheets. b) X-ray diffraction pattern of LiCoO$_2$ nanosheets (blue) which can be indexed to the R$\overline{3}$m space group. The pattern from the crystallographic information file of single crystal Li$_{0.68}$CoO$_2$ (gray) is shown for comparison.

Figure 4.3. a) Surface coverage of phosphorus in atoms/nm^2 normalized to the control sample for each study when LiCoO$_2$ was exposed to 1 mM phosphate in the presence of 1 mM SA (green bar), 1 mM 3HB (pink bar), 1 mM BA (yellow bar), 1 mM 4HB (purple bar) or 1 mM LA (blue ba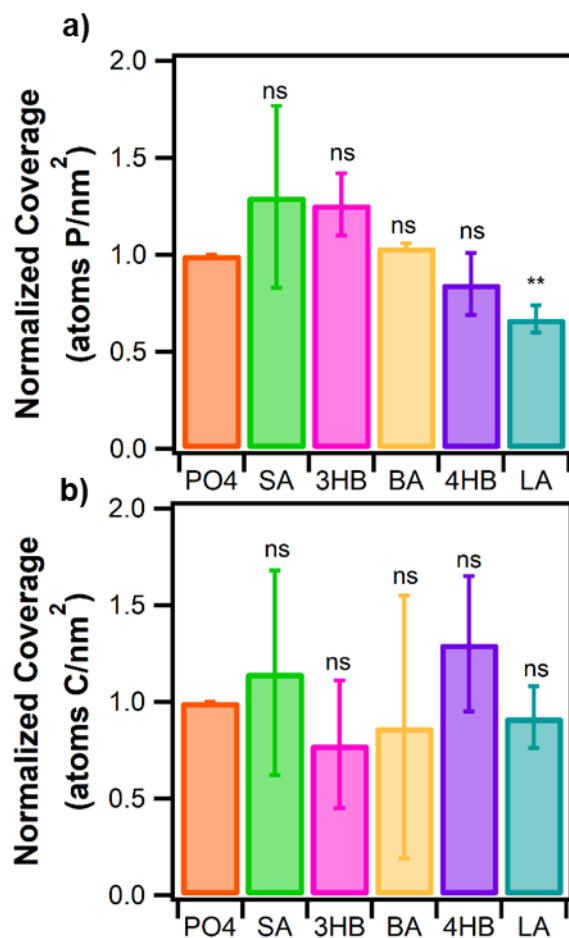r). b) Surface coverage of carbon in atoms/nm^2 normalized to the control sample for each study when LiCoO$_2$ was exposed to 1 mM phosphate in the presence of 1 mM SA (green bar), 1 mM 3HB (pink bar), 1 mM BA (yellow bar), 1 mM 4HB (purple bar) or 1 mM LA (blue bar). ns = no significance, ** = p ≤ 0.01.

Figure 4.4. a) Spectrum of 100 mM LA after exposure to $LiCoO_2$ for one hour (light blue trace, "exposure") and after rinsing away excess LA for one hour (dark blue trace, "surface)". b) Surface spectrum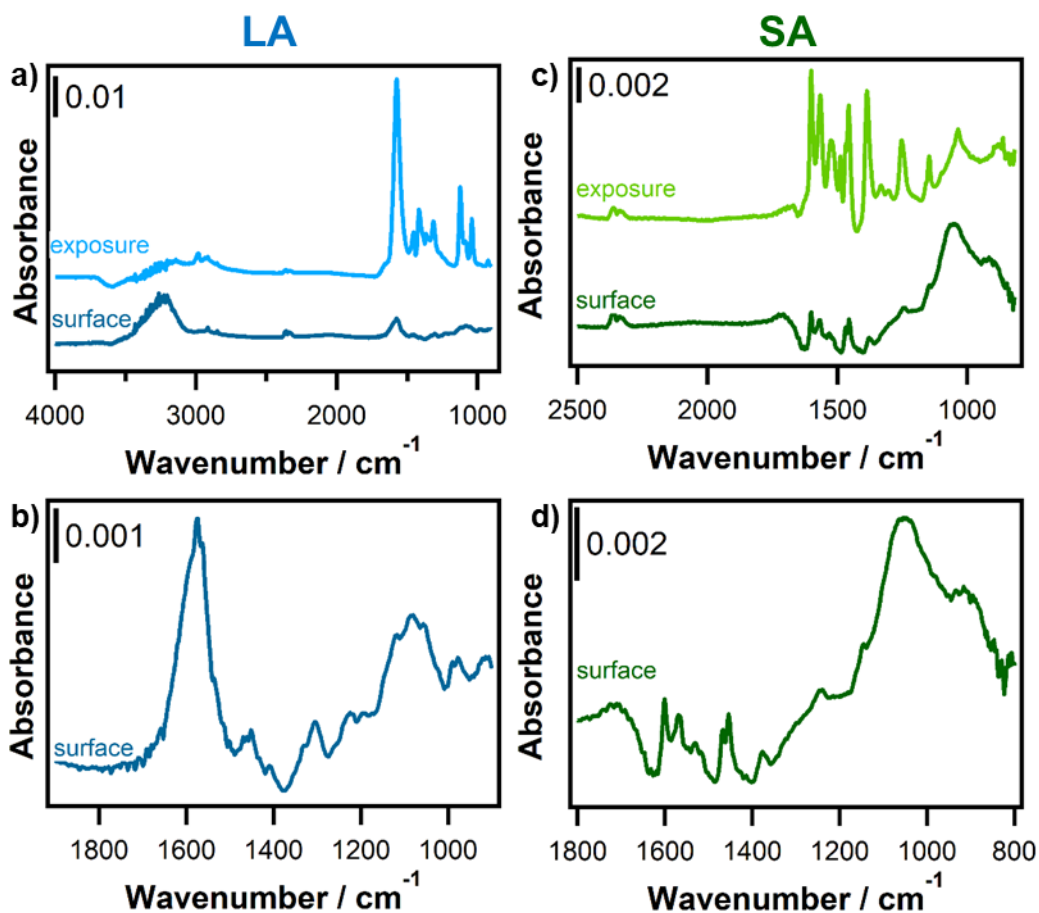 of LA on $LiCoO_2$ after rinsing in the region where LA peaks arise. c) Spectrum of 10 mM SA after exposure to $LiCoO_2$ for one hour (light green trace, "exposure") and after rinsing away excess SA for one hour (dark green trace, "surface)". d) Surface spectrum of SA on $LiCoO_2$ after rinsing in the region where SA peaks arise.
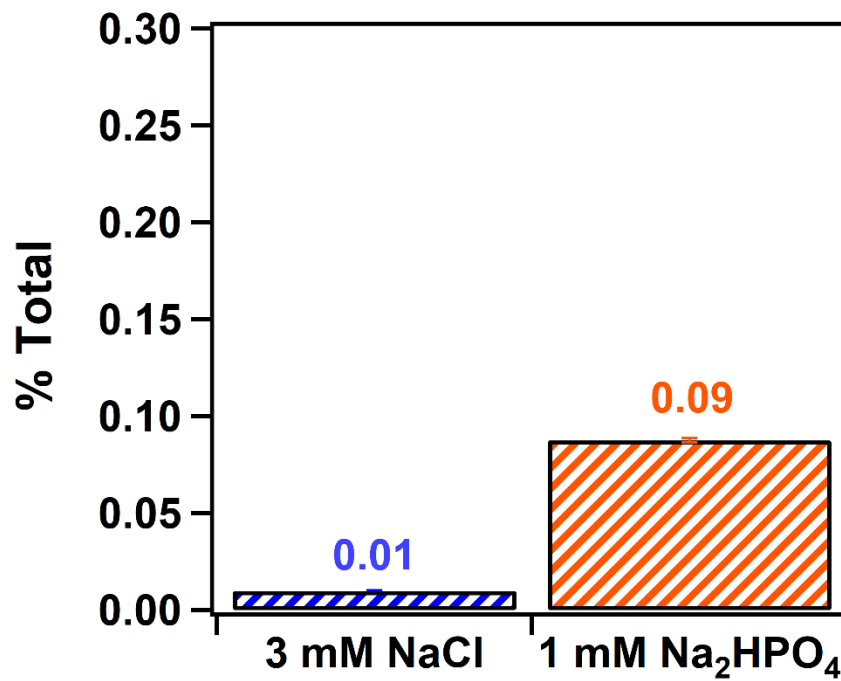
Figure 5. Percent of total cobalt in the LiCoO$_2$ sample that dissolves in the process of exposure to

3 mM NaCl for 1 hour (blue stripes, left) or 1 mM Na$_2$HPO$_4$ for 1 hour (orange stripes, right).
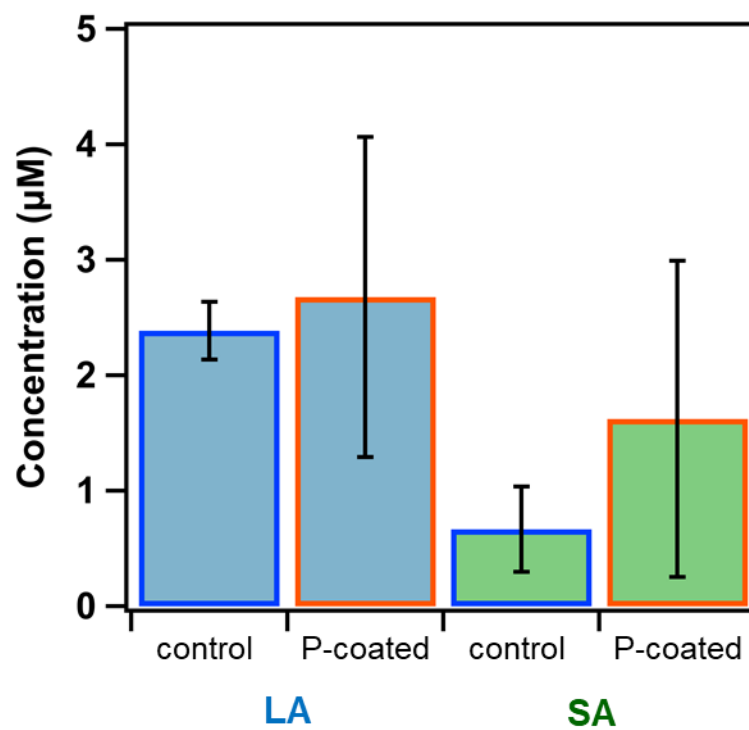
Figure 6. Concentration of Co^{2+} detected after dissolution of uncoated (blue outline) or

phosphate-coated (orange outline) $LiCoO_2$. Blue fill = in 10 mM LA, green fill = in 10 mM SA.
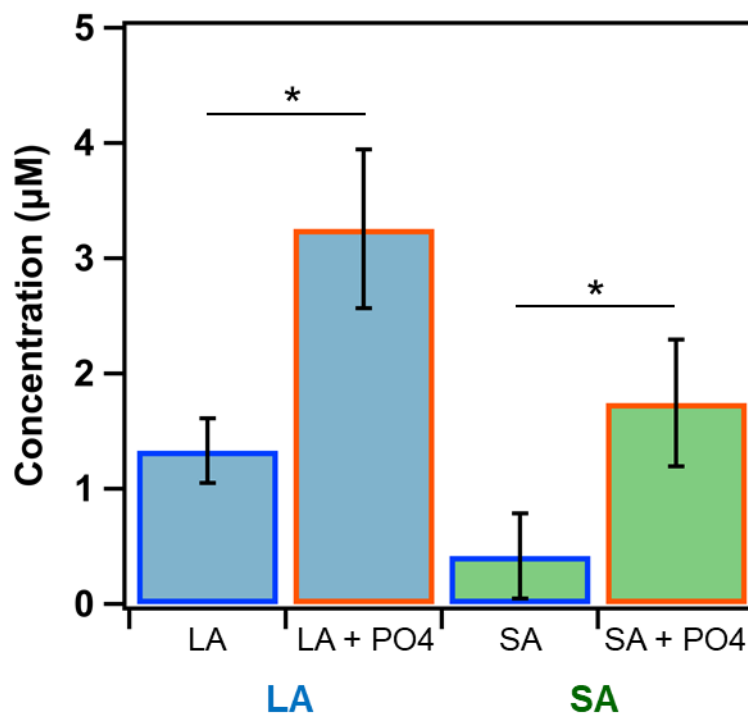
Figure 7. Concentration of Co^{2+} detected after dissolution of $LiCoO_2$ after exposure to 10 mM

LA (blue fill) with (orange outline) and without (blue outline) 1 mM phosphate, and after

exposure to 10 mM SA (green fill) with (orange outline) and without (blue outline) 1 mM

phosphate. * indicates $p \leq 0.05$.

Exposure	Surface	Assignment
1575	1574	$\nu_{as}(COO^-)$
	1470	$\delta_{as}(CH_3)$
1456	1452	$\delta_{as}(CH_3)$
1416	1410	$\nu_s(COO^-)$
1365		$\delta_s(CH_3)$
1315	1306	$\delta(C\text{-}H)$
	1225	Potential degradation
	1196	Potentially pyruvate
1124	1117	$\rho(CH_3) + \nu AL(C\text{-}O)$
1086	1080	$\nu AL(C\text{-}O)$
1041	1057	$\nu AL(C\text{-}O)$

Table 1. Vibrational modes of LA. Peak locations and assignments after exposure to $LiCoO_2$ and after rinsing away excess LA, revealing the modes of the LA associated with the $LiCoO_2$ surface. ν = stretching, ρ = rocking, δ = bending.

Exposure	Surface	Assignment
1601	1601	ν(C-C) ring
1567	1570	ν_{as}(COO$^-$)
1489		ν(C-C) ring
1456	1454	ν(C-C) ring
1387	1377	ν_s(COO$^-$)
1333		δ(C-OH) (ring)
1302		δ(OH)
1252	1240	ν(C-O) (ring)
1159		δ(C-H) inner plane
1146	1146	δ(C-H) inner plane
1034	1049	δ(C-H) inner plane

Table 1. Vibrational modes of SA. Peak locations and assignments after exposure to LiCoO$_2$ and after rinsing away excess SA, revealing the modes of the SA associated with the LiCoO$_2$ surface. ν = stretching, ρ = rocking, δ = bending.

4.6. References.

1.   Kanan, M. W.; Surendranath, Y.; Nocera, D. G., Cobalt–phosphate oxygen-evolving compound. *Chemical Society Reviews* **2009,** *38*, 109-114.

2.   Zhong, D. K.; Cornuz, M.; Sivula, K.; Gratzel, M.; Gamelin, D. R., Photo-assisted electrodeposition of cobalt–phosphate (Co–Pi) catalyst on hematite photoanodes for solar water oxidation. *Energy Environ. Sci.* **2011,** *4*, 1759-1764.

3.   Lu, Z. Y.; Wang, H. T.; Kong, D. S.; Yan, K.; Hsu, P. C.; Zheng, G. Y.; Yao, H. B.; Liang, Z.; Sun, X. M.; Cui, Y., Electrochemical tuning of layered lithium transition metal oxides for improvement of oxygen evolution reaction. *Nat. Commun.* **2014,** *5*, 7.

4.   Whittingham, M. S., Lithium Batteries and Cathode Materials. *Chem. Rev.* **2004,** *104*, 4271-4301.

5.   Xiao, X.; Liu, X.; Wang, L.; Zhao, H.; Hu, Z.; He, X.; Li, Y., LiCoO2 Nanoplates with Exposed (001) Planes and High Rate Capability for Lithium-Ion Batteries. *Nano. Res.* **2012,** *5* (6), 395-401.

6.   Okubo, M.; Hosono, E.; Kim, J.; Enomoto, M.; Kojima, N.; Kudo, T.; Zhou, H.; Honma, I., Nanosize Effect on High-Rate Li-Ion Intercalation in LiCoO2 Electrode. *Journal of the American Chemical Society* **2007,** *129*, 7444-7452.

7.   Bozich, J.; Hang, M.; Hamers, R.; Klaper, R., Core Chemistry Influences the Toxicity of Multicomponent Metal Oxide Nanomaterials, Lithium Nickel Manganese Cobalt Oxide, and Lithium Cobalt Oxide to *Daphnia magna*. *Environmental Toxicology and Chemistry* **2017,** *36* (9), 2493-2592.

8.   Dogangun, M.; Hang, M. N.; Machesky, J.; McGeachy, A. C.; Dalchand, N.; Hamers, R. J.; Geiger, F. M., Evidence for Considerable Metal Cation Concentrations from Lithium

Intercalation Compounds in the Nano−Bio Interface Gap. *J. Phys. Chem. C* **2017,** *121*, 27473-27482.

9.   Dogangun, M.; Hang, M. N.; Troiano, J. M.; McGeachy, A. C.; Melby, E. S.; Pedersen, J. A.; Hamers, R. J.; Geiger, F. M., Alteration of Membrane Compositional Asymmetry by LiCoO2 Nanosheets. *ACS Nano* **2015,** *9* (9), 8755-8765.

10.   Gunsolus, I. L.; Hang, M. N.; Hudson-Smith, N. V.; Buchman, J. T.; Bennett, J. W.; Conroy, D.; Mason, S. E.; Hamers, R. J.; Haynes, C. L., Influence of nickel manganese cobalt oxide nanoparticle composition on toxicity toward Shewanella oneidensis MR-1: redesigning for reduced biological impact. *Environ. Sci.: Nano* **2017,** *4* (3), 636-646.

11.   Hang, M. N.; Gunsolus, I. L.; Wayland, H.; Melby, E. S.; Mensch, A. C.; Hurley, K. R.; Pedersen, J. A.; Haynes, C. L.; Hamers, R. J., Impact of Nanoscale Lithium Nickel Manganese Cobalt Oxide (NMC) on the Bacterium Shewanella oneidensis MR-1. *Chemistry of Materials* **2016,** *28*, 1092-1100.

12.   Notter, D. A.; Gauch, M.; R., W.; Wagner, P.; Stamp, A.; Zah, R.; Althaus, H.-J., Contribution of Li-Ion Batteries to the Environmental Impact of Electric Vehicles. *Environ. Sci. Technol.* **2010,** *44*, 6550-6556.

13.   Dunn, J. B.; Gaines, L.; Kelly, J. C.; James, C.; Gallagher, K. G., The significance of Li-ion batteries in electric vehicle life-cycle energy and emissions and recycling's role in its reduction. *Energy Environ. Sci.* **2015,** *8* (1), 158-168.

14.   Ellingsen, L. A.; Hung, C. R.; Majeau-Bettez, G.; Singh, B.; Chen, Z.; Whittingham, M. S.; Stromman, A. H., Nanotechnology for environmentally sustainable electromobility. *Nat Nanotechnol* **2016,** *11* (12), 1039-1051.

15.   Laudadio, E. D.; Bennett, J. W.; Green, C. M.; Mason, S. E.; Hamers, R. J., Impact of Phosphate Adsorption on Complex Cobalt Oxide Nanoparticle Dispersibility in Aqueous Media. *Environ. Sci. Technol.* **2018,** *52*, 10186-10195.

16.   Laudadio, E. D.; Ilani-Kashkouli, P.; Green, C. M.; Kabengi, N. J.; Hamers, R. J., Interaction of Phosphate with Lithium Cobalt Oxide Nanoparticles: A Combined Spectroscopic and Calorimetric Study. *Langmuir* **2019,** *35* (50), 16640-16649.

17.   Chen, J.; Xiu, Z.; Lowry, G. V.; Alvarez, P. J., Effect of natural organic matter on toxicity and reactivity of nano-scale zero-valent iron. *Water Res* **2011,** *45* (5), 1995-2001.

18.   JOHNSON, R. I. L.; JOHNSON, G. O. B.; NURMI, J. T.; TRATNYEK, P. G., Natural Organic Matter Enhanced Mobility of Nano Zerovalent Iron. *Environ. Sci. Technol.* **2009,** *43*, 5455–5460.

19.   Mensch, A. C.; Hernandez, R. T.; Kuether, J. E.; Torelli, M. D.; Feng, Z. V.; Hamers, R. J.; Pedersen, J. A., Natural Organic Matter Concentration Impacts the Interaction of Functionalized Diamond Nanoparticles with Model and Actual Bacterial Membranes. *Environ. Sci. Technol.* **2017,** *51* (19), 11075-11084.

20.   Li, L.; Ge, J.; chen, R.; wu, f.; chen, s.; zhang, X., Environmental friendly leaching reagent for cobalt and lithium recovery from spent lithium-ion batteries. *Waste Management* **2010,** *30*, 2615-2621.

21.   Li, L.; Ge, J.; Wu, F.; Chen, R.; Chen, S.; Wu, B., Recovery of cobalt and lithium from spent lithium ion batteries using organic citric acid as a leachant. *Journal of Hazardous Materials* **2010,** *176*, 288-293.

22.	Li, L.; Lu, J.; Ren, Y.; Zhang, X.; Chen, R.; Wu, F.; Amine, K., Ascorbic-acid-assisted recovery of cobalt and lithium from spent Li-ion batteries. *Journal of Power Sources* **2012,** *218*, 21-27.

23.	Li, L.; Qu, W.; Zhang, X.; Lu, J.; Chen, R.; Wu, F.; Amine, K., Succinic acid-based leaching system: A sustainable process for recovery of valuable metals from spent Li-ion batteries:. *Journal of Power Sources* **2015,** *282*, 544-551.

24.	Sun, C.; Xu, L.; Chen, X.; Qiu, T.; Zhou, T., Sustainable recovery of valuable metals from spent lithium-ion batteries using DL-malic acid: Leaching and kinetics aspect. *Waste Manag Res* **2018,** *36* (2), 113-120.

25.	Sun, L.; Qiu, K., Organic oxalate as leachant and precipitant for the recovery of valuable metals from spent lithium-ion batteries. *Waste Management* **2012,** *32*, 1575-1582.

26.	Chen, H.; Grey, C. P., Molten Salt Synthesis and High Rate Performance of the ''Desert-Rose'' form of LiCoO2**. *Advanced Materials* **2008,** *20*, 2206-2210.

27.	Wu, H.; Gonzalez-Pech, N. I.; Grassian, V. H., Displacement reactions between environmentally and biologically relevant ligands on TiO2 nanoparticles: insights into the aging of nanoparticles in the environment. *Environ. Sci.: Nano* **2019,** *6*, 489-504

28.	Powell, C. J.; Jablonski, A. *NIST Electron Effective-Attenuation-Length Database*, version 1.3; National Institute of Standards and Technology: Gaithersburg, MD, 2011.

29.	Tanuma, S.; Powell, C. J.; Penn, D. R., Calculation of Electron Inelastic Mean Free Paths (IMFPs) VII. Reliability of the TPP-2M IMFP Predictive Equation. *Surf. Interface Anal.* **2003,** *35*, 268-275.

30. Takahashi, Y. K., N.; Dokko, K.; Nishizawa, M.; Akimoto, J.; Uchida, I., Structure and electron density analysis of electrochemically and chemically delithiated Li Co O2 single crystals. *Journal of Solid State Chemistry* **2007,** *180*, 313-321.

31. Mizushima, K.; Jones, P. C.; Wiseman, P. J.; Goodenough, J. B., LixCoO2: A New Cathode Material for Batteries of High Energy Density. *Mat. Res. Bull* **1980,** *15*, 783-789.

32. Huang, X.; Bennett, J. W.; Hang, M. N.; Laudadio, E. D.; Hamers, R. J.; Mason, S. E., Ab Initio Atomistic Thermodynamics Study of the (001) Surface of LiCoO2 in a Water Environment and Implications for Reactivity under Ambient Conditions. *The Journal of Physical Chemistry C* **2017,** *121* (9), 5069-5080.

33. Kim, T.; Song, W.; Son, D.-Y.; Ono, L. K.; Qi, Y., Lithium-ion batteries: outlook on present, future, and hybridized technologies. *Journal of Materials Chemistry A* **2019,** *7* (7), 2942-2964.

34. Maiyalagan, T.; Jarvis, K. A.; Therese, S.; Ferreira, P. J.; Manthiram, A., Spinel-type lithium cobalt oxide as a bifunctional electrocatalyst for the oxygen evolution and oxygen reduction reactions. *Nat. Commun.* **2014,** *5*, 1-8.

35. Fernandez-Rodriguez, J. M.; Hernan, L.; Morales, J.; Tirado, J. L., Low-temperature hydrothermal transformations of LiCoO2 and HCoO2. *Mat. Res. Bull* **1988,** *23*, 899-904.

36. Gardner, S. D.; Singamsetty, C. S. K.; Booth, G. L.; He, G.; Pittman Jr, C. U., Surface Characterization of Carbon Fibers Using Angle-Resolved XPS and ISS. *Carbon* **1995,** *33* (5), 587-595.

37. Ha, J.; Yoon, T. H.; Wang, Y.; Musgrave, C. B.; Brown, G. E. J., Adsorption of Organic Matter at Mineral/Water Interfaces: 7. ATR-FTIR and Quantum Chemical Study of Lactate Interactions with Hematite Nanoparticles. *Langmuir* **2008,** *24*, 6683-6692.

38.   Ramos, M. E.; Huertas, F. J., Adsorption of lactate and citrate on montmorillonite in aqueous solutions. *Applied Clay Science* **2014,** *90*, 27-34.

39.   Awatani, T.; Dobson, K. D.; McQuillan, A. J.; Ohtani, B.; Uosaki, K., In situ Infrared Spectroscopic Studies of Adsorption of Lactic Acid and Related Compounds on the TiO2 and CdS Semiconductor Photocatalyst Surfaces from Aqueous Solutions. *Chemistry Letters* **1998,** *27* (8), 849-850.

40.   Chen, Y.-K.; Lin, Y.-F.; Peng, Z.-W.; Lin, J.-L., Transmission FT-IR Study on the Adsorption and Reactions of Lactic Acid and Poly(lactic acid) on TiO2. *J. Phys. Chem. C* **2010,** *114*, 17720-17727.

41.   Cornell, R. M.; Schindler, P. W., Infrared study of the adsorption of hydroxycarboxylic acids on a-FeOOH and amorphous Fe (III)hydroxide. *Colloid & Polymer Sci.* **1980,** *258*, 117101175.

42.   Kim, K. S.; Barteau, M. A., Adsorption and Decomposition of Aliphatic Alcohols on Ti02. *Langmuir* **1988,** *4*, 533-543.

43.   Hussein, G. A. M.; Sheppard, N.; Zaki, M. I.; Fahim, R. B., Infrared Spectroscopic Studies of the Reactions of Alcohols over Group IVB Metal Oxide Catalysts. *J. Chem. Soc., Faraday Trans. 1* **1989,** *85* (7), 1723-1742.

44.   Henke, A. H.; Laudadio, E. D.; Hedlund Orbeck, J. K.; Hoang, K. N. L.; Murphy, C. J.; Feng, Z. V.; Hamers, R. J., Redox-mediated Dissolution of Lithium Cobalt Oxide (LiCoO2) Nanoparticles from Interaction with Nicotinamide Adenine Dinucleotide (NADH) and Glutathione (GSH). *In preparation.* **2020**.

45.   Yost, E. C.; Tejedor-Tejedor, M. I.; Anderson, M. A., In Situ CIR-FTIR Characterization off Salicylate Complexes at the Goethite/Aqueous Solution Interface. *Environ. Sci. Technol.* **1990,** *24*, 822-828.

46.   Kubicki, J. D.; Itoh, M. J.; Schroeter, L. M.; Apitz, S. E., Bonding Mechanisms of Salicylic Acid Adsorbed onto Illite Clay: An ATR-FTIR and Molecular Orbital Study. *Environ. Sci. Technol.* **1997,** *31*, 1151-1156.

47.   Buchman, J. T.; Bennett, E. A.; Wang, C.; Abbaspour Tamijani, A.; Bennett, J. W.; Hudson, B. G.; Green, C. M.; Clement, P. L.; Zhi, B.; Henke, A. H.; Laudadio, E. D.; Mason, S. E.; Hamers, R. J.; Klaper, R. D.; Haynes, C. L., Nickel enrichment of next-generation NMC nanomaterials alters material stability, causing unexpected dissolution behavior and observed toxicity to S. oneidensis MR-1 and D. magna. *Environmental Science: Nano* **2020,** *7*, 571-587.

48.   Hang, M. N.; Hudson-Smith, N. V.; Clement, P. L.; Zhang, Y.; Wang, C.; Haynes, C. L.; Hamers, R. J., Influence of Nanoparticle Morphology on Ion Release and Biological Impact of Nickel Manganese Cobalt Oxide (NMC) Complex Oxide Nanomaterials. *ACS Applied Nano Materials* **2018,** *1* (4), 1721-1730.

49.   Neaman, A.; Chorover, J.; Brantley, S. L., Implications of the Evolution of Organic Acid Moieties for Basalt Weathering over Geological Time. *American Journal of Science* **2005,** *305*, 147-185.

50.   Manley, E. P.; Evans, L. J., Dissolution of feldspars by low-molecular-weight aliphatic and aromatic acids. *Soil Science* **1986,** *141* (2), 106-112.

Chapter 5. Conclusions and Future Directions

The invention of the lithium ion battery is one of the most impactful discoveries of our time. The versatility of their use, from small scale appliances to large electric vehicles, highlights both how far this technology has come, and underscores the vast potential that still remains. While lithium ion batteries have and continue to revolutionize technology, the assumption that these systems are inherently sustainable has shown to not be absolute. As researchers continue to optimize the materials and performance of the batteries themselves, continued analysis of the environmental burdens of production, recycling, and disposal are vital to ensuring sustainable development.

This work provides the first look into the potential environmental impacts of the nanomaterials of lithium ion battery cathodes, specifically $LiCoO_2$, upon unintentional release through improper disposal. We chose to focus on the phosphate oxyanion as an important environmental and biological model molecule, and developed methodologies to apply in situ surface chemical analysis to the interactions between phosphate and $LiCoO_2$ at the nanoparticle-liquid interface. Using attenuated total reflectance – FTIR, we were able to show that phosphate oxyanion adsorbs irreversibly to the surface of $LiCoO_2$ nanoparticles, even at environmentally relevant concentrations of ~ 1 µM. Deconvoluting the P-O vibrational modes allowed us to assign a predominantly deprotonated, bidentate geometry to the phosphate adsorbed to the surface. We hypothesized therefore that the surface charge of $LiCoO_2$ would become negative due to the deprotonated phosphates on the particle surfaces, which was confirmed using laser doppler microelectrophoresis. Both dynamic light scattering and UV-visible spectroscopy elucidated the consequence of this irreversible adsorption and enhanced negative surface charge, that the colloidal stability of the particles was enhanced.

This work led us to consider the different ways that phosphate might interact with $LiCoO_2$ as a function of the range of pH values relevant to environmental systems. We chose to investigate the thermodynamics of phosphate absorption to $LiCoO_2$ as a function of pH between 5.6 and 9.0. Flow microcalorimetry experiments revealed two distinct modes of interaction of phosphate with the $LiCoO_2$ surface at pH 7.4. This was unlike the results at pH 5.6 and pH 9.0, which revealed a single exothermic peak, with more heat being evolved at lower pH. At pH 7.4 however, more heat was evolved than at both pH 5.6 and 9.0, and the interaction went on for a longer period of time. Ion chromatography analysis of the effluent of this experiment revealed that the same amount of phosphate adsorbed to $LiCoO_2$ at both pH 5.6 and pH 7.4, clarifying that the increased heat evolved was not simply a result of more phosphate adsorbing to the surface. Instead, two distinct exothermic interactions appeared to be taking place, likely due to restructuring of phosphate on the surface. We applied two-dimensional cross correlation analysis to time-course attenuated total reflectance FTIR spectra to reveal the order in which specific phosphate vibrational modes grew into the spectra, corresponding with the geometric transformation of phosphate on the surface from a monodentate to bidentate coordination, through two subsequent condensation reactions. The combined use of these two in situ methodologies, presented here for what we believe is the first time, allowed us to propose a mechanism for interaction and develop a more complete picture of the reaction than would be possible using just one of the techniques alone.

The analytical toolkit applied to the deep assessment of phosphate interaction with $LiCoO_2$ was then used to build systematic complexity of our model environmental systems. Organic acids are present in a variety of environmentally and biologically relevant systems, and also can be considered to be surrogate molecules for natural organic matter. Understanding the role of chemical group functionality on the interaction of the molecules with $LiCoO_2$ can elucidate the

moieties responsible for association with the particle surfaces. We found that hydrophobicity and steric hinderance of salicylic acid limited its ability to associate with the $LiCoO_2$ surface in a way that would enhance the dissolution of cobalt from the material, whereas exposure to the smaller, more labile lactic acid resulted in greater cobalt release. Lactic acid also mitigated phosphate adsorption to the surface, while salicylic acid did not. Phosphate coatings were not able to mitigate cobalt dissolution from the particles when exposed to either lactic acid or salicylic acid, refuting the hypothesis that these coatings would be stable in the presence of other molecules and therefore able to protect the material from dissolution. Instead, these results highlight the importance of studying competitive interactions of relevant molecules with the nanoparticle surface, as considering single molecules alone does not capture the range of complex interactions that may occur in actual environmental systems. Therefore, the toolkit established in this work should be used to build up model systems in a controlled manner, to continue to elucidate the important factors that dictate the interaction of small molecules with $LiCoO_2$, and therefore will influence the ultimate fate and transport of these materials.

The work presented here on $LiCoO_2$ also raises the question, are these findings universal? Would these model molecules behave similarly with NMC or other cathode materials? Determining the generalizability of these findings will be important moving forward. The complexity of the composition of NMC and other mixed transition metal oxides may present a more challenging analysis, especially in the case of dissolution experiments, where it has already been shown that the ions are released in a non-stoichiometric manner, and the amount of release is highly dependent on the complexity of the dissolution matrix.

Developing an understanding, both of the impact of nanomaterials on the environment, and also the interaction of that environment with the nanomaterials, is a complex task. The research

discussed here can provide the groundwork for future studies, as well as the toolkit developed in this work can provide a framework for future experimental design. It is our hope that this fundamental backbone of experiment development and subsequent analysis will aid in the eventual closing of the gap between understanding these transformations in model systems and true ones.

Appendix

Appendix 2. Supporting information for Chapter 2: Impact of Phosphate Adsorption on Complex Cobalt Oxide Nanoparticle Dispersibility in Aqueous Media.

A.2.1. Supplemental Materials and Methods.

A.2.1.1. General.

A Thermo Scientific Sorvall Legend X1R Centrifuge with a Thermo TX-400 rotor at 4696 g was used for all centrifugation described. All reagents were purchased from Sigma-Aldrich, and ultrapure water (18.2 MΩ/cm resisitivity) was used in all experiments.

A.2.1.2. Surface area measurements of $LiCoO_2$ nanoparticles.

We determined the specific surface areas of $LiCoO_2$ nanosheets according to the Brunauer-Emmet-Teller (BET) model using N_2 adsorption/desorption isotherms.[1] Each sample holder (Micromeritics) was loaded with ~100 mg of dry nanoparticles and outgassed at 150 °C under vacuum for 20 h using a Micromeritics VacPrep 061 Sample Degas System. Each sample was analyzed with a Micromeritics Gemini VII 2390 Surface Area Analyzer over the relative pressure range (P/P$_0$) of 0.05 to 0.3, where P$_0$ is the pressure of N_2 required to saturate the surface. Surface area values of 130 m^2/g were obtained for $LiCoO_2$ nanoparticles.

A.2.1.3. Determination of extent lithiation using Inductively Coupled Plasma – Optical Emission Spectroscopy.

To analyze Li and Co content, we performed ICP-OES PerkinElemer Optima 2000 spectrometer. $LiCoO_2$ nanoparticles were in aqua regia (3:1 v/v mixture of 30% v/v HCl and 70% v/v HNO_3, caution-highly corrosive!) and diluted in water. These measurements give a Li:Co ratio of 0.62 ± 0.07.

A.2.1.4. attenuated total reflectance – FTIR.

Spectra were acquired at 4 cm^{-1} averaging 500 scans per spectrum. In each experiment, a reference spectrum was obtained after flowing 1 mL of water over the LiCoO$_2$ -coated ZnSe at 0.5 mL/min. A solution of 0.1 mg/L Na$_2$HPO$_4$ (previously purged with nitrogen to remove dissolved gases) was then flowed continually (0.5 mL/min) while repeated spectra were acquired over 1 hr. Time-dependent measurements show that the absorbance of the bands in the P-O stretching region reached a constant value well before 1 hr. To test whether adsorption was reversible, we flowed water through the cell at 0.5 mL/min while taking repeated spectra for 1 h. All spectra shown here were referenced to the spectrum of ultrapure water over the LiCoO$_2$ film. The volume of the cell is 0.55 mL, and so for each 1 hr interval where solutions were being flowed, approximately 54 full volume exchanges of the flow cell occurred. Peaks were deconvoluted using FitYK software.[2]

A.2.1.5. Quantitative analysis of phosphate adsorption by X-ray Photoelectron Spectroscopy.

Samples were prepared using 250 ml of a 100 mg/L suspension of LiCoO$_2$ in 1 mM Na$_2$HPO$_4$ adjusted to pH 7.3. The solutions were stirred throughout the experiment. Aliquots (50 ml each) were removed after 3 h, 24 h, 48 h, 72 h, and 172 h of exposure. Particles in each aliquot were isolated via centrifugation (4696 g, 10 min), redispersed in ultra-pure water to remove unadsorbed phosphate, and immediately re-isolated via centrifugation. The pellet was left allowed to dry under vacuum at room temperature for at least 24 h. Once dry, the sample was pressed into indium foil on copper foil using a hydraulic press to obtain a flat sample for XPS analysis. XPS data were acquired on either a custom-built ultrahigh-vacuum Phi instrument with a monochromatized Al Kα source (1486.6 eV photon energy) and a hemispherical electron energy analyzer or a Thermo Fisher Scientific K-alpha XPS. Spectra were collected at 45° photoelectron

takeoff angles and XPS spectra were fit using CasaXPS software.[3] The inelastic mean free path of Co was estimated using the NIST Effective Attenuation Length Database via the TPP-2M equation.[4-5] Li (1s), Co(2p), O(1s), Na(1s), C(1s) and P(2p) peaks were monitored and Co 2p and P 2p peak areas were used for quantitative analysis of surface coverage (Equation A.1).

$$Coverage = \frac{A_{P,2p}}{A_{Co,2p}} \times \frac{SF_{Co,2p}}{SF_{P,2p}} \times \frac{Scans_{Co,2p}}{Scans_{P,2p}} \times \rho_{Co,2p} \times \lambda_{Co,2p} \times \cos\theta$$

Equation A.1. Monolayer coverage estimation for quantitative XPS analysis. A = peak area, SF = atomic sensitivity factor (SF (Co,2p) = 3.255 for custom instrument, 18.23529 for Thermo instrument, SF (P,2p) = 0.412 for custom instrument, 1.352941 for Thermo instrument), ρ= density of cobalt in $LiCoO_2$ (30 atoms/nm^2), λ = inelastic mean free path of Co electron emitted from $LiCoO_2$, (1.922 nm) θ= Angle of the analyzer to the surface normal (45° for the instruments used here). Scans refers to the number of scans that were summed to achieve the total peak area.

A.2.1.6. Sample preparation for Dynamic Light Scattering and Laser Doppler Microelectrophoresis.

Phosphate solutions were prepared from 10^{-7} to 10^{-2} M Na_2HPO_4. Ionic strength was controlled through the addition of NaCl to obtain ionic strength values of 30 mM for all samples. Ionic strengths were calculated with the assumption that $Na_2HPO_4 \rightarrow 2\ Na^+ + HPO_4^{2-}$ and that subsequent protonation/deprotonation reactions of HPO_4^- are negligible. The pH of all solutions except the two highest concentrations of phosphate was approximately neutral (6.9 - 7.2), with the 10 mM and 1 mM Na_2HPO_4 solutions having pH of 8.4 and 8.1, respectively. We did not further adjust the pH in order to avoid altering the concentrations and ionic strength of the small-volume samples (800 µL).

A.2.1.7. UV-Vis Sedimentation Analysis.

The transmission of light through a sample is attenuated by both true optical absorption and by scattering of light out of the path of the transmitted optical beam. Since intensity loss due to true optical absorption and by scattering are both expected to be proportional to nanoparticle concentration[6-10], we use the *apparent* absorption $A_{apparent} = -log_{10}\left(\frac{I_{transmitted}}{I_{incident}}\right)$ to measure the sedimentation. The sample volume was limited through the use of a 3 mm aperture aligned towards the top of the cuvette, such that only the absorbance in approximately the top 3 mm of the solution was being measured.

A.2.1.8. Preparation of Dissolution Samples.

MHW was prepared by making a 96 mg/L $NaHCO_3$, 60 mg/L $CaSO_4$, 60 mg/L $MgSO_4$, and 4 mg/L KCl solution in ultrapure water. The solution was aerated for 72 h before use and used within 14 days of preparation. $LiCoO_2$ was added to MHW and MHW with phosphate to achieve the desired particle concentration. The solutions were stirred for 24 h, after which an aliquot was removed. Samples were centrifuged for 20 min and the supernatant was removed and acidified to 2% with high purity HNO_3 and analyzed for total Co concentration using a magnetic-sector Thermo-Finnigan Element 2XR ICP-MS.

A.2.2. Additional Figures.

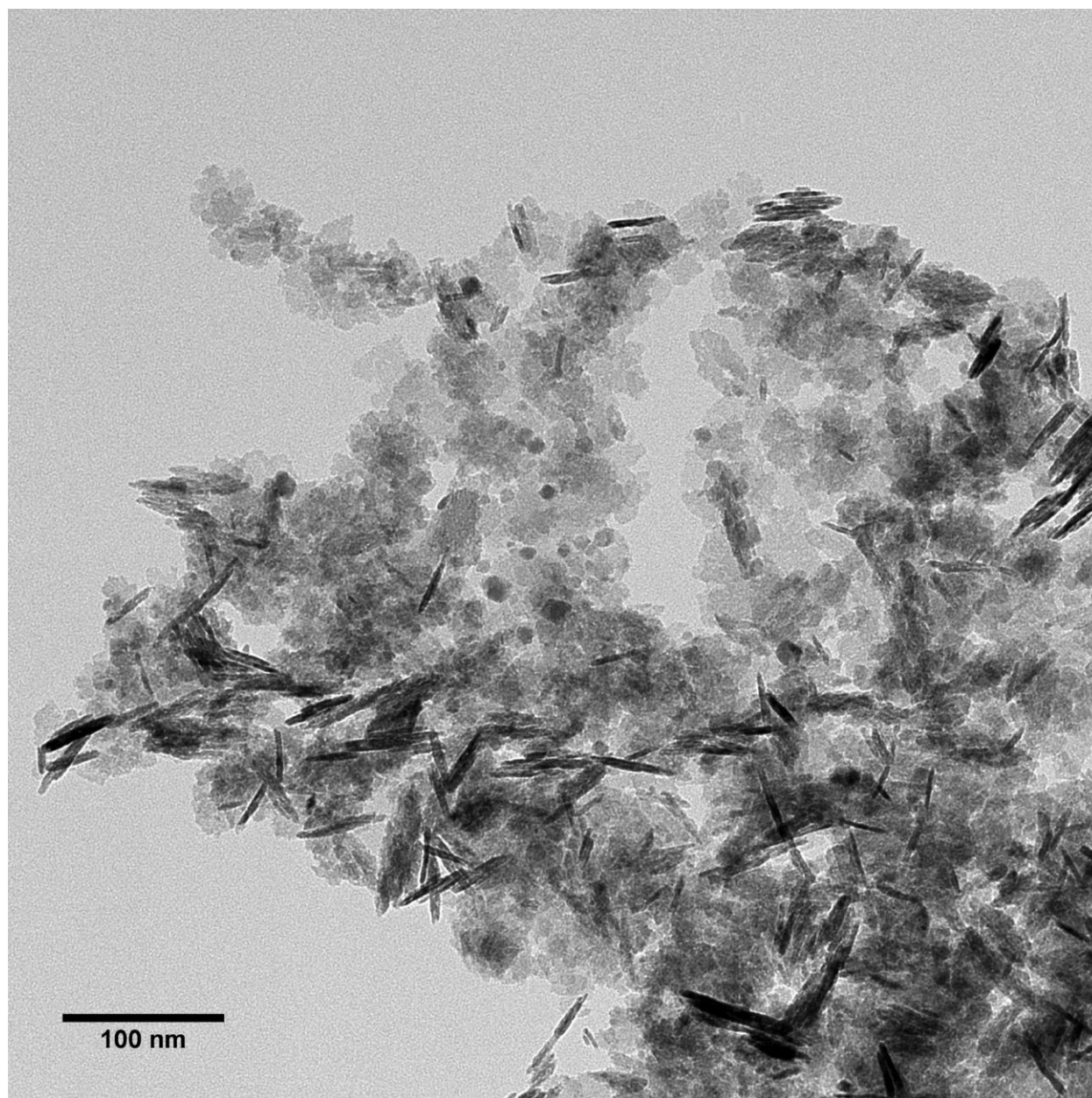**A.2.2.1. Figure A.2.1. TEM micrograph of LiCoO$_2$ particles.**

Figure A.2.1. TEM micrograph of LiCoO$_2$ nanosheets.

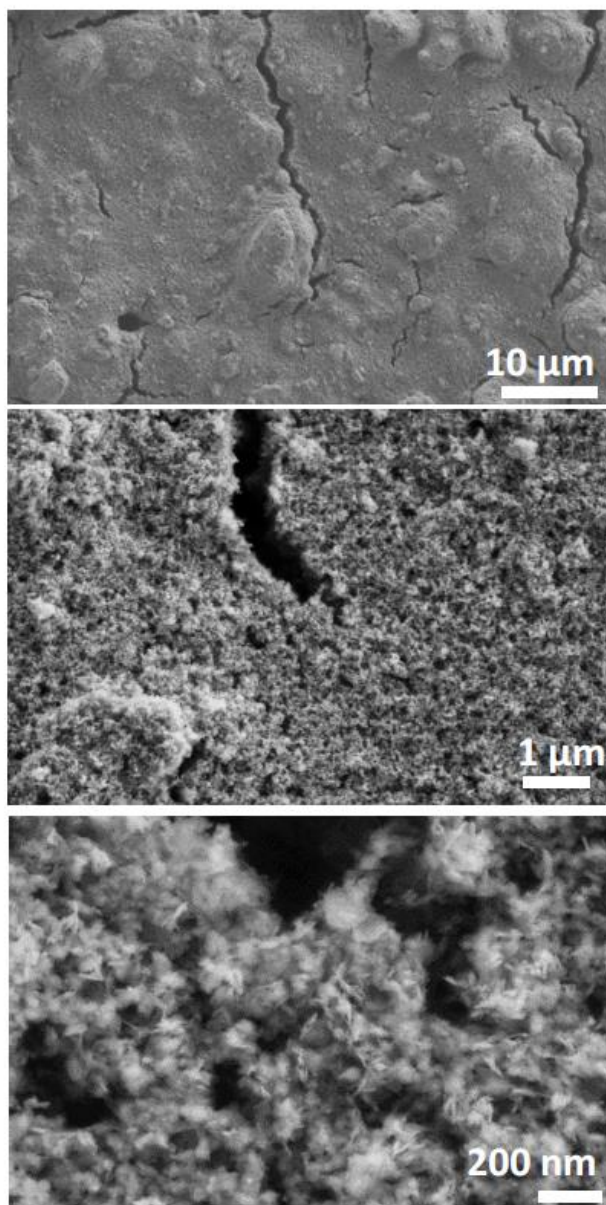**A.2.2.2. Figure A.2.2. SEM micrographs of spin-cast nanoparticle films.**

Figure A.2.2. SEM micrographs of spin-cast nanoparticle films. Films are fairly continuous, and consist of randomly-oriented individual nanosheets.

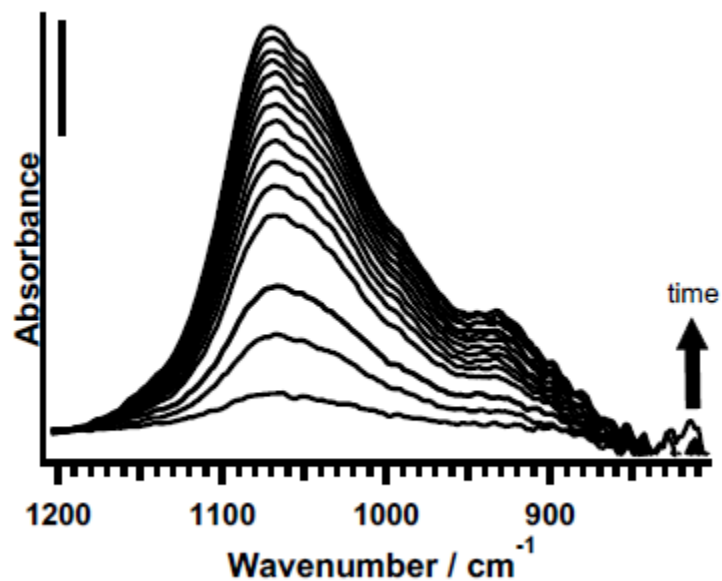**A.2.2.3. Figure A.2.3. Time-course ATR-FTIR spectra of phosphate exposure to LiCoO₂-coated ZnSe.**

Figure A.2.3. Time-course ATR-FTIR spectra of phosphate exposure to LiCoO$_2$-coated ZnSe, showing apparent equilibration after one hour of exposure. Scale bar is 0.002 a.u.

A.2.2.4. Figure A.2.4. Atomic coverage of P on LiCoO$_2$ for particles exposed to 1 mM, 10 mM and 100 mM.
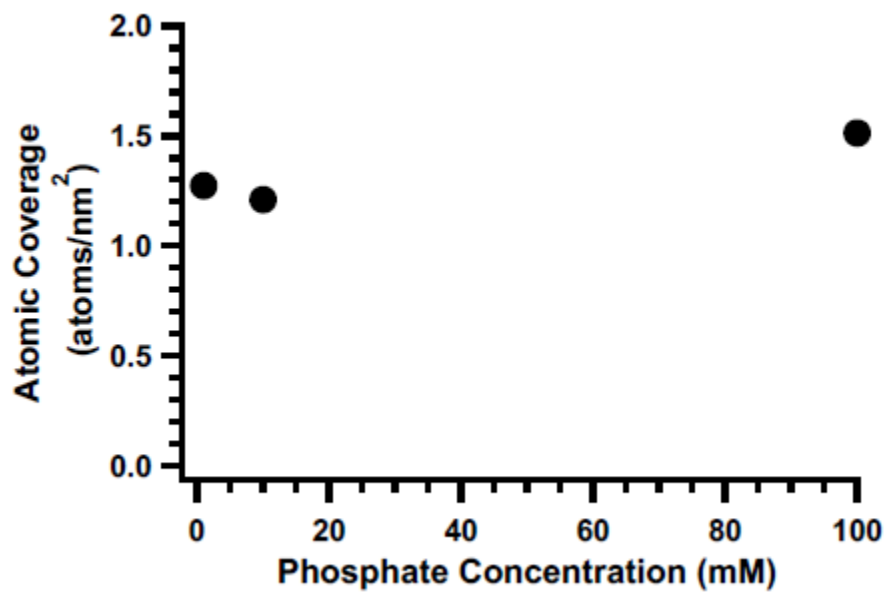
Figure A.2.4. Atomic coverage of P on LiCoO$_2$ for particles exposed to 1 mM, 10 mM and 100 mM for one hour in solution.

A.2.2.5. Figure A.2.5. SEM micrograph of LiCoO$_2$ particles following sonication described for DLS measurements.
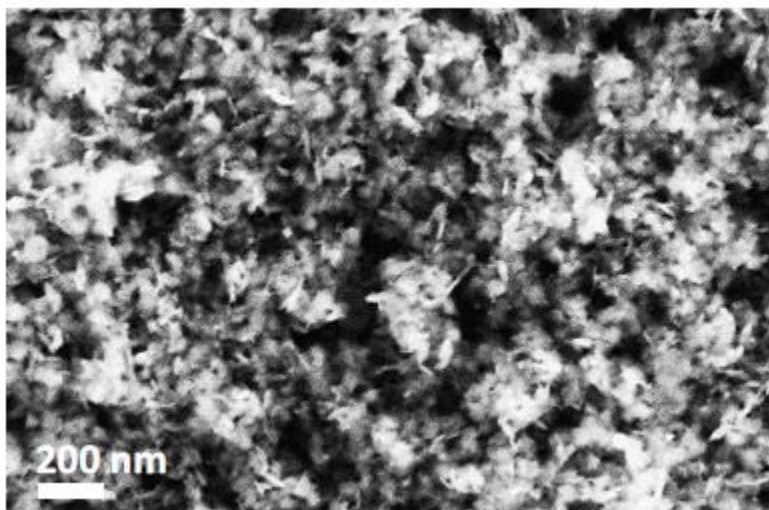
Figure A.2.5. SEM micrograph of LiCoO$_2$ particles following sonication described for DLS measurements. Individual particles are still observed and primary particle size does not seem to be impacted.

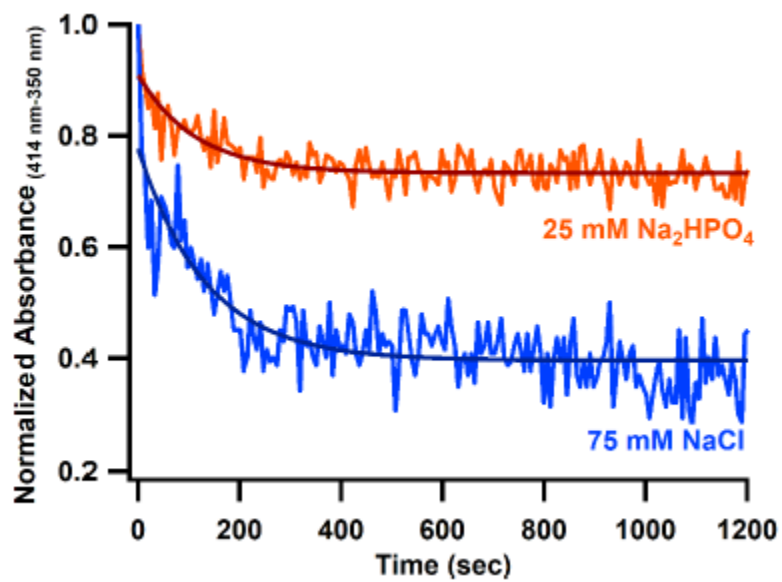**A.2.2.6. Figure A.2.6. Raw UV-Vis sedimentation plots for 25 mM Na₂HPO₄ and 75 mM NaCl.**

Figure A.2.6. Raw UV-Vis sedimentation plots for 25 mM Na₂HPO₄ and 75 mM NaCl.

A.2.3. References.

1.	Chènebault, P.; Schürenkämper, A., The Measurement of Small Surface Areas by the B.E.T. Adsorption Method. *J. Phys. Chem.* **1964,** *69* (7), 2300-2305.

2.	Wojdyr, M., *J. Appl. Cryst.* **2010,** *43*.

3.	*CasaXPS*, software version 2.3.16.

4.	Powell, C. J.; Jablonski, A. *NIST Electron Effective-Attenuation-Length Database*, version 1.3; National Institute of Standards and Technology: Gaithersburg, MD, 2011.

5.	Tanuma, S.; Powell, C. J.; Penn, D. R., Calculation of Electron Inelastic Mean Free Paths (IMFPs) VII. Reliability of the TPP-2M IMFP Predictive Equation. *Surf. Interface Anal.* **2003,** *35*, 268-275.

6.	Pettibone, J. M.; Cwiertny, D. M.; Scherer, M.; Grassian, V. H., Adsorption of Organic Acids on TiO2 Nanoparticles: Effects of pH, Nanoparticle Size, and Nanoparticle Aggregation. *Langmuir* **2008,** *24*, 6659-6667.

7.	Stebounova, L. V.; Guio, E.; Grassian, V. H., Silver nanoparticles in simulated biological media: a study of aggregation, sedimentation, and dissolution. *J Nanopart Res* **2011,** *13* (233-244), 233.

8.	Phenrat, T.; Saleh, N.; Sirk, K.; Tilton, R. D.; Lowry, G. V., Aggregation and Sedimentation of Aqueous Nanoscale Zerovalent Iron Dispersions. **2007**.

9.	Bian, S.-W.; Mudunkotuwa, I. A.; Rupasinghe, T.; Grassian, V. H., Aggregation and Dissolution of 4 nm ZnO Nanoparticles in Aqueous Environments: Influence of pH, Ionic Strength, Size, and Adsorption of Humic Acid. *Langmuir* **2011,** *27*, 6059-6068.

10.	Zhou, D.; Keller, A. A., Role of morphology in the aggregation kinetics of ZnO nanoparticles. *Water Research* **2010,** *44*, 2948-2956.

Appendix 3. Supporting information for Chapter 3: Interaction of Phosphate with Lithium Cobalt Oxide Nanoparticles: A Combined Spectroscopic and Calorimetric Study.

A.3.1. Supplemental Materials and Methods.

A.3.1.1. General.

A Thermo Scientific Sorvall Legend X1R Centrifuge with a Thermo TX-400 rotor at 4696 g was used for all centrifugation described, unless otherwise noted. All reagents were purchased from Sigma-Aldrich. Ultrapure water (18.2 MΩ/cm resisitivity) was used in all experiments.

A.3.1.2. Unit conversion for amount phosphate adsorbed to LiCoO₂ between two methods.

$$\frac{\mu mol}{mg\ LCO}P(from\ calorimetry) \times 10\ mg\ LCO \times \frac{1\ mol}{10^6\ \mu mol} \times \frac{6.022 \times 10^{23}\ atoms\ P}{1\ mol} = atoms\ P$$

$$10\ mg\ LCO \times \frac{1\ g}{10^3\ mg} \times \frac{135\ m^2}{g} \times \frac{10^{18}\ nm^2}{1\ m^2} = 1.35 \times 10^{18}\ nm^2$$

$$\frac{atoms\ P\ from\ calorimetry}{1.35\times10^{18}\ nm^2} \rightarrow \text{calorimetry data in XPS units}$$

pH	μmol P / mg LCO (Calorimetry)	Atoms P/ nm² LCO (Calorimetry)	Atoms P/ nm² LCO (XPS)
5.6	0.14	0.625	1.36
7.4	0.15	0.664	1.12
9.0	0.015	0.066	0.63

A.3.2. Additional Figures.

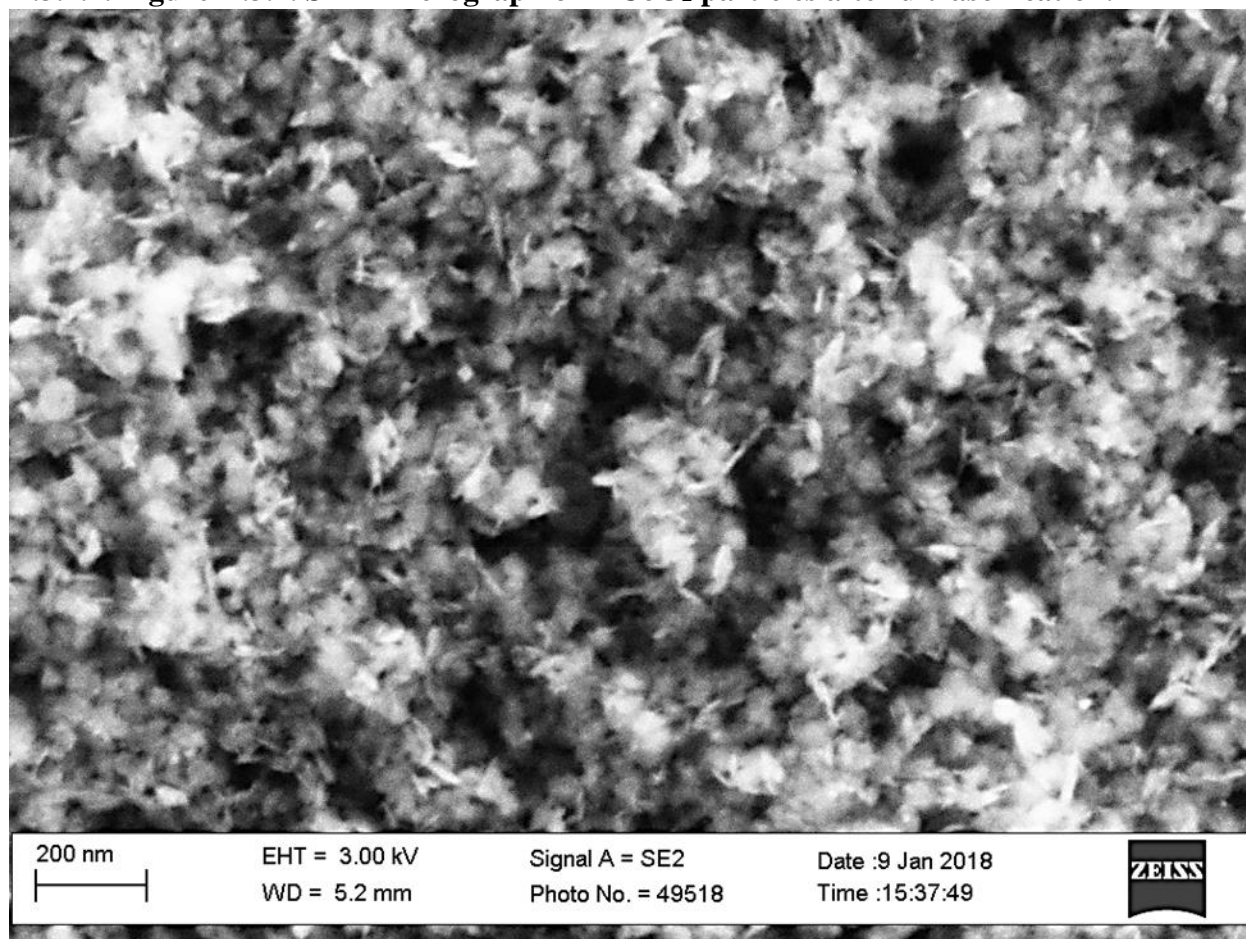**A.3.2.1. Figure A.3.1. SEM micrograph of LiCoO₂ particles after ultrasonication.**

Figure A.3.1. SEM micrograph of LiCoO₂ particles following ultrasonication described for DLS measurements and formation of nanoparticle layers for ATR-FTIR. Individual particles are still observed, and particles do not appear to have been fractured in the process.

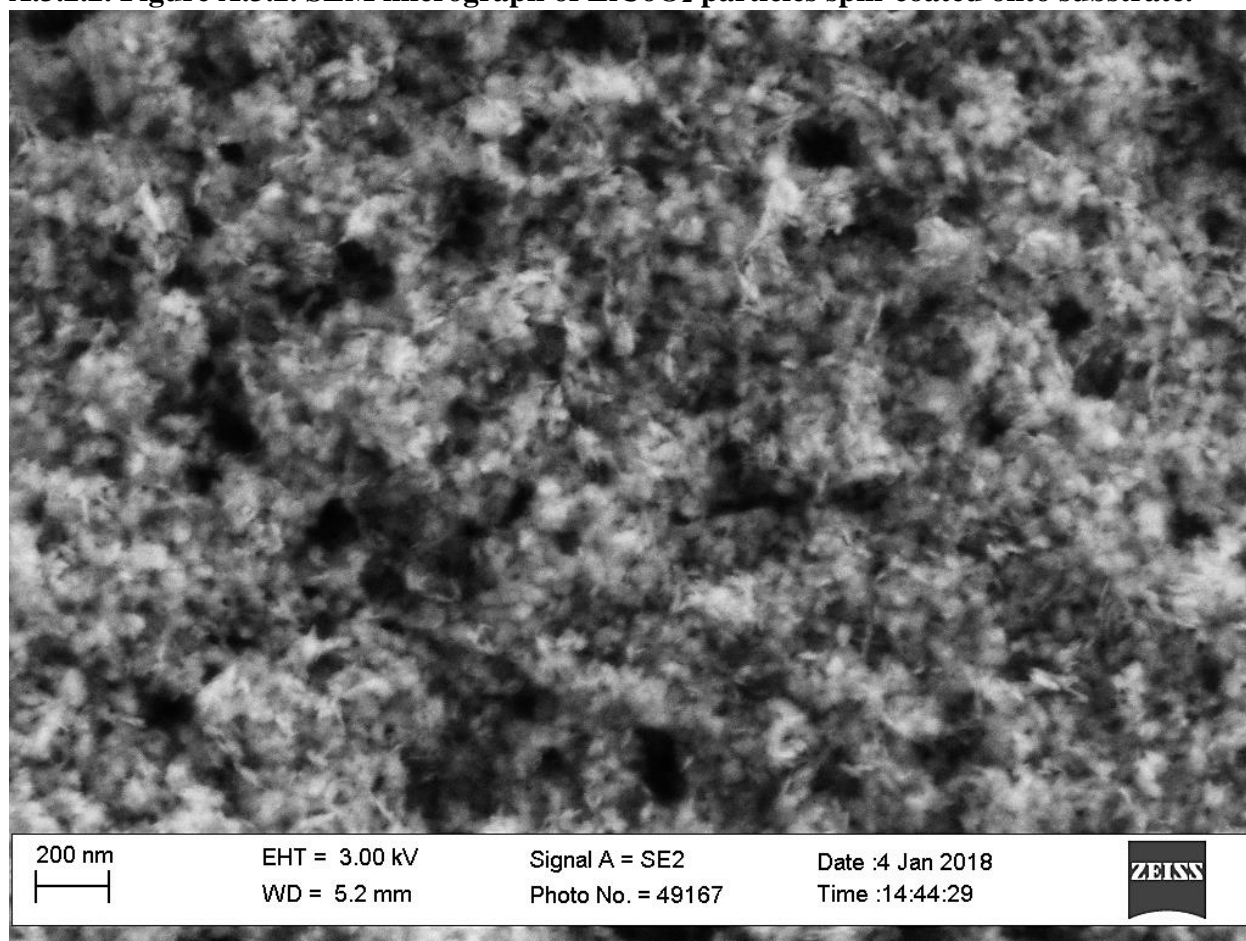**A.3.2.2. Figure A.3.2. SEM micrograph of LiCoO₂ particles spin-coated onto substrate.**

Figure A.3.2. SEM shows LiCoO₂ particles randomly orient on surfaces when applied using a spin-coater.
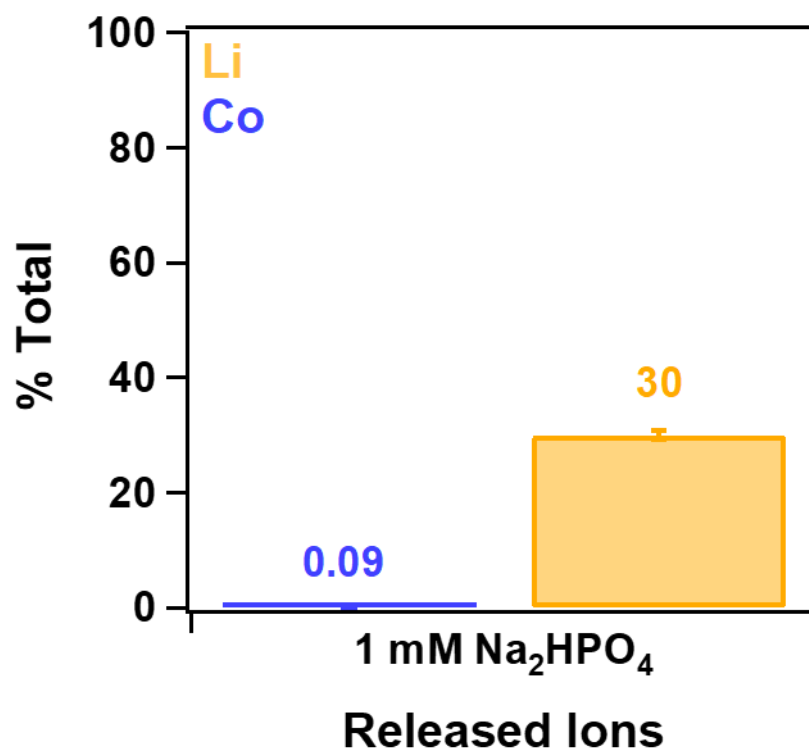
A.3.2.3. Figure A.3.3. Ion release from LiCoO$_2$ in phosphate.

Figure A.3.3. Percentage of total cobalt (blue) and lithium (yellow) ions in the material that are released from a 100 mg/L suspension of LiCoO$_2$ in 1 mM Na$_2$HPO$_4$ for 1 hour as measured with ICP-MS.
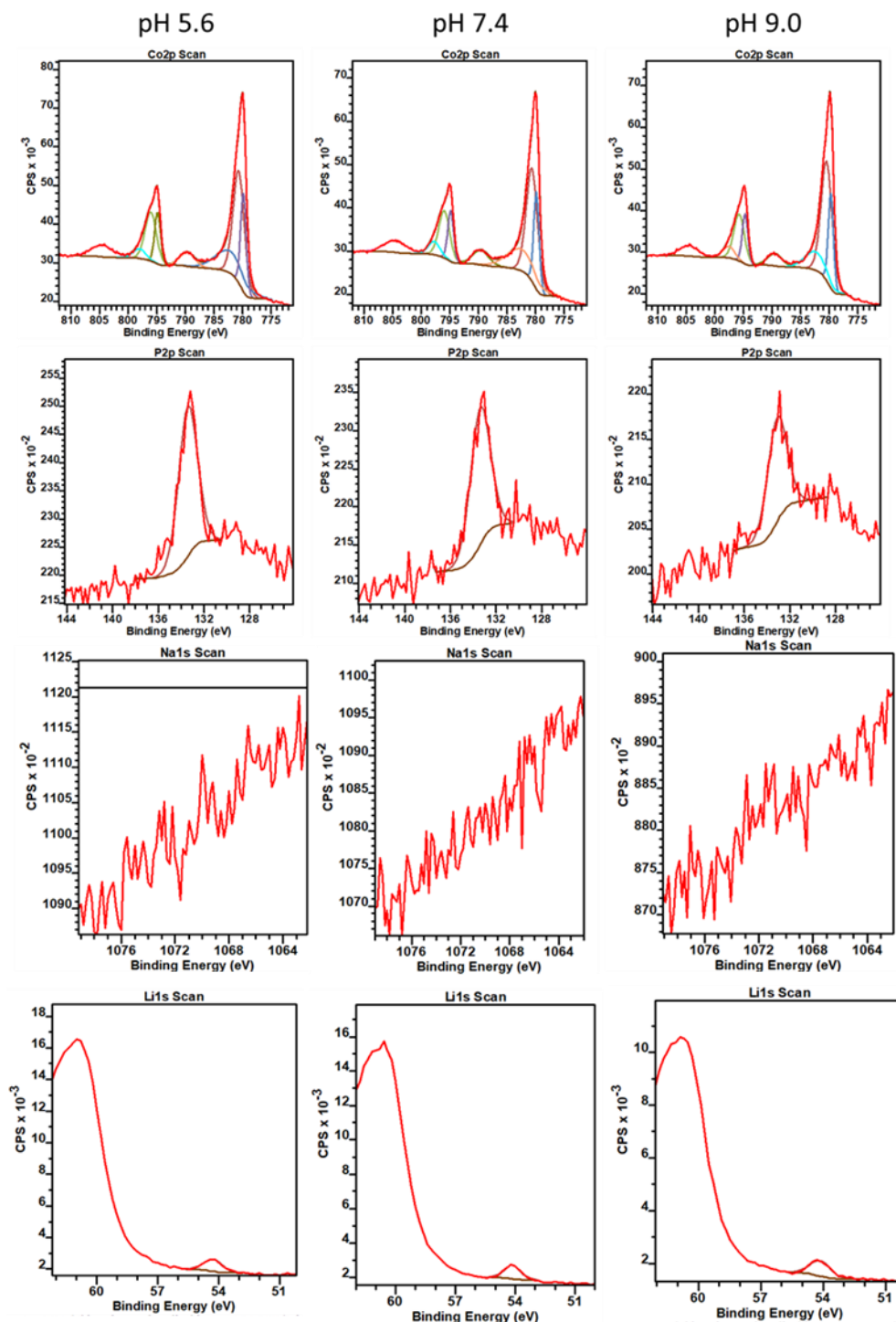
A.3.2.4. Figure A.3.4. Representative XPS spectra corresponding to coverage analysis.

Figure A.3.4. Representative XPS spectra used in the analysis of phosphate coverage on LCO as

a function of pH. There is no evidence for sodium binding to the surface. Lithium is observed in

each case, but is not used for quantification due to the likelihood of Li^+/H^+ exchange at the
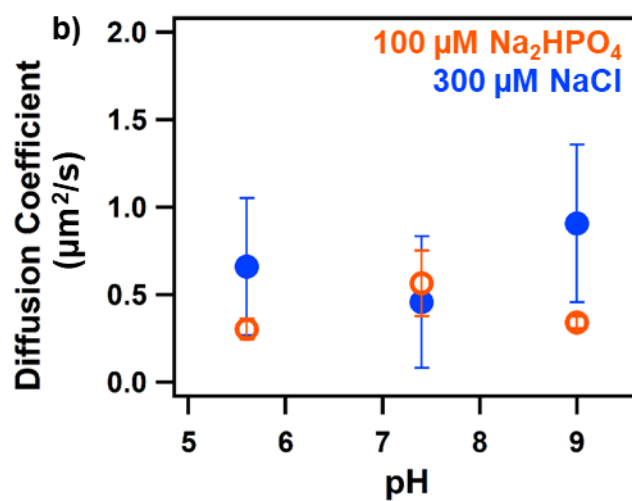
surface in water.

A.3.2.5. Figure A.3.5. Diffusion coefficients of LiCoO₂ in phosphate.

Figure A.3.5. Diffusion coefficient of LiCoO₂ nanoparticles as a function of pH in the absence and presence of phosphate.

A.3.2.6. Figure A.3.6. Time-course ATR-FTIR spectra of phosphate exposure to LiCoO$_2$.
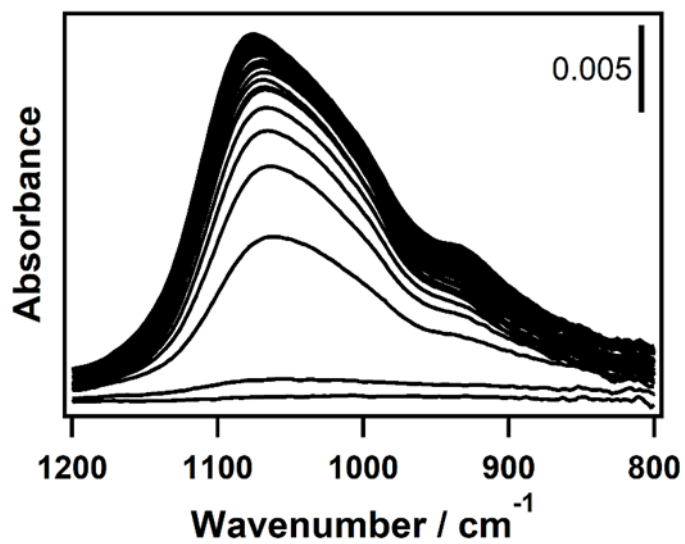

Figure A.3.6. ATR-FTIR spectra collected over the course of one hour of Na$_2$HPO$_4$ exposure to LiCoO$_2$ at pH 7.4.
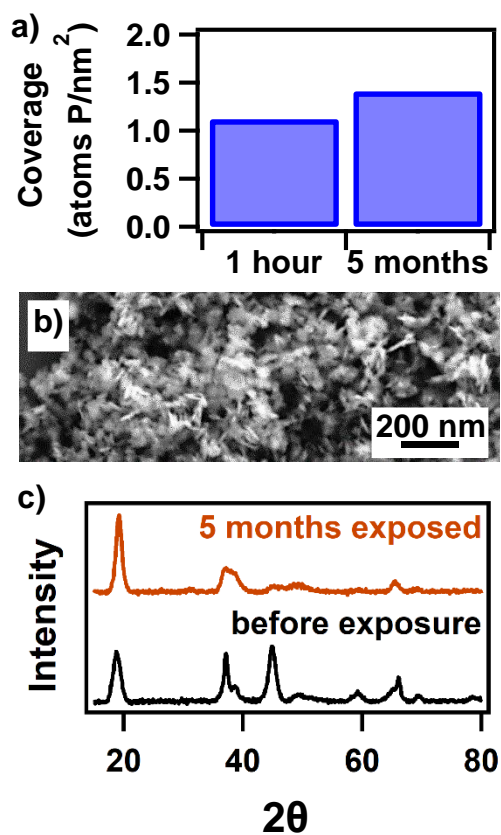
A.3.2.7. Figure A.2.7. Long-term impacts of phosphate exposure to LiCoO₂.

Figure A.3.7. Long term impacts of Na₂HPO₄ exposure to LiCoO₂ at pH 7.4. a) coverage values as determined by XPS in atoms P / nm² after one hour vs after five months. b) SEM micrograph of LiCoO₂ nanosheets after five months in Na₂HPO₄ at pH 7.4. c) XRD patterns of LiCoO₂ nanoparticles before exposure (black trace) and after five months exposure to Na₂HPO₄ at pH 7.4 (orange trace).

Appendix 4. Supporting information for Chapter 4: The Influence of Organic Acids on Lithium Cobalt Oxide Nanoparticle Dissolution and Interaction with Phosphate

A.4.1. Additional Figures.

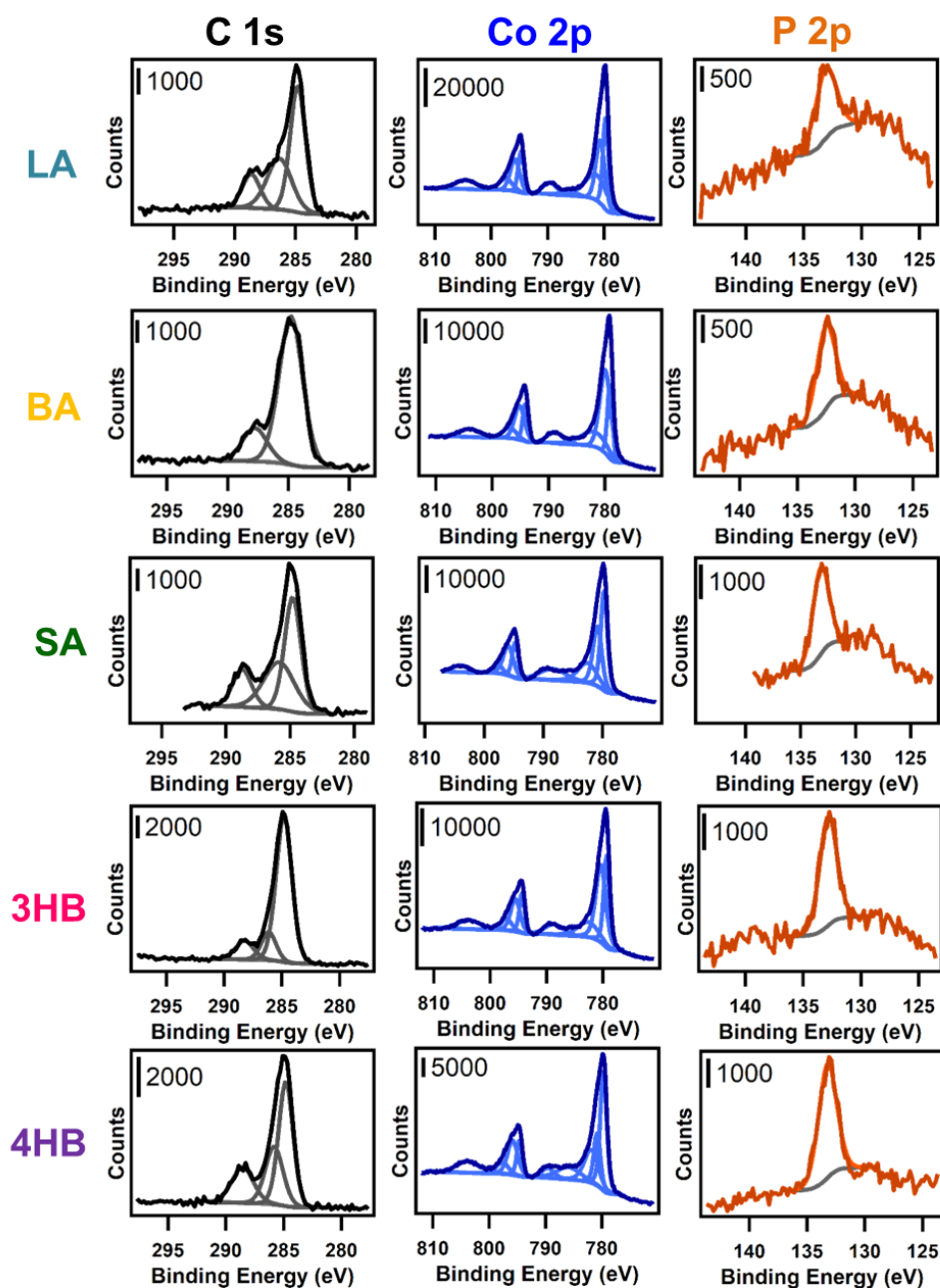*A.4.1.1. Figure A.4.1. Representative XP spectra from competitive adsorption experiments.*

Figure A.4.1. Representative XP spectra of the C(1s), Co(2p) and P(2p) regions for LiCoO$_2$ particles exposed to 1 mM Na$_2$HPO$_4$ and 1 mM of organic acid.

A.4.1.2. Figure A.4.2. Unnormalized surface coverages from XPS data for competitive adsorption experiments.
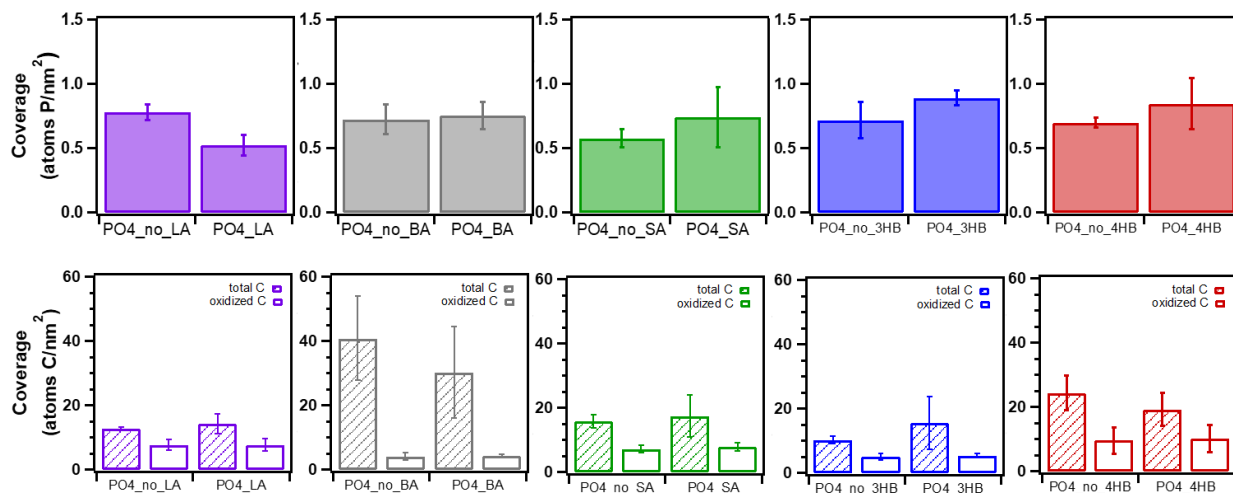

Figure A.4.2. Raw coverage values from XPS adsorption experiments. Top row, left to right: phosphorus coverage in the presence and absence of LA, BA, SA, 3HB and 4HB. Bottom row, left to right: oxidized carbon coverage (striped bars, coverage calculated solely from the 286 eV and 288.5 eV contributions) and total carbon coverage (empty bars) when exposed to phosphate in the presence and absence of LA, BA, SA, 3HB and 4HB.

A.4.1.3. Figure A.4.3. XP spectrum and calculated carbon coverage for as-synthesized LiCoO₂
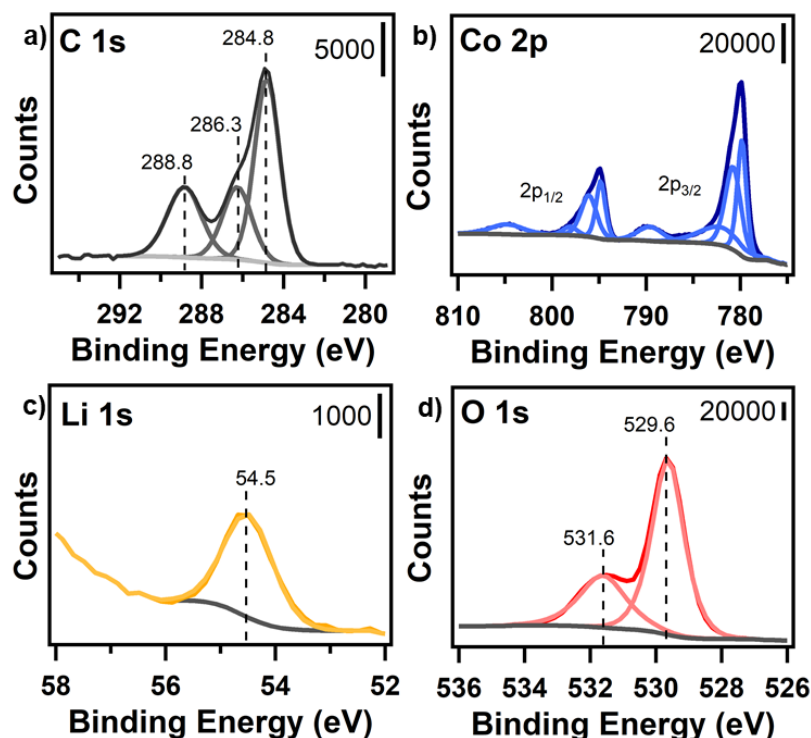
nanoparticles.

Figure A.4.3. XP spectra for the pristine, as-synthesized LiCoO₂ nanoparticles. a) C(1s) region. The peak at 284.8 eV is attributed to adventitious carbon, the peak at 286.3 eV is attributed to carbon in alcohol/ether groups, and the peak at 288.8 eV is attributed to carbon in carboxyl groups. b) Co(2p) region, showing the $2p_{3/2}$ and $2p_{1/2}$ regions and corresponding satellite peaks. The $2p_{3/2}$ and $2p_{1/2}$ peaks can be fit to three components, consistent with predominantly Co^{3+} with some Co^{4+} at the surface. c) Li(1s) region. The location of the Li(1s) peak at 54.5 eV is consistent with lithium in an octahedral environment, as expected for this material. d) O(1s) region. The peak at 529.6 eV is attributed to the O^{2-} ions in the crystal structure, and the higher binding energy peak at 531.6 eV is attributed to undercoordinated oxygen at the surface and/or from adsorbed surface species. Total

carbon coverage of as-synthesized particles is 11 atoms C/nm^2, whereas oxidized carbon coverage

(coverage calculated excluding the adventitious carbon peak) is 5.4 atoms C/nm^2.

A.4.1.4. Figure A.4.4. Concentrations in μM of Li$^+$ and Co^{2+} released from LiCoO₂ during phosphate coating.
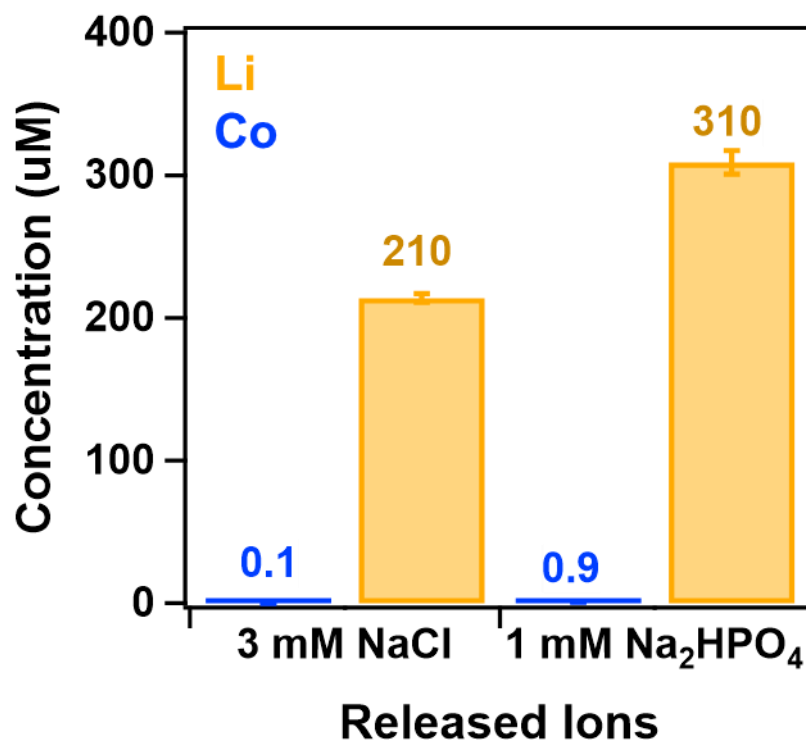

Figure A.4.4. Concentrations of Co^{2+} (blue bar) and Li$^+$ (yellow bar) released during LiCoO₂ exposure to either 3 mM NaCl or 1 mM Na₂HPO₄.

Appendix 5. Synchrotron X-ray Absorption Spectroscopy for analysis of lithium cobalt oxide nanoparticle transformation in aqueous systems: method optimization and preliminary results

A.5.1 Introduction.

A.5.1.1. Introduction to X-ray Absorption Fine Structure.

In order to develop an understanding of how nanomaterials transform in aqueous environments, we need the ability to probe these transformations as they occur using in situ analytical techniques. These transformations are often surface-mediated, as the surface is particularly reactive. By definition, the creation of a surface leads to the formation of undercoordinated surface species. The presence of water can greatly reduce the energy of these surfaces, through the formation of surface complexes that passivate dangling bonds. However, these inevitable and instantaneous transformations may have significant impact on the surface properties of these materials, rendering ex situ analysis unrepresentative of the true surface structures.[1] Traditional x-ray spectroscopy often requires the use of ultra-high vacuum, limiting its ability for in situ experiments. While samples can be prepared ex situ, this analysis tends to only provide a surface chemical snapshot of the transformed material, and is susceptible to drying artifacts including changes to coatings, surface oxidation, loss of hydration information, and more.

In situ x-ray spectroscopy experiments are possible through the use of synchrotron light sources. Synchrotron light sources accelerate traveling electrons to >99.999999% the speed of light by focusing electrons into a narrow beam bent on a circular path using an electromagnetic field. X-rays emitted from this beam of focused electrons are extremely bright, allowing for various x-ray techniques to be applicable to samples outside of vacuum. X-ray Absorption Fine Structure (XAFS) experiments are a way to examine the modulations of x-ray absorption probability as a function of photoelectron scattering. Near Edge X-ray Absorption Fine Structure (NEXAFS) experiments can elucidate the formal valence, coordination, hybridization, band structure and oxidation states of atoms in a material. The half-height of the pre-edge peak in the NEXAFS region of spectra corresponds to the formal valence state, which can be determined through comparison to reference samples.[2] Extended X-Ray Absorption Fine Structure (EXAFS) can elucidate the determination of the number, distance, and identity of neighboring atoms to the absorbing atom.[3] While these are bulk techniques, they can be made more surface sensitive by being performed in a fluorescence geometry, or by increasing the surface area to volume ratio of the sample. The latter makes nanomaterials ideal samples for surface analysis using XAFS.

A.5.1.2. in situ X-Ray Absorption Fine Structure of metal oxides.

XAFS has been used to characterize oxidation state changes as a function of pH,[4] assign coordination geometries of adsorbates on the surface of minerals,[5] and also assign the identity of adsorbates onto surfaces from solution.[6] XAFS provides a tool to characterize the native structure of nanomaterials, allowing for the confirmation of both crystal structure and surface functionality. This could be particularly useful to provide experimental values to corroborate theoretical predictions, and confirm the successful synthesis of new materials such as $LiFe_{1/3}Mn_{1/3}Al_{1/3}O_2$. In addition to providing powerful analysis of the native structures of our nanomaterials, it also opens

the door for deeper analysis of the materials in solution and subsequent transformations. These techniques can be used to assess the hydration of the materials in solution, the surface functionalization and lithiation state, the oxidation state of the metals at the surface and how they change as the material dissolves, and the identity and geometry of adsorbates on the surface. Because the complex metal oxide nanosheets tend to be approximately 10 atomic layers thick, the surface represents about 20% of the material, and therefore about 20% of the signal will come from the surface as opposed to the bulk material. The surface sensitivity could be enhanced by synthesizing thinner materials or developing a procedure to exfoliate single or few layers of the material for these experiments.

A.5.1.3. Extended X-ray Absorption Fine Structure Theory.

The EXAFS region is characterized by its modulating absorption probability as a function of energy past the absorption edge. Core electrons from elements have a characteristic binding energy on the energy scale of x-rays. When irradiated with an x-ray with energy corresponding to that binding energy, the core electron can be ejected and emitted as a photoelectron. The photoelectron radiates outward from the absorbing atom, and has the ability to scatter elastically off of a neighboring atom and radiate back towards the initial absorbing atom.

As Fermi's Golden Rule explains, the more similar the initial and final states, the more likely that a process will occur. The initial state is the atom with the core electron, while the final state is the atom, core hole, and photoelectron. When the photoelectron elastically scatters back towards the absorbing atom, the final state more closely resembles the initial state, with the photoelectron density returning to the absorbing atom. At this point, the absorption probability increases, which is exemplified by the modulations in the EXAFS plot of absorption probability as a function of time. The probability of x-ray absorption is enhanced if it leads to constructive

interference of the ejected electron at the location of the absorbing atom, which is the case when the round trip distance back from the neighboring atom is a whole number of wavelengths, satisfying the equation:

$$2D = n\lambda \qquad \text{(Equation 1)}$$

The photoelectron can be modeled as a plane (sinusoidal) wave,

$$\sin(2\pi \frac{2D}{\lambda}) \qquad \text{(Equation 2)}$$

The EXAFS, defined χ, is proportional to the plane wave. Converting wavelength to wavenumbers using:

$$k = \frac{2\pi}{\lambda} \qquad \text{(Equation 3)}$$

this relationship can be simplified to

$$\chi \, \alpha \, \sin(2kD). \qquad \text{(Equation 4)}$$

Which shows that the spacing of the EXAFS oscillations is a function of atomic distance and wavenumber, and therefore, energy. This equation is a simplification, as there are a number of experimental factors to consider when the actual EXAFS phenomenon is taking place. Equation 5 is also known as "The EXAFS Equation", which includes all the variables that impact the EXAFS phenomenon for an absorbing atom.

$$\chi(k) = S_o^2 \sum_i N_i \frac{f_i(k)}{kD_i^2} e^{\frac{2D_i}{\lambda(k)}} e^{-2k^2\sigma^2} \sin(2kD_i + \delta_i(k)) \qquad \text{(Equation 5)}$$

S_o^2 is a scaling factor to account for incomplete overlap; even with photoelectron scattering, the initial and final state are not exactly the same, as there is still the presence of a core hole. This scaling factor cannot be experimentally derived but is instead approximated in the modeling and

analysis. The EXAFS equation is represented as a sum, as many atoms (N_i) can interact with the photoelectron, and the resulting spectrum is a sum of all of those interactions. $f_i(k)$ is proportional to the possibility of inelastic scattering, which will change the energy of the photoelectron and therefore the similarity between initial and final states. kD_i^2 adjusts for the fact that photoelectrons emit as spherical waves, and therefore the scattering probability drops off as the square of the distance. $e^{\frac{2D_i}{\lambda(k)}}$ adjusts for the mean free path of the emitted photoelectron and core hole filling. A photoelectron can only travel so far before inelastically scattering and imparting its energy. There is also the possibility that when the photoelectron returns to the absorbing atom, it can be reabsorbed and fill the core hole, thus ending the EXAFS phenomenon. The core hole filling and inelastic mean free path adjustments define EXAFS as a local phenomenon; scattering off of atoms more distant than 10 Å from the absorbing atom is negligible. The $e^{-2k^2\sigma^2}$ term accounts for the fact that EXAFS is an average, and there will be a variation in D due to the disorder of atoms in the material. The last variable, $\delta_i(k)$, accounts for the phase shift of the wave that can occur after interaction.

One outcome of the expanded EXAFS equation is the ability to determine atomic identity from EXAFS oscillations. $\delta_i(k)$ and $f_i(k)$ are element specific, and so the identity of neighboring atoms can be extracted from this equation.

A.5.2 Materials and Methods.

A.5.2.1. Nanoparticle synthesis and characterization.

We synthesized sheet-like nanoparticles of Li_xCoO_2 as described previously.[7-9] We synthesized a $Co(OH)_2$ precursor by dropwise addition of 1 M $Co(NO_3)_2{\cdot}6H_2O$ to 0.1 M LiOH. We isolated the precipitate by centrifuging into a pellet and decanting the supernatant. We washed

the pellet by redispersion in water, centrifugation and removal of supernatant a total of three times. We dried the product in a vacuum oven at 30 $^{\circ}$C overnight. To convert Co(OH)$_2$ to Li$_x$CoO$_2$, the Co(OH)$_2$ precursor was added to a molten salt flux of LiNO$_3$:LiOH in a 6:4 molar ratio. We prepared the molten salt flux by heating the mixture at 200 $^{\circ}$C in a polytetrafluoroethylene container with magnetic stirring. After the precursor had reacted in the flux for 30 min, we quenched the reaction with water and washed/isolated the precipitate through four cycles as described above. The product was then dried in a vacuum oven at 30 $^{\circ}$C overnight.

A.5.2.2. Chemical characterization of Li$_x$CoO$_2$ nanoparticles.

We obtained powder x-ray diffraction (XRD) patterns of the Li$_x$CoO$_2$ nanoparticles with a Bruker D8 Advance powder diffractometer. We prepared concentrated dispersions of LCO powders in isopropyl alcohol by ultrasonication in a cup sonicator. We drop-cast the suspension onto a zero-diffraction plate and allowed it to dry. The powder XRD pattern was acquired from 15 to 80 $^{\circ}$ 2θ using a step size of 0.20 $^{\circ}$ and dwell time of 166 s at each point.

For morphology characterization with scanning electron microscopy (SEM), we prepared dilute dispersions of LCO in methanol and drop-cast the dispersions onto low-resistivity boron-doped silicon wafers. Micrographs were acquired with a Leo Supra55 VP SEM at 3 kV electron energy using a secondary electron detector.

A.5.2.3. Preparation of ex situ samples for XAS analysis.

We prepared ex situ nanoparticle samples for analysis by making pellets of LiCoO2 mixed with boron nitride (BN). The absorption length of LiCoO$_2$ is ~ 5 mg/cm^2, and our pellet press was 0.7 cm in diameter, so loadings of 1.8 mg LiCoO$_2$ were used for each pellet. A stock powder of 18 mg LiCoO$_2$ and 511 mg BN was mixed with a mortar and pestle. 50 mg of the mixture was used

to prepare each pellet. The pellets were mounted inside holes in Teflon spacers and covered on either side with Kapton tape.

A.5.2.4. Preparation of in situ samples for XAS analysis.

We prepared 12.5 mg/mL suspensions of $LiCoO_2$ nanoparticles in analyte solutions of interest by weighing out 25 mg of nanoparticles and adding to 2 mL of solution. The mixture was sonicated briefly to disperse the particles. The suspension was transferred into in situ cells with a 2 mm pathlength fitted with magnetic stir bars, as shown in Figure A.5.1.

A.5.2.5. Data acquisition.

Data acquisition conditions were optimized to the Co K-edge at 7708 eV. The intensity of the beam, I0, and intensity after transmission through the sample, IT, were optimized for each sample. IT is highest before the edge, and lowest after the edge. The amplifier settings were adjusted so that IT is between 0.2 and 4.5 both below the edge (100 eV less than onset energy) and above the edge (100 eV higher than onset energy). The sensitivity (in A/V) and offset (pA) can be adjusted to ensure optimal conditions for both above and below the edge. The offset should always be 10% of the sensitivity. For most of the data described here, the amplifier was set at 2 nA/V sensitivity and 200 pA offset.

Each sample was then scanned horizontally and vertically to ensure uniform signal across the sample. Horizontal and vertical scans were taken at 7725 eV, an after confirming uniformity of the sample, a center point in both the X and Y direction was chosen for data acquisition, as shown in Figure A.5.2.

The acquisition conditions were set as follows: Pre edge acquisition beginning at -200 eV before the edge, 5 eV per step, 2 s integration time; XANES acquisition beginning at -15 eV before

the edge, 0.2 eV per step, 2 s integration time; EXAFS acquisition beginning at 40 eV after the edge, 0.05 k per step, 2 s integration time, with no k-weighting. Due to the noise levels seen in the EXAFS data presented here, in the future, adding k-weighting would be advised, as noise increases as a function of k.

A.5.2.6. Data processing.

Data were analyzed using the Demeter XAS Data Processing and Analysis package, which is available for free online. The raw spectrum files were imported into the Athena program for normalization. The onset energy was defined as a fraction of the edge step.

A.5.3 Results and Discussion.

A.5.3.1. ex situ characterization of cobalt oxidation state from NEXAFS.

The NEXAFS region can provide information about the oxidation state in $LiCoO_2$. Previously, researchers have examined the NEXAFS region of $LiCoO_2$ during battery cycling or chemical delithiation to see how the spectra change.[2, 10-15] The pre-edge peak around 7710 eV shifts to higher energy when there is Co^{4+} present in the sample, and the intensity of this pre-edge peak is indicative of local structural distortion. The lack of shoulder peak at around 7720 eV is also often seen in conjunction with the presence of Co^{4+} in the material.

Figure A.5.3. shows the NEXAFS region of the cobalt K-edge absorption peak for $LiCoO_2$ nanoparticles (gray), commercial $LiCoO_2$ bulk material (black), aqueous Co^{2+} (pink), and $Co(OH)_2$ nanoparticles (brown). The edge onset energy for both the nano and bulk $LiCoO_2$ samples is consistent with Co^{3+} being the major species, while for Co^{2+} in solution and the $Co(OH)_2$ particles, the edge onset energy is consistent with Co^{2+}. The inset shows the pre-edge feature on a larger scale. The pre-edge peak is more intense and at higher energy for $LiCoO_2$ than Co^{2+} and $Co(OH)_2$, consistent with the presence of Co^{4+} species. The pre-edge peak is also more intense for the $LiCoO_2$

nanoparticles than the LiCoO$_2$ bulk, potentially indicating that there are more Co^{4+} species in the nanoparticles than the bulk. This is consistent with the LiCoO$_2$ nanoparticles having a larger surface area and therefore more undercoordinated species at the surface.

The pre-edge peak energy and edge onset energy are plotted as a function of expected primary oxidation state of cobalt in the material in Figure A.5.4. There is a clear trend towards higher pre-edge peak energy and edge onset energy as the cobalt oxidation state increases.

This data confirms that the LiCoO$_2$ nanoparticles synthesized contain cobalt in predominantly the Co^{3+} oxidation state, with Co^{4+} likely on the surface. The comparison between the bulk commercial LiCoO$_2$ material and our synthesized material are in good agreement, consistent with the materials being of the same structure. This technique can be used as an additional way to corroborate structural characterization of complex metal oxide nanomaterials.

A.5.3.2. in situ characterization of cobalt oxidation state from NEXAFS.

Figure A.5.5. compares the NEXAFS region of LiCoO2 nanoparticles ex situ (gray), LiCoO$_2$ bulk ex situ (black), and LiCoO$_2$ nanoparticles in water (blue). The in situ spectrum of LiCoO$_2$ nanoparticles in water almost exactly tracks the ex situ spectrum of LiCoO$_2$ nanoparticles, except that there is more noise, possibly due to the conditions of the in situ experiment. This data is good confirmation that the structure of LiCoO$_2$ nanoparticles does not change significantly when put into solution.

Figure A.5.6 shows the NEXAFS and EXAFS region of the spectrum for LiCoO$_2$ nanoparticles in gure A.5.6. NEXAFS and early EXAFS region of LiCoO$_2$ ex situ (gray), in water (blue), in 30 mM NaCl (purple), and in bacterial growth medium (green). Increasing solution complexity tends to result in an increase of noise, but not in a linear fashion; the bacterial growth

medium is a very complex aqueous system, however the spectrum of $LiCoO_2$ in this medium is less noisy than the one in 30 mM NaCl. This suggests that both solution complexity and the resulting dispersibility of the particles in that solution play a role in the noise level of the spectra.

Understanding the factors causing the noise level in these spectra will be important to be able to obtain meaningful data from the in situ experiments. The noise level in the EXAFS region is a particular concern, as the noise is amplified in the EXAFS analysis process. The EXAFS region is background subtracted and scaled by k^2, therefore the noise is amplified at high values of k (wavenumber), as shown in Figure A.5.7.

For the in situ samples studied that did not result in spectra too noisy to analyze, the changes to the edge onset energy of the NEXAFS region can give indication of the oxidation state changes of cobalt in the sample. Figure A.5.8. shows the edge onset energy (black markers, left axis) and the difference between the edge onset energy in that sample versus the dry material (red markers, right axis). $LiCoO_2$ in phosphate solutions showed edge onsets shifted to lower onsets, with larger shifts in higher concentrations. The shift in the edge onset energy is not as significant in water or NaCl. The shift in edge onset to lower energy suggests that more of the cobalt in the sample is in the 2+ oxidation state. This may be a function of the materials dissolving in the presence of phosphate, increasing the concentration of Co^{2+} in the sample. To corroborate this, future studies of $LiCoO_2$ in solutions known to enhance dissolution should be done.

A.5.4 Conclusions.

In situ x-ray absorption spectroscopy techniques such as NEXAFS and EXAFS have significant potential for use in the analysis of chemical transformations of nanomaterials in aqueous environments. These preliminary studies demonstrate the ability to obtain NEXAFS and EXAFS data from the Co K edge of cobalt in $LiCoO_2$ and related materials. Ex situ results provide

evidence of the predominantly Co^{3+} species in $LiCoO_2$, while also suggest more Co^{4+} as opposed to its bulk counterpart, consistent with an increased surface sensitivity of the measurement when nanomaterials are used. In situ experiments suffered from complications due to particle dispersibility and solution complexity, adding noise to the data. In the future, it will be necessary to reduce the impact of these variables to obtain useful and analyzable data. Some options would be to create an immobilized sample of particles within a mesh and expose it to solution, which reduce the volume of solution needed and eliminate the impacts of dispersion. Another option would be to measure the samples in fluorescence mode as opposed to transmission, as uniform thickness is not required in this method, and it is also more surface sensitive than transmission.
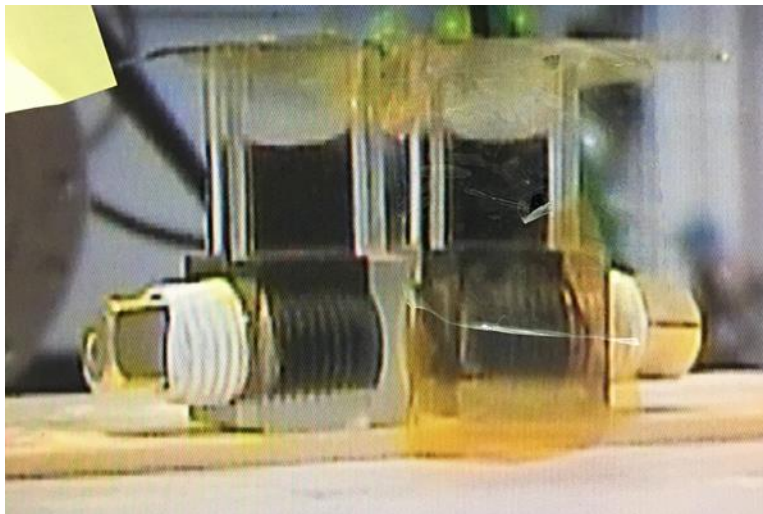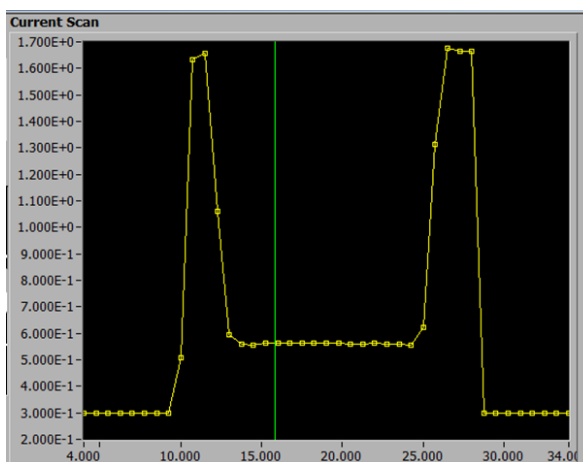
A.5.5 Figures.

Figure A.5.1. Image of the in situ cells designed for these experiments. The cells are held upright on a magnetic stir plate. The stir bar is inserted through the bottom opening, which is then sealed with a screw covered in Teflon tape. The solution is loaded through the top opening using a pipette. The volume in each cell is 2 mL. The spectra were taken from the upper part of the solution.
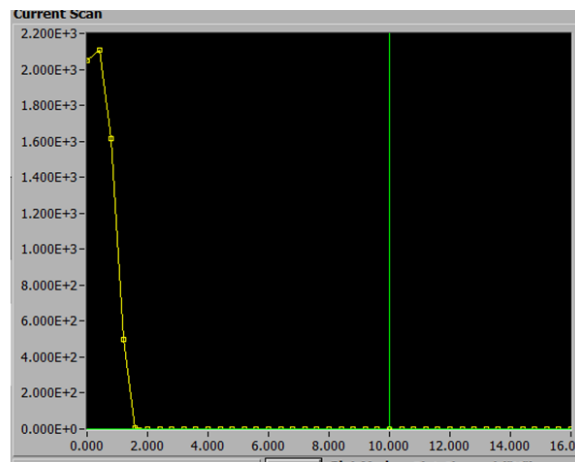
Figure A.5.2. Left: absorption of the sample vs. horizontal location right above the Co K-edge. Absorption is homogeneous across the liquid sample in the horizontal direction, as seen in the region from ~14 to ~24 on the x-axis. Right: transmission of the sample vs. vertical location right above the Co K-3dge. Absorption is homogeneous across the liquid sample in the vertical direction, as seen from the transmission being at 0 across the vertical volume of the sample. Horizontal and vertical scan locations are then chosen, as shown by the green bar in each plot.
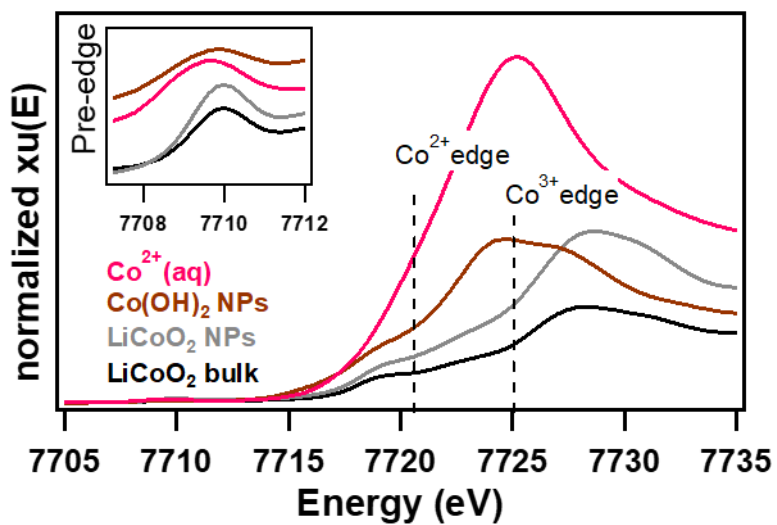
Figure A.5.3. NEXAFS spectra for bulk ex situ materials, Co^{2+} in solution (pink), $Co(OH)_2$ nanoparticles (brown), $LiCoO_2$ nanoparticles (gray), and bulk commercial $LiCoO_2$ particles (black). The edge onset energy for Co^{2+} and Co^{3+} is indicated. Inset: zoom-in on the pre-edge feature.
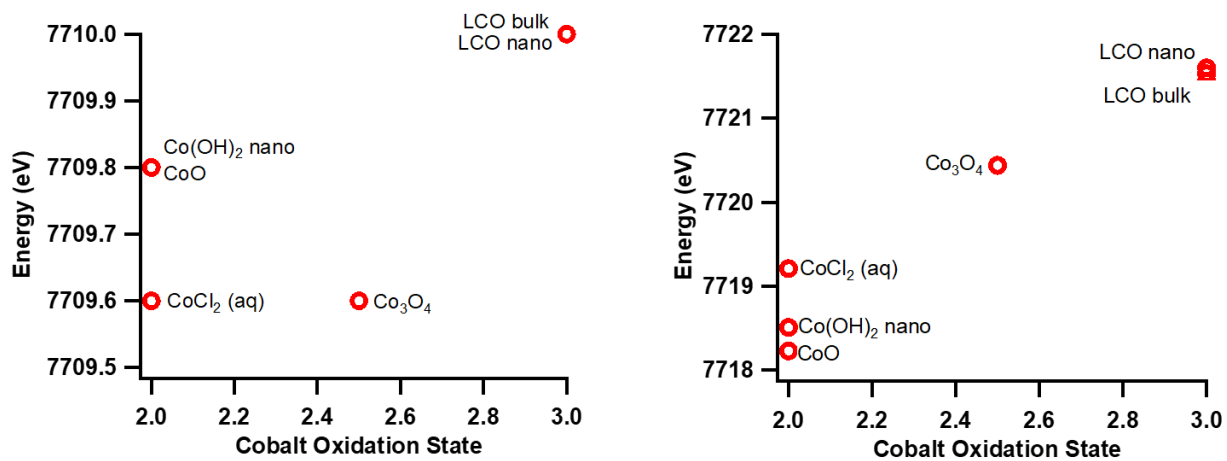
Figure A.5.4. Left: pre-edge peak energy versus cobalt oxidation state for materials measured ex situ. Right: edge onset energy versus cobalt oxidation state for materials measured ex situ.
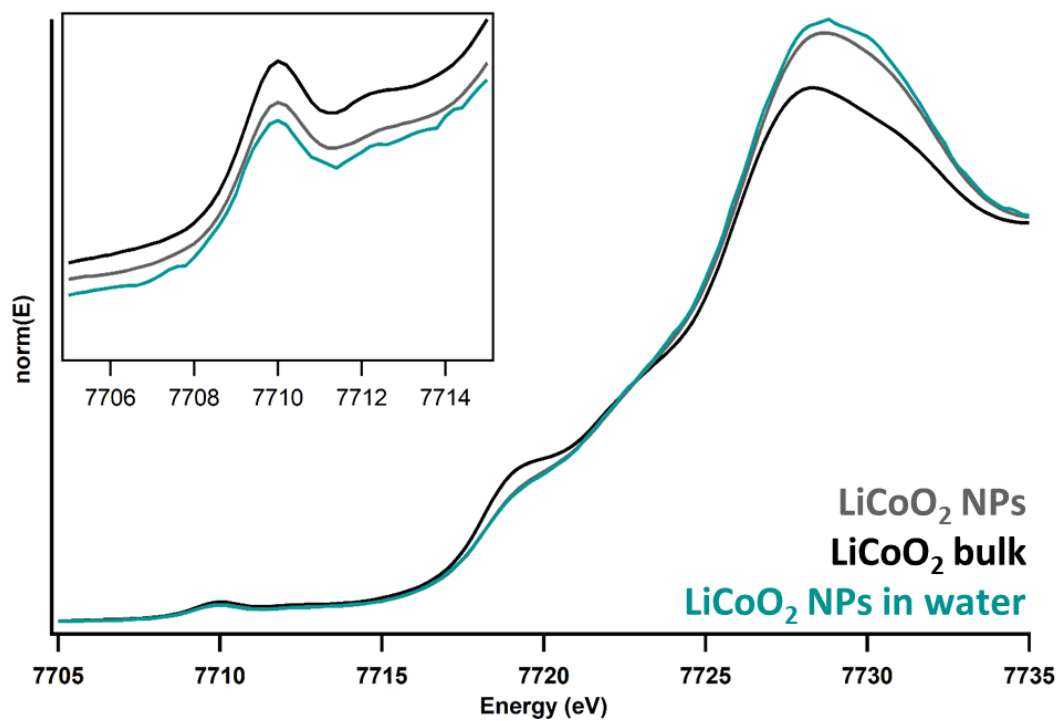
Figure A.5.5. NEXAFS spectra for LiCoO$_2$ nanoparticles (gray), and bulk commercial LiCoO$_2$ particles (black) ex situ, and LiCoO$_2$ nanoparticles in water, in situ (blue). Inset: zoom-in on the pre-edge feature.
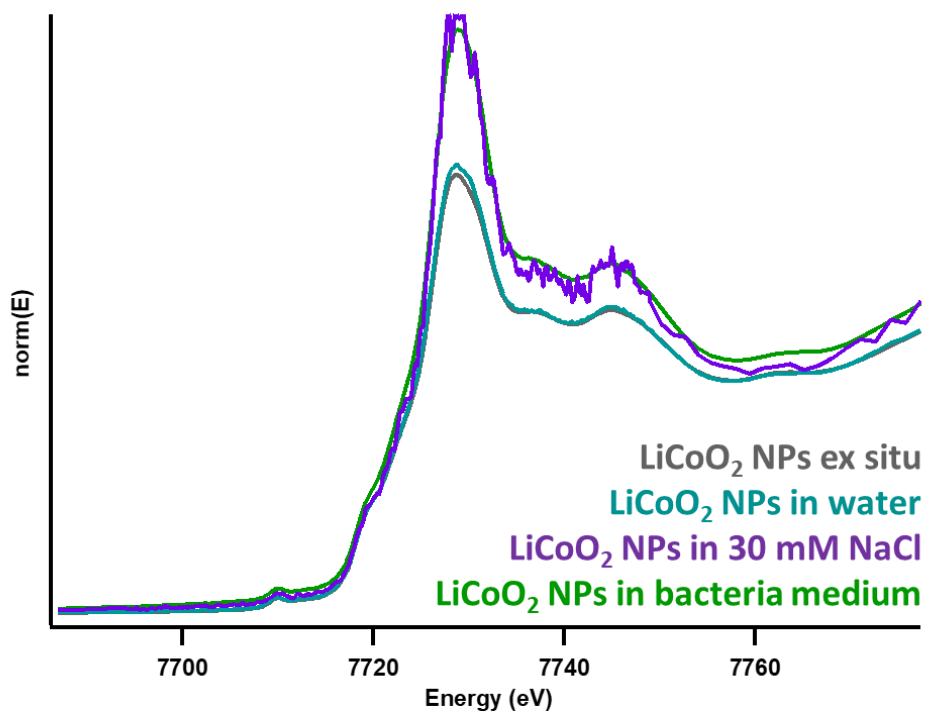
Figure A.5.6. NEXAFS and early EXAFS region of $LiCoO_2$ ex situ (gray), in water (blue), in 30

mM NaCl (purple), and in bacterial growth medium (green).
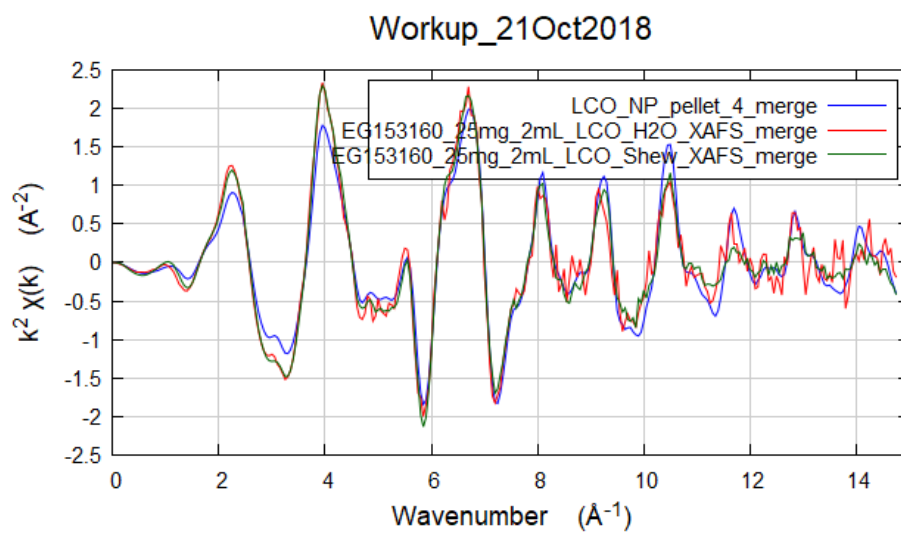
Figure A.5.7. Analysis of the EXAFS region for in situ samples shows that the noise level is too high to extract information.
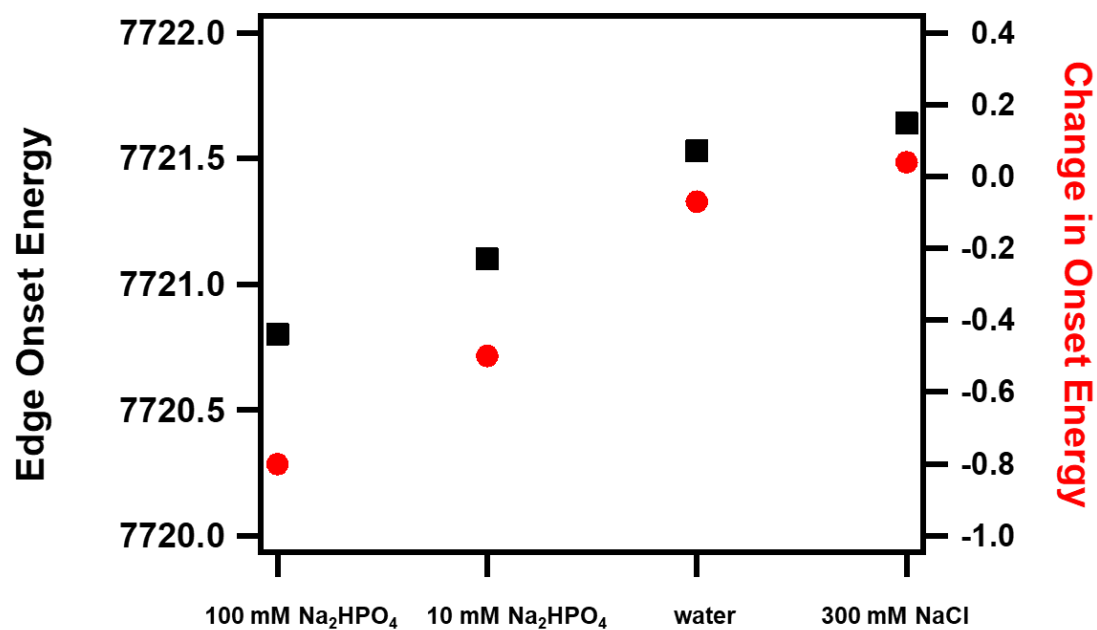
Figure A.5.8. Edge onset energy and shift in edge onset energy from ex situ LiCoO2 for LiCoO2 in 100 mM Na2HPO4, 10 mM Na2HPO4, pure water, and 300 mM NaCl. The phosphate solution has more of an impact on edge onset, shifting to lower energies.

A.5.6 References.

1.   Fenter, P.; Sturchio, N. C., Mineral–water interfacial structures revealed by synchrotron X-ray scattering. *Progress in Surface Science* **2004,** *77*, 171-258.

2.   Ito, A.; Sato, Y.; Sanada, T.; Hatano, M.; Horie, H.; Ohsawa, Y., In situ X-ray absorption spectroscopic study of Li-rich layered cathode material Li[Ni0.17Li0.2Co0.07Mn0.56]O2. *Journal of Power Sources* **2011,** *196*, 6828-6834.

3.   Tsai, Y. W.; Hwang, B. J.; Ceder, G.; Sheu, H. S.; Liu, D. G.; Lee, J. F., In-Situ X-ray Absorption Spectroscopic Study on Variation of Electronic Transitions and Local Structure of LiNi1/3Co1/3Mn1/3O2 Cathode Material during Electrochemical Cycling. *Chem. Mater.* **2005,** *17*, 3191-3199.

4.   Guénet, H.; Davranche, M.; Vantelon, D.; Pédrot, M.; Al-Sid-Cheikh, M.; Dia, A.; Jestin, J., Evidence of organic matter control on As oxidation by iron oxides in riparian wetlands. *Chemical Geology* **2016,** *439*, 161-172.

5.   Sowers, T. D.; Harrington, J. M.; Polizzotto, M. L.; Duckworth, O. W., Sorption of arsenic to biogenic iron (oxyhydr)oxides produced in circumneutral environments. *Geochimica et Cosmochimica Acta* **2017,** *198*, 194-207.

6.   Rose, J.; Flank, A.-M.; Masion, A.; Bottero, J.-Y.; Elmerich, P., Nucleation and Growth Mechanisms of Fe Oxyhydroxide in the Presence of PO4 Ions. 2. P K-Edge EXAFS Study. *Langmuir* **1997,** *13*, 1827-1834.

7.   Chen, H.; Grey, C. P., Molten Salt Synthesis and High Rate Performance of the ''Desert-Rose'' form of LiCoO2**. *Advanced Materials* **2008,** *20*, 2206-2210.

8.   Laudadio, E. D.; Bennett, J. W.; Green, C. M.; Mason, S. E.; Hamers, R. J., Impact of Phosphate Adsorption on Complex Cobalt Oxide Nanoparticle Dispersibility in Aqueous Media. *Environ. Sci. Technol.* **2018,** *52*, 10186-10195.

9.   Laudadio, E. D.; Ilani-Kashkouli, P.; Green, C. M.; Kabengi, N. J.; Hamers, R. J., Interaction of Phosphate with Lithium Cobalt Oxide Nanoparticles: A Combined Spectroscopic and Calorimetric Study. *Langmuir* **2019,** *35* (50), 16640-16649.

10.   Kim, D.-S.; Sohn, J.-S.; Lee, C.-K.; Lee, J.-H.; Han, K.-S.; Lee, Y.-I., Simultaneous separation and renovation of lithium cobalt oxide from the cathode of spent lithium ion rechargeable batteries. *Journal of Power Sources* **2004,** *132* (1-2), 145-149.

11.   Kim, J.-J.; Ryu, K. H.; Sakaue, K.; Terauchi, H.; Yo, C. H., Structural characterization for the chemically Li+ ion extracted LiyCoO2, LiyCo0.95Ga0.05O2, and LiyCo0.9Ga0.1O2 compounds. *Journal of Physics and Chemistry of Solids* **2002,** *63*, 2037-2045.

12.   Kim, M. G.; Yo, C. H., X-ray Absorption Spectroscopic Study of Chemically and Electrochemically Li Ion Extracted LiyCo0.85Al0.15O2 Compounds. *J. Phys. Chem. B* **1999,** *103*, 6457-6465.

13.   Chae, B.-M.; Oh, E.-S.; Lee, Y.-K., Conversion mechanisms of cobalt oxide anode for Li-ion battery: In situ X-ray absorption fine structure studies. *Journal of Power Sources* **2015,** *274*, 748-754.

14.   Alamgir, F. M.; Strauss, E.; denBoer, M.; Greenbaum, S.; Whitacre, J. F.; Kao, C.-C.; Neih, S., LiCoO2 Thin-Film Batteries Structural Changes and Charge Compensation. *Journal of the Electrochemical Society* **2005,** *152*, A845-A849.

15.   Maugeri, L.; Iadecola, A.; Joseph, B.; Simonelli, L.; Olivi, L.; Okubo, M.; Honma, I.; Wadati, H.; Mizokawa, T.; Saini, N. L., Local structure of LiCoO2 nanoparticles studied by Co K-edge x-ray absorption spectroscopy. *J Phys Condens Matter* **2012,** *24* (33), 335305.

Appendix 6. Contributions to other work.

Throughout my tenure as a researcher in the Center for Sustainable Nanotechnology, I have made both intellectual and experimental contributions to a number of collaborative studies. Below I summarize the major findings of these projects, as well as my specific contributions to their success.

A.6.1. Published work.

A.6.1.1. Abbaspour-Tamijani, A., Bennett, J.W., Jones, D.T., Cartagena-Gonzalez, N., Jones, Z.R., Laudadio, E.D., Hamers, R.J., Santana, J.A., Mason, S.E. DFT and Thermodynamics Calculations of Surface Cation Release in LiCoO$_2$. *Appl. Surf. Sci.* **2020,** *515*, 145865-145873**.** DOI: 10.1016/j.apsusc.2020.145865

The goal of this work was to use density functional theory (DFT) + thermodynamics to model and predict cobalt release from LiCoO$_2$ surfaces in aqueous environments. This work also includes DFT vibrational analysis of surface termination-specific vibrational modes of LiCoO$_2$. My contributions to this work were both intellectual during the manuscript preparation stage, and also experimental data acquisition. Layer spacing of LiCoO$_2$ nanoparticles and bulk material was acquired from experimental x-ray diffraction analysis and guided benchmarking of the model in this manuscript.

A.6.1.2. Buchman, J.T., Bennett, E.A., Wang, C., Abbaspour Tamijiani, A., Bennett, J.W., Hudson, B.G., Green, C.M., Clement, P.L., Zhi, B., Henke, A.H., Laudadio, E.D., Mason, S.E., Hamers, R.J., Klaper, R.D., Haynes, C.L. Nickel enrichment of next-generation NMC nanomaterials alters material stability, causing unexpected dissolution behavior and observed toxicity to *S. oneidensis* MR-1 and *D. magna. Environ. Sci.: Nano* **2020,** 7, 571-587. DOI: 10.1039/C9EN01074B

The goal of this work was to investigate the toxicity of equistoichiometric LiNi$_x$Mn$_y$Co$_{1-x-y}$O$_2$ (x = 0.33, y = 0.33, 1-x-y=0.33, "NMC333") materials and compare to those with a higher nickel content (x = 0.6, y = 0.2, 1-x-y = 0.2, "NMC622") to two model biological organisms, the gram negative soil bacterium *Shewanella oneidensis* MR-1 and the eukaryotic water flea *Daphia magna*. The major findings of this work are that the dissolution behavior of NMC333 versus NMC622 are inconsistent with the stoichiometries of the material. Notably, NMC622 released approximately the same concentration of [Ni^{2+}] as NMC333 into both aqueous media studied. Density functional theory (DFT) simulations are able to attribute the unexpected dissolution behavior of NMC622 to the different lattice stability of Ni^{4+} versus Ni^{2+} in the material lattice. The impact on toxicity is nominally the same level of toxicity of NMC333 and NMC622 to *S. oneidensis*, where the major mode of toxicity is ion release, but different levels of toxicity to *D. magna*, where the major mode of toxicity is through ingestion of the nanomaterials. My contributions to this work were intellectual during the stages of manuscript preparation and revision, as well as synthetic, where myself and summer undergraduate research student Nafisa Ibrahim were the first to synthesize NMC622, and trained further collaborators on the synthetic technique.

A.6.1.3. Mensch, A.C., Melby, E.S., Laudadio, E.D., Foreman-Ortiz, I.U., Zhang, Y., Dohnalkova, A., Hu, D., Pedersen, J.A., Hamers, R.J., Orr, G. Primary amine-terminated quantum dots preferentially interact with membrane domain boundaries in bilayers and lipid rafts at the cell membrane as revealed by atomic force and super resolution fluorescence microscopy. *Environ. Sci.: Nano* **2020**, *7,* 149-161.

The goal of this work was to understand the impact of amine-terminated quantum dots on the structural properties of model cellular membranes. Supported lipid bilayers with "lipid rafts"

were prepared as model eukaryotic membranes, and the interaction of primary amine-terminated quantum dots with these bilayers was studied with atomic force microscopy (AFM) and super resolution fluorescence microscopy. It was discovered using AFM that the quantum dots preferentially interacted with the domain boundaries of the liquid-disordered regions in the bilayer, which then led to further disruption of the lipid rafts and imbedding of the amphiphilic particles into the bilayer. Correlated fluorescence microscopy corroborated these findings. My contributions to this work were X-ray photoelectron spectroscopic analysis of the quantum dots. This spectral analysis of the N(1s) region revealed the presence of amine groups on the particle surface. This contribution is included in Figure 1 of the manuscript (reproduced below as Figure A.6.1)
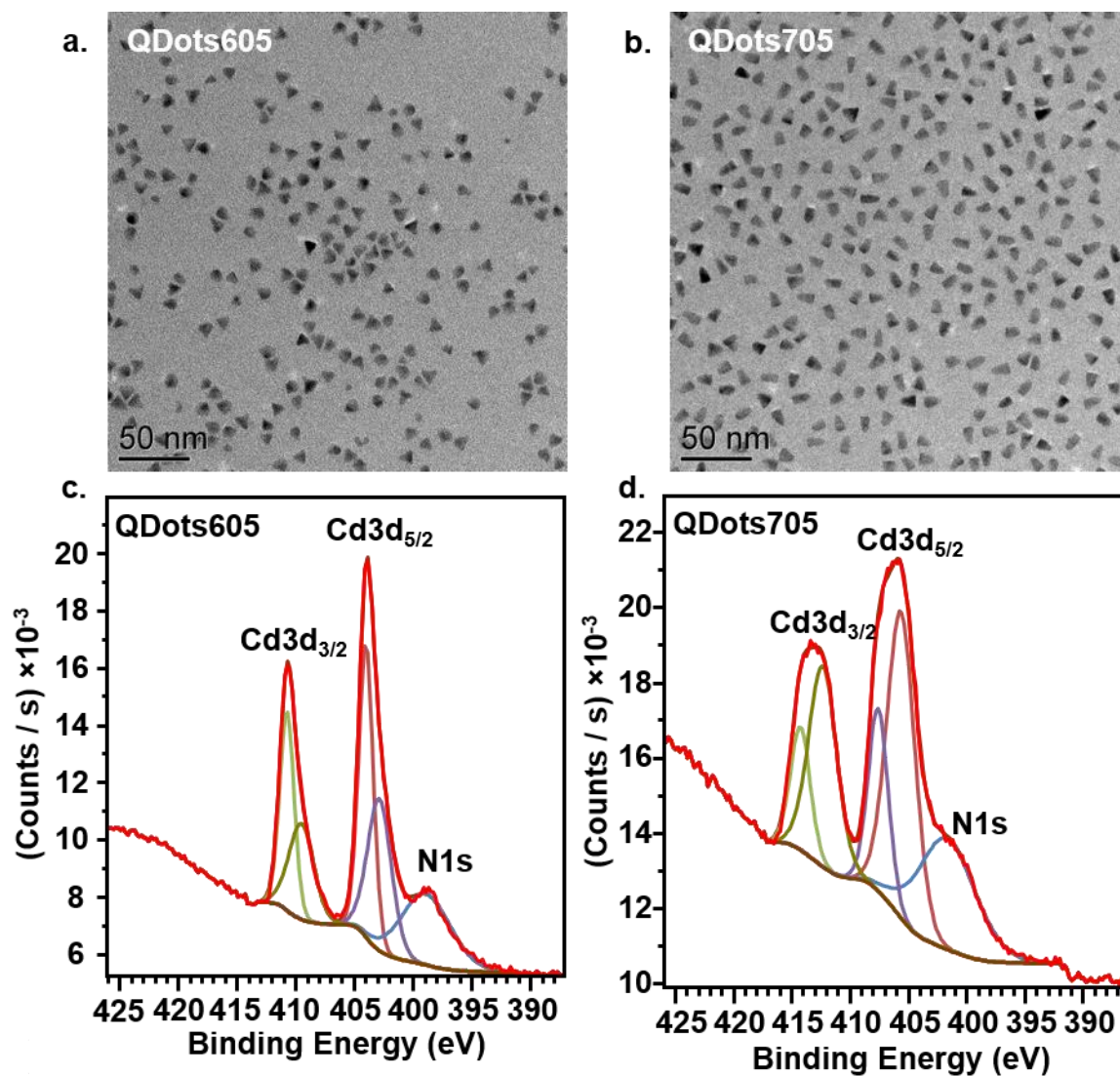
Figure A.6.1. a. and b. TEM analysis of QDot605 (a) and QDot705 (b) showing the size distribution of each particle type. c. and d. XPS analysis of QDot605 (c) and QDot705 (d) confirming the presence of amine groups on the surface of the particles. The XPS raw data (red) are fit with the different color traces as described in the Methods section.

A.6.1.4. Cui, Y.; Melby, E.S.; Mensch, A.C., <u>Laudadio, E.D.,</u> Hang, M.N., Dohnalkova, A., Hu, D., Hamers, R.J., Orr, G. Quantitative mapping of oxidative stress response to lithium cobalt oxide nanoparticles in single cells using multiplexed in situ gene expression analysis. *Nano Lett.,* **2019,** *19*, 1990-1997. DOI: 10.1021/acs.nanolett.8b05172

The goal of this work was to use a recently established super resolution imaging technique, multiplexed fluctuation localization imaging-based fluorescence in situ hybridization (fliFISH) for quantitative mapping of the gene expression responses, specifically oxidative stress genes, in single rainbow trout gill cells (*Oncorhynchus mykiss*) to exposure to $LiCoO_2$. Ten oxidative stress response genes were labeled and tracked through the implementation of two-color barcoding in the fliFISH technique. It was observed that initially, genes targeting superoxide species were upregulated, followed by an increase in gene copies targeting peroxide and hydroxyl species. Co^{2+} and Li^+ ions were found to inhibit transcription for all of the stress response genes. Taken together, this work suggests a "two-hit" toxicological response to $LiCoO_2$ nanoparticles, where the particles themselves induce oxidative stress, and ions released from the particles inhibit transcription of defense genes. My contributions to this work were nanoparticle synthesis and characterization. I characterized the nanomaterials used in this study to confirm that no significant changes to surface properties had occurred over the time period that the experiments were conducted over. I also synthesized an additional batch of nanomaterials that select experiments were repeated with to ensure reproducibility across nanoparticle batches. The characterization information is detailed in the manuscript's supporting information file.

A.6.1.5. Chong, G., <u>Laudadio, E.D.,</u> Wu, M., Murphy, C.J., Hamers, R.J., Hernandez, R. Density, Structure, and Stability of Citrate^{3-} and H_2Citrate$^-$ on Bare and Coated Gold Nanoparticles. *J. Phys. Chem. C* **2018,** *122,* 28393-28404. DOI: 10.1021/acs.jpcc.8b09666

The goal of this work was to apply all-atom molecular dynamic simulations towards the understanding of the density, structure and stability of citrate capping molecules on gold nanoparticles (AuNPs). The outcomes of this work are a consensus citrate density for the different states of citrate on the particles, to aid both with experimental AuNP characterization and also future molecular dynamics simulations. My contributions to this work were experimental corroboration of the ensemble binding modes of citrate on AuNPs as determined through the MD simulations. Attenuated Total Reflectance – FTIR (ATR-FTIR) was employed on citrate capped AuNPs, both dry and in solution, to determine the vibrational modes of citrate on the AuNP surface. From the ATR-FTIR spectra, we were able to corroborate MD results showing the presence of H_2citrate$^-$ functionalities within poly(allylamine hydrochloride) (PAH) wrapped citrate-capped AuNPs. The spectra are also in agreement with the conformations of PAH interacting with citrate molecules on AuNPs as predicted from simulation. These spectra were included in Figure 9 of the manuscript (reproduced below as Figure A.6.2)
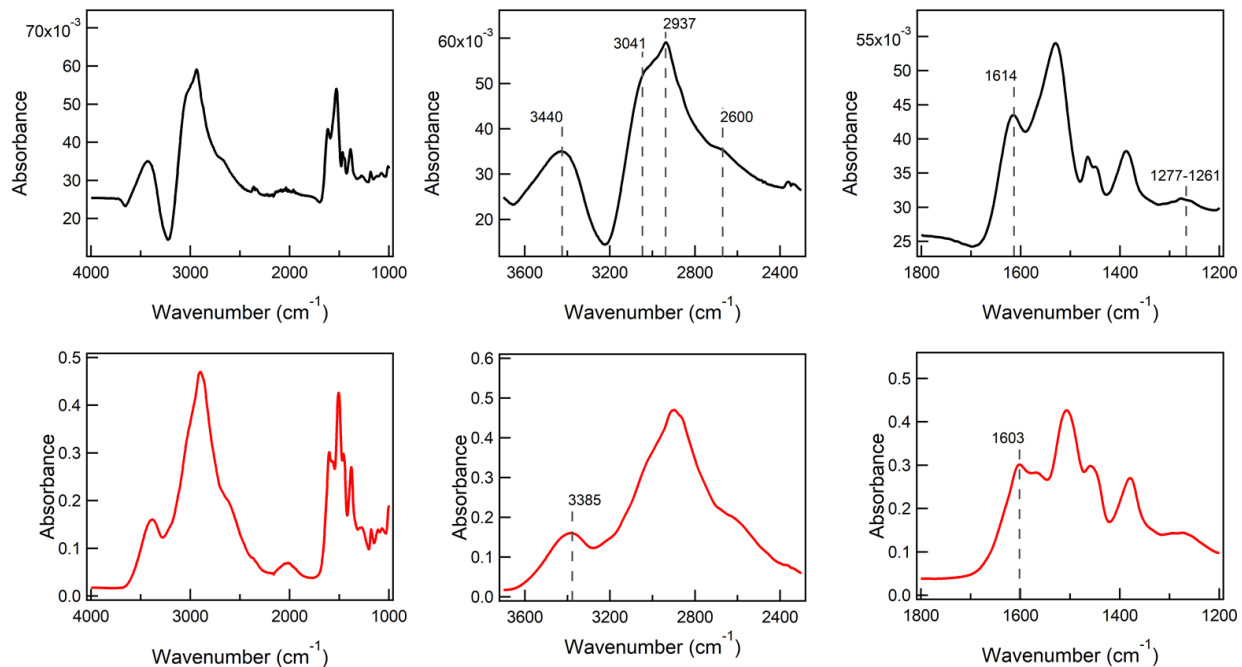
Figure A.6.2. ATR-FTIR spectrum of PAH−cit-AuNPs in solution (top row) and dry (bottom row): the full (from 4000 to 1000 cm^{-1}), OH region (from 3700 to 2300 cm^{-1}), and fingerprint region (from 1800 to 1200 cm^{-1}) spectra are shown from left to right.

A.6.1.6. Huang, X., Bennett, J.W., Hang, M.N., <u>Laudadio, E.D.,</u> Hamers, R.J., Mason, S.E. Ab Initio Atomistic Thermodynamics Study of the (001) Surface of $LiCoO_2$ in a Water Environment and Implications for Reactivity under Ambient Conditions. *J. Phys. Chem. C* **2017,** *12*, 5069-5080. DOI: 10.1021/acs.jpcc.6b12163

The goal of this work was to use (DFT) (specifically, GGA + U methodology) to model bulk and surface structures of the (001) face of $LiCoO_2$. One of the major outcomes of this work was understanding the likely surface terminations of $LiCoO_2$ in aqueous solution. While $LiCoO_2$ is terminated in lithium atoms on the (001) face in the pristine material, this work shows that in an aqueous environment, it is preferable for those lithium ions to dissociate and be replaced with protons. The hydroxylated surface of $LiCoO_2$ is more reactive to species in solution such as the phosphate oxyanion, where the models predict energetically favorable outer-sphere interactions between the adsorbate and the hydroxylated $LiCoO_2$ (001) surface, whereas this interaction is not favorable when the surface is lithium terminated. My contributions to this work were some of the preliminary experimental results showing that phosphate does adsorb to the surface of $LiCoO_2$ in aqueous environments, thus validating the model predictions.

A.6.2. Manuscripts submitted.

A.6.2.1. Mensch, A.C., Mitchell, H.D., Markillie, L., <u>Laudadio, E.D.,</u> Schwartz, M.P., Hamers R.J., Orr, G. Impact of toxic and subtoxic doses of lithium cobalt oxide nanoparticles and their ions on molecular pathways in trout gill epithelial cells. *Environ. Sci.: Nano,* **2020.** Under review.

The goal of this work was to determine the impact of $LiCoO_2$ nanoparticle exposure at subtoxic and toxic levels to the gene expression and molecular pathways of trout gill epithelial cells (*Oncorhynchus mykiss*). It was found that $LiCoO_2$ nanoparticle exposure impacted four main functions; metabolic and energy-related processes, hypoxia and oxygen-related processes, membrane binding and internalization, and development. These findings were consistent with past and ongoing work suggesting that $LiCoO_2$ may sorb or oxidize biomolecules and induce other oxidative stress. My contributions to this work were both the nanoparticle synthesis and characterization of the materials used in this study, as well as data acquisition and analysis of the ion release experiments to determine concentrations of Li^+ and Co^{2+} ions for use in the ion control experiments. The zeta potential of $LiCoO_2$ particles in nanopure water and cell growth medium were included in Figure 1 of the manuscript (reproduced below as Figure A.6.3) and scanning electron microscopy and x-ray photoelectron spectroscopy characterization was included in Figure S1 of the Supporting Information (reproduced below as Figure A.6.4).
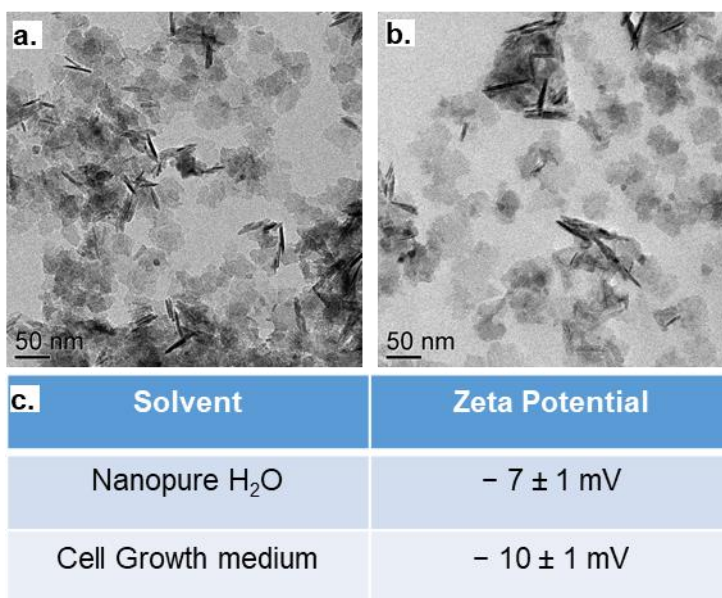
Figure A.6.3. TEM images showing the size distribution of the LCO nanosheets in a. nanopure water and b. cell culture growth medium. c. Zeta potential characterization of the nanosheets in nanopure H_2O and growth medium.
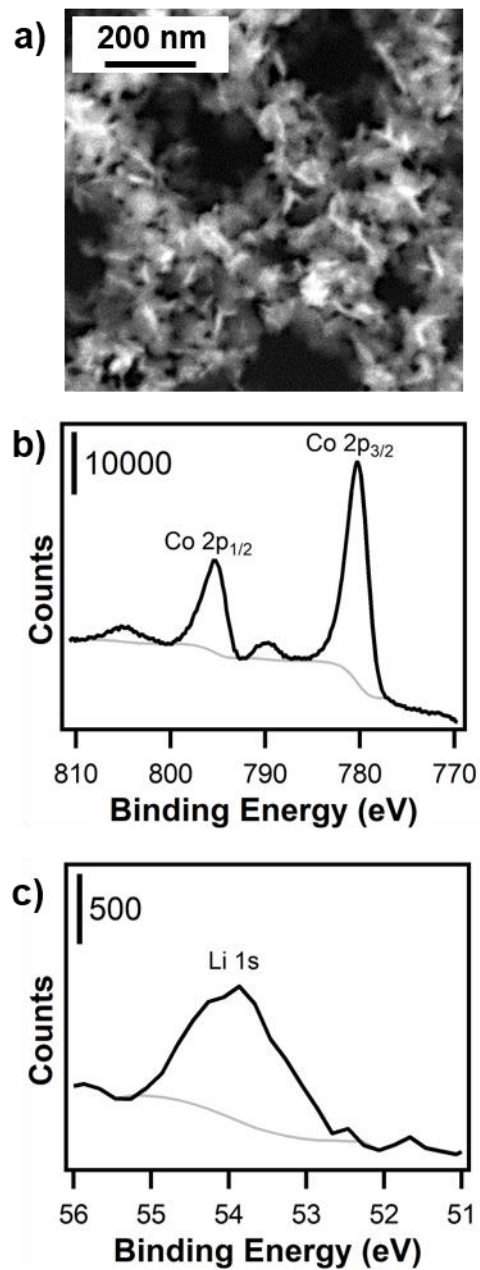
Figure A.6.4. Additional LCO NP characterization data, including a. scanning electron micrograph of LCO nanosheets and x-ray photoelectron spectroscopy (XPS) spectrum of the b. Co 2p region and c. Li 1s region collected from LCO nanosheets. Black trace: spectrum, gray trace: background.

A.6.2.2. Foreman-Ortiz, I.U., Liang, D., <u>Laudadio, E.D.,</u> Calderin, J.D., Wu, M., Keshri, P., Zhang, X., Schwartz, M.P., Hamers, R.J., Rotello, V.M., Murphy, C.J., Cui, Q., Pedersen, J.A. Anionic nanoparticle-induced fluidization of lipid membranes affects ion channel function. *PNAS*, **2020.** Under review.

The goal of this work was to understand the impacts of negatively charged gold nanoparticles on the function of gramicidin A (gA), a model ion channel, in suspended lipid bilayers and vesicles. This work combines electrophysiology, molecular dynamics simulations, and FTIR vibrational analysis to examine how these nanomaterials affect ion channel function. My contributions to this work were characterization of the ligand shell surrounding the nanomaterials using X-ray photoelectron spectroscopy, which allowed for the determination of free ligand in solution for subsequent free ligand control experiments. I also assisted in the acquisition and analysis of the FTIR spectra, which show an increase in the monomeric gA vibrational modes after exposure to gold nanoparticles, suggesting that the gold nanoparticles disrupt gA's ability to dimerize in the vesicles. These spectra were included in Figure 3 of the manuscript (reproduced below as Figure A.6.5)
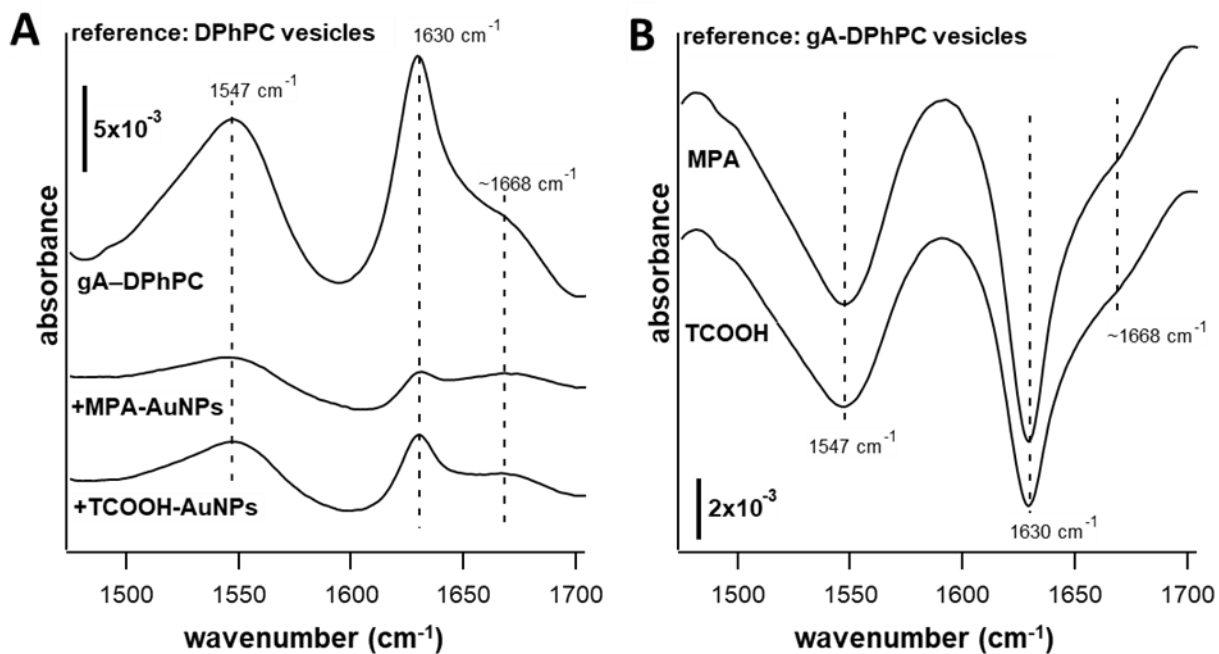
Figure A.6.5. Amide I and II region in the infrared absorbance spectra of gA-containing DPhPC vesicles before and after exposure to 100 nM of the indicated nanoparticle. Spectra were referenced against (A) DPhPC vesicles lacking gA and (B) DPhPC vesicles containing gA. Abbreviations: DPhPC, 1,2-diphytanoyl-sn-glycero-3-phosphocholine; gA, gramicidin A; MPA, mercaptopropionic acid; TCOOH, mercaptodecanoic-tetraethyleneglycol-carboxylate.